Nonlocal modelling of fracture in heterogeneous quasi-brittle materials

Dimitrios Xenos

Infrastructure & Environment Research Division
School of Engineering

University of Glasgow

Submitted in fulfilment of the requirements for the Degree of Doctor of Philosophy

April 2015

Abstract

Integral-type nonlocal models provide a mesh-independent description of fracture in quasi-brittle materials. According to these constitutive models, the stress at a point is evaluated by a weighted average of the variable describing the state of the material in the vicinity of this point. The weights of the material points depend on a model parameter, called interaction radius, that controls the size of the final failure zones. The objective of the present thesis is to develop nonlocal models, that can provide a realistic description of failure in quasi-brittle materials. In particular, it is aimed to identify a realistic approach to take into account boundaries. Furthermore, a strategy to calibrate the nonlocal radius is developed. It is also required to demonstrate that the nonlocal models can describe fracture in reinforced concrete structures mesh-independently.

The performance of different nonlocal models in analysing boundaries is investigated. Nonlocal damage models with different averaging schemes as well as nonlocal and over-nonlocal damage-plasticity models are applied to analyse failure in beams subjected to three-point bending. The original formulation of nonlocal averaging and the overnon-local damage-plasticity model lead to excessive energy dissipation close to boundaries compared to meso-scale analysis results. The spurious energy dissipation is reduced in the analyses with the modified averaging schemes.

A new calibration strategy to determine the interaction radius is proposed based on the final experimental fracture patterns. The main assumption is that the majority of energy is dissipated in a localised rough crack and is validated based on meso-scale analyses results. The potential of the calibration strategy was shown by applying it to calibrate a nonlocal damage model based on the experimental fracture surface and load-displacement curve of a beam subjected to three-point bending.

Furthermore, a nonlocal extension of the damage-plasticity model CDPM2 is applied in the analyses of a reinforced concrete beam and a column. These experiments were selected because both localised and distributed cracking are experimentally observed and the material points are subjected to various stress states. It was illustrated that nonlocal models describe failure in reinforced concrete mesh-independently.

Acknowledgements

The research reported in the present thesis was completed in the Infrastructure & Environment Research Division within the School of Engineering of the University of Glasgow from September 2011 to April 2015. The financial support provided by the University is gratefully acknowledged.

I would like to thank Dr Peter Grassl for the patient guidance, encouragement and advice he has provided throughout my time as his student. I acknowledge the contributions of Prof. M. Jirásek, Dr M. Horák, Dr D. Grégoire and Prof. S. Morél to different parts of my work. I would also like to thank Prof. S. Wheeler for his pastoral support and his comments on my work during Friday's presentations.

I am also indebted to all my collegues in the 604 office in the Rankine Building. A special thanks to Andrea, Eri and Ignatios, the lunch team. I would also like to thank Graeme, Ross, Caroline and Alan for being a bad influence in conferences and for sharing lots of great moments with me. Costy and Michael were also very good friends and they helped me on various ocasions. I acknowledge the efforts of Xue, Li and Thomas to teach me the proper Chinese. I also would like to thank Ahmed, Zahur, Sandeep, Rémi, Euan, Dimitris and Ewan.

I owe a lot to my parents, Thomas and Elissavet for their dedication and the many years of support that provided the foundation to complete this PhD. Finally, I want to thank Maria, my girlfriend, for supporting me during all these brilliant four years in Glasgow.

Contents

List of Figures

List of Symbols

Roman Symbols

A_h	Hardening parameter calculated from (6.21)
B_h	Hardening parameters calculated from (6.21)
C_h	Hardening parameters calculated from (6.21)
d	Distance between two points
d_min	Minimum distance between two neighboring Voronoi cells
D_e	Isotropic elastic stiffness tensor
D_f	Parameter introduced in (6.30)
D_h	Hardening parameters calculated from (6.21)
e	Eccentricity parameter calculated from (6.5)
E	Young's modulus
E_h	Hardening parameter calculated from (6.21)
E_0	Parameter of the hardening law, described in (3.17)
f_bc	Material strength in equibiaxial compression
f_c	Compressive strength
f_d	Damage loading function
f_p	Plasticity yield function
f_t	Tensile strength
F_h	Hardening parameter calculated from (6.21)
g_p	Plastic potential function
H_p	Hardening modulus introduced in (6.17)
l_a	Autocorrelation length introduced in (3.32)

$\mathbf{m}$ The tensor equal to $\dfrac{\partial g_{\mathrm{p}}}{\partial \boldsymbol{\sigma}}$

m_{d} Parameter of the damage law evaluated from (3.3)

m_{p} Parameter of the hardening law calculated evaluated from (3.17)

m_0 Friction parameter calculated from (6.6)

n Parameter controlling the softening part of the damage law in (3.2)

n_{ij} Component j of the i$^{\mathrm{th}}$ eigenvector of the stress tensor

q_{h0} Initial hardening parameter of the hardening law introduced in (6.16)

q_{h1} Hardening function introduced in (6.16)

q_{h2} Hardening function introduced in (6.17)

$r\cos(\bar{\theta})$ Function controlling the shape of the deviatoric sections presented in (6.4)

R Interaction radius introduced in (3.12)

R_{h} Variable of x_{h} calculated from (6.20)

$\bar{\boldsymbol{s}}$ Deviatoric effective stress

$\boldsymbol{T}$ Transformation matrix calculated in (4.3)

t Parameter of the distance-based approach

w_{fc} Compressive softening parameter of the damage-plasticity model CDPM2

w_{ft} Tensile softening parameter of the damage-plasticity model CDPM2

x_{h} Hardening ductility measure calculated from (6.19)

x_{s} Softening ductility measure calculated from (6.28)

Greek Symbols

α Weight function

α_0 Weight function introduced in (3.12)

α_{c} Variable introduced in (6.26)

α_∞ Weight function for an infinite medium

α_∞^* Special weight function to take into account multi-dimensional interactions

β Parameter of both the distance- and the stress-based approaches

β_{c} Variable provides a smooth transition from pure damage to damage-plasticity softening processes during cyclic loading introduced in (6.30)

$\boldsymbol{\delta}$ Kronecker delta tensor

$\boldsymbol{\varepsilon}$ Strain tensor

$\varepsilon_{\mathrm{eq}}$ Equivalent strain

$\bar{\varepsilon}_{\mathrm{eq}}$ Nonlocal equivalent strain

$\varepsilon_{\mathrm{eq}}^{\mathrm{c}}$ Equivalent strain referring to the compressive part of the constitutive law

$\varepsilon_{\mathrm{eq}}^{\mathrm{t}}$ Equivalent strain referring to the compressive part of the constitutive law

$\varepsilon_{\mathrm{max}}$ Axial strain at peak stress f_{t} introduced in (3.2)

ε_{f} Parameter calculated from (3.4)

$\varepsilon_{\mathrm{fc}}$ Compressive softening parameter of the damage-plasticity law CDPM2

$\varepsilon_{\mathrm{ft}}$ Tensile softening parameter of the damage-plasticity law CDPM2

$\varepsilon_{\mathrm{in}}^{\mathrm{c}}$ Inelastic strain related to compressive damage

$\varepsilon_{\mathrm{in}}^{\mathrm{t}}$ Inelastic strain related to tensile damage

$\boldsymbol{\varepsilon}_{\mathrm{p}}$ Plastic strain tensor

ε_0 Strain at which damage initiates in the damage-plasticity law CDPM2

ε_1 Parameter controlling the softening part of the damage law shown in (3.2)

ε_2 Parameter controlling the softening part of the damage law shown in (3.2)

ε_3 Parameter calculated from (3.5)

κ_{d} Damage history variable

κ_{p} Cumulative plastic strain

λ Plastic multiplier

ν Poisson's ratio

$\bar{\theta}$ Lode angle of the effective stress tensor $\bar{\boldsymbol{\sigma}}$

$\bar{\rho}$ Deviatoric stress of the effective stress tensor $\bar{\boldsymbol{\sigma}}$

$\boldsymbol{\sigma}$ Stress tensor

$\bar{\boldsymbol{\sigma}}$ Effective stress tensor

$\bar{\boldsymbol{\sigma}}_{\mathrm{Pc}}$ Tensor formed by the negative principal components of the effective stress tensor $\bar{\boldsymbol{\sigma}}$ in the principal coordinate system

$\bar{\boldsymbol{\sigma}}_{\mathrm{Pt}}$ Tensor formed by the positive principal components of the effective stress tensor $\bar{\boldsymbol{\sigma}}$ in the principal coordinate system

$\bar{\boldsymbol{\sigma}}_{\mathrm{P}}$ Effective stress tensor $\bar{\boldsymbol{\sigma}}$ in the principal coordinate system

$\bar{\boldsymbol{\sigma}}_{\mathrm{c}}$ Tensor $\bar{\boldsymbol{\sigma}}_{\mathrm{Pc}}$ rotated in the global coordinate system

$\bar{\boldsymbol{\sigma}}_{\mathrm{t}}$ Tensor $\bar{\boldsymbol{\sigma}}_{\mathrm{Pt}}$ rotated in the global coordinate system

$\bar{\sigma}_{\mathrm{v}}$ Volumetric stress of the effective stress tensor $\bar{\boldsymbol{\sigma}}$

σ_{y} Yield stress defined in (3.16)

ω Damage variable

ω_{c} Compressive damage variable

ω_{t} Tensile damage variable

Mathematical Operators

: Double-dot product of two tensors

$< . >_{+}$ MacAuley brackets-positive part operator

$< . >_{-}$ Negative part operator

Chapter 1

Introduction

1.1 Background

Fracture in quasi-brittle materials has been investigated for more than 100 years and numerous experiments have been conducted on various materials such as cementitious composites, fibreglass or toughened ceramics, used in a wide range of applications. Concrete is the most intensively studied material, with the largest experimental effort but its failure is not yet fully understood. The inelastic behaviour of concrete members observed during experiments is not always in agreement with the one predicted during the design process and designers have to either increase the safety margins by underestimating the material properties or resort to extensive large-scale testing. The reason is that the material's fracture properties observed in small-sized specimens during laboratory experiments cannot be used directly to model larger structures using macroscopic constitutive laws that do not take into account the actual failure mechanisms.

Macroscopic constitutive models for quasi-brittle materials should provide an objective description of the final failure zones. This is achieved by including in the constitutive law information about the geometry of the Fracture Process Zone (FPZ), that forms during failure. In these regions, energy is dissipated by failure mechanisms, such as distributed micro-cracking, crack-bridging, as well as aggregate interlocking. Commonly used constitutive models for fracture in quasi-brittle materials are cohesive crack, crack-band and nonlocal models.

Nonlocal models are divided in gradient and integral type models and describe the FPZs by regularised strain profiles. The latter are used throughout the present thesis and are known to provide mesh-independent results for both tensile and compressive failure in nonlinear finite element analyses. In these models, the stress at a point is evaluated by a weighted average of the variable describing the state of the material in the vicinity of this point. The weights are defined by a weight function, whose main parameter is the interaction radius controlling the width of the final failure zones. Although integral-type nonlocal models are considered to be very suitable to describe fracture in quasi-brittle materials, they exhibit shortcomings, which need to be addressed. In particular, there is no consensus in the literature on how to calibrate the interaction radius and on how to take into account the influence of boundaries in nonlocal averaging. Modeling of boundaries is important because it is common for cracks to initiate at these areas due to local stress gradients and due to the increased density of smaller aggregates close to boundaries.

1.2 Aims & Objectives

The aim of the present thesis is to provide a framework for the development of nonlocal models, that provide a realistic description of failure in quasi-brittle materials. To achieve this aim the following three objectives should be met. A realistic approach to take into account boundaries should be identified (Chapter 4). A strategy to calibrate the interaction radius in nonlocal models should be developed (Chapter 5). A nonlocal approach to modelling failure in reinforced concrete members should be presented and the capability of nonlocal models to provide mesh-independent results should be demonstrated (Chapter 6).

1.3 Assumptions

The present thesis focuses on the mechanical response of concrete. Phenomena related to heat transfer, moisture transport and chemical reactions are not taken into account. The mechanical problem is formulated according to the theory of small strains. Quasi-static loading conditions are assumed. Fracture is investigated at two different scales: the meso- and the macro-scale. At the meso-scale, concrete is considered as a heterogeneous three phase composite composed of a mortar matrix, coarse aggregates and ITZs between the two other phases. Coarse aggregates are modelled as linear elastic. The

spatial variation of the fracture properties in mortar and ITZ due to finer aggregates and the micro-structure of the mortar phase is included by auto-correlated random fields. The structural response is modelled by a 2D lattice consisting of structural elements. At the macroscale, concrete is modelled as homogeneous continuum by applying the Finite Element Method (FEM) using 3D tetrahedra or 2D plane strain triangles. Fracture is modelled implicitly by damage or damage-plasticity material models formulated according to the nonlocal or the crack-band approach. Steel reinforcement is analysed directly by beam and truss elements with elastic-perfectly plastic constitutive laws.

1.4 Outline

The present thesis is divided in 7 chapters. In Chapter 2, the literature review is presented. The fracture processes in quasi-brittle materials are reviewed including a detailed description of the FPZ and the factors that influence its formation. Macroscopic material models for concrete are briefly discussed focusing on damage-plasticity approaches and on nonlocal models. Different nonlocal averaging procedures reported in the literature are described, which lead to a reduction of the spurious energy dissipation close to boundaries observed in analyses with standard nonlocal models. Furthermore, existing calibration strategies of the interaction radius are presented.

In Chapter 3, the modelling approaches, which will be applied in the subsequent chapters, are described. Macroscopic nonlocal models are presented, that are based on damage mechanics and a combination of damage mechanics and plasticity. The main features of the meso-scale approach are reviewed. The next three chapters address the objectives set in Section 1.2.

In Chapter 4, different nonlocal approaches are investigated and the nonlocal model that provides a realistic description of boundaries is identified. The constitutive laws are calibrated against meso-scale analyses results by analysing specimens, in which the influence of the boundary conditions is eliminated. The calibrated material models and the meso-scale approach are applied to analyse unreinforced concrete beams with different types of boundaries. The performance of the nonlocal models in analysing boundaries is evaluated by comparing the load-displacement curves and the dissipated energy profiles with the meso-scale analyses results.

In Chapter 5, a new calibration strategy for nonlocal models based on the final crack patterns is developed. The main assumptions of the calibration procedure are validated based on meso-scale analyses results. The performance of the calibration procedure is evaluated by means of a simple application of a concrete beam subjected to three-point bending.

In Chapter 6, the potential of nonlocal models to describe failure in reinforced concrete specimens mesh-independently is highlighted. A damage-plasticity material model formulated according to the crack-band approach is presented, which is capable of describing the material response under various stress states. An extension of this material model according to the nonlocal theory is proposed. The two material models are applied to analyse failure of a reinforced concrete beam and a column and their mesh-dependence is investigated. The results are evaluated globally in the form of load-displacement curves and locally in the form of principal strain contour plots and mesh-independence of nonlocal models is investigated.

In Chapter 7 conclusions arising from this thesis are presented along with recommendations for future work.

Chapter 2

Literature Review

This chapter presents a review of the literature, on which the research of the present thesis was based. The fracture processes in concrete are presented by focusing on the Fracture Process Zone (FPZ), in which the fracture energy is dissipated. This is a nonlinear zone of distributed microcracking, that forms around the mean crack front during failure. Two numerical approaches to model fracture are presented. The first approach relies in directly modelling the mechanical response of the material meso-scale. Cracks are modelled as displacement discontinuities by a lattice of structural elements. In the second approach concrete is modelled as a continuum in the macroscale. Failure is described as permanent deformations by plasticity models, or as a reduction of the material stiffness by damage models, or by combinations of both models, all of which are reviewed. It is illustrated that localised failure can be described by formulating these material models according to the crack-band or the nonlocal theory. The main issues of the nonlocal approaches are discussed including modelling of boundaries and the calibration of nonlocal models.

2.1 Fracture Processes in Concrete

Recent developments in quasi-brittle fracture aim at understanding the failure mechanisms occurring in the material meso-structure and their effects on the macroscopic behaviour of structures (Landis, 1999). The key assumption to bridge these two scales is to investigate the nonlinear zone, defined as FPZ, that forms around the crack front during failure. In this region, energy is dissipated at each loading step (Muralidhara et al., 2010). In very large structures made of very brittle materials, such as ceramics, the size of the FPZ is much smaller than the structure size (Bažant, 1999) and its

influence can be ignored. Fracture can be analysed with constitutive laws, formulated according to Linear Elastic Fracture Mechanics (LEFM), that are based solely on the material strength (Hillerborg et al., 1976). In any other case, the FPZ needs to be included in the material model, which should be formulated according to Nonlinear Elastic Fracture Mechanics (NLEFM) to account for the nonlinear stress distribution within the FPZ (Cedolin et al., 1983).

The influence of the material composition needs to be considered to accurately describe the FPZ. The maximum diameter of the aggregates $d_{\max}$ in the concrete mix influences the size of the FPZ but this relationship was not identified in Cedolin et al. (1987). Single Edge Notched (SEN) and unnotched specimens were subjected to tension and the FPZ was monitored by recording the displacement patterns of a photoelastic coating on the specimen surface. The FPZ is a three-dimensional region and cannot be specified only from the deformation patterns at the surface because they can vary from the ones in the core of the specimen. The incompatibility of the deformation patterns can be attributed to the increased density of smaller aggregates close to the specimen boundaries (Kreijger, 1984). In Mihashi et al. (1991), concrete specimens were subjected to compact tension and the FPZ was monitored by the Acoustic Emissions (AE) technique, that involves recording the location and the intensity of the AE signals in the specimen during fracture. It was illustrated, that the FPZ size increases for increasing $d_{\max}$. This is in accordance with other experimental results reported by Otsuka and Date (2000), where the FPZ was investigated in compact tension tests by means of the AE technique and X-ray scans at different loading stages. The results indicated a change of both the FPZ shape and size in the form of an increase of the width and a decrease of the length for increasing $d_{\max}$. Similar conclusions can be drawn for other heterogeneous quasi-brittle materials, such as rocks (Přikryl et al., 2003). The effect of concrete porosity on the size of the FPZ was investigated, for instance in Haidar et al. (2005). Concrete beams were subjected to three-point-bending and failure was monitored by recording AEs in the specimen. It was shown, that the FPZ size increases for increasing material porosity. Furthermore, the FPZ geometry may completely change due to self-healing processes, that depend on the content of unhydrated cement and the curing environment, in which the structure is exposed (Granger et al., 2007). Hence, the size of the FPZ increases for increasing $d_{\max}$, increasing material porosity and is influenced by self-healing processes.

The boundary conditions in the form of specimen geometry and loading type have been reported to strongly influence the FPZ (Guinea et al., 1992; Tang et al., 1996). Jankowski and Styś (1990) investigated the evolution of the FPZ in geometrically similar notched beams subjected to four-point bending by means of a photoelastic coating method. It was illustrated that the FPZ width increases as the crack propagates away from the notch. This effect was investigated in Hu and Wittmann (1990) by implicitly

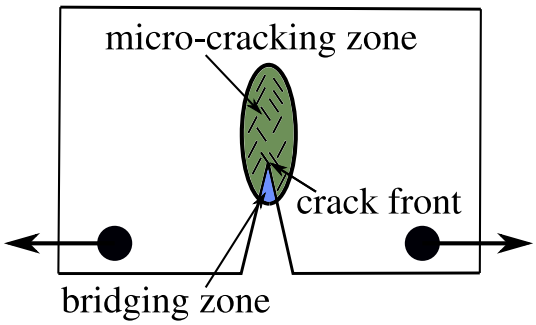

Figure 2.1: Schematic description of the micro-cracking and crack bridging zones on a plane through the thickness of a compact tension specimen.

specifying the FPZ width in specimens subjected to wedge-splitting with an iterative technique. The elastic compliance-notch length calibration curve was initially constructed based on experimental results from specimens with different notch depths. Then, the FPZ was measured at a certain loading stage by loading, unloading and reloading the specimen to measure its compliance. The notch was extended to match the notch length for the measured compliance based on the calibration curve. The procedure was repeated until no notch extension was needed indicating that the current notch tip was outside the FPZ. Hu and Wittmann (1992) applied an analytical technique based on dissipated energy arguments to demonstrate that the FPZ size increases as the crack propagates away from the specimen boundary. The influence of the type of the boundary was experimentally investigated in Labuz and Biolzi (1998) by recording the AE signals in notched and unnotched granite and sandstone beams subjected to four-point bending. High energy AEs were distributed in a larger area in the unnotched specimens than in the notched ones, which indicates the influence of the strain field around the specimen boundary on the FPZ size. Otsuka and Date (2000) illustrated that the FPZ size increases as the crack propagates away from the boundary until it attains its maximum "saturated" size for a long enough ligament length, i.e. the distance between the notch tip and the opposite boundary of the beam. Then, it starts to decrease as it approaches the other boundary of the structure. Chen and Liu (2004) investigated in notched three-point bending specimens the influence of the ratio of the ligament length to the total beam depth on the FPZ by applying an AE technique. It was argued that the maximum recorded width of the FPZ increases for increasing values of the absolute ligament length. Moreover, a Digital Image Correlation (DIC) technique was applied to monitor the FPZ size in Wu et al. (2011). The displacements of individual points on the specimen were calculated at a certain loading stage by comparing images of the specimen in the deformed and the undeformed state. These values were then used to reconstruct the displacement field. The FPZ width can be only qualitatively determined based on the DIC results because the calculated values depend on the density of the monitored points. From all the abovementioned experimental results it can be concluded that the maximum width of the FPZ in notched specimens depends on the ligament length as its width increases for increasing distance of the crack front from the boundaries.

The FPZ is the result of a set of dissipative mechanisms that act in the concrete meso-scale. At this scale, concrete is considered as a heterogeneous three phase composite composed of a mortar matrix, aggregates and Interface Transition Zones (ITZs) between the two other phases. Li and Maalej (1996) argued that crack bridging and micro-cracking are the main failure mechanisms in normal strength concrete 2.1. Microcracking is the result of the failure of the interface zones between aggregates and mortar occurring in a zone around the macroscopic crack-tip and accounts for less than 20% of the total fracture energy (Cedolin et al., 1987; Nirmalendran and Horii, 1992). Crack-bridging dissipates most of the fracture energy mainly in the post-peak resulting in softening, i.e. decreasing stresses for increasing strains. This mechanism acts in the wake of the main crack front and is attributed to aggregate bridging in mode I or aggregate interlocking and friction between the crack surfaces in modes II and III of cracking, respectively (van Mier, 1991; Landis, 1999).

A group of researchers focused on the investigation of the FPZ in the meso-scale based on the geometry of the final crack-patterns. Saouma et al. (1990) recorded the crack patterns of concrete specimens with different $d_{\max}$ failing in uniaxial compression. The fracture surfaces were scanned by a mechanical profilometer and the average standard deviation of the crack patterns from the mean crack plane was calculated for different sampling window sizes. It was illustrated that the crack patterns are fractal, i.e. their geometrical properties are invariant to the investigated length-scale. Bouchaud et al. (1990) applied scanned electron microscopy to record the fracture surface of aluminum compact tension specimens subjected to different heat treatment. The validity of the fractality assumption was proven and it was shown that the fractal properties were comparable to the ones for concrete. In Lange et al. (1993), confocal microscopy was applied to scan the fracture surface of notched mortar beams with different compositions subjected to three-point bending. It was illustrated, that the average standard deviation of the fracture surface from the mean crack plane for a given window size is correlated with the fracture toughness K_{IC}. In a similar experimental campaign, Morel et al. (2008) investigated notched mortar beams subjected to four-point bending. It was concluded that the fractality does not hold for larger length scales. Moreover, it was suggested that the largest window size for which fractality is still valid can be related to the FPZ size.

The concept of relating the FPZ size to the final fracture patterns is adopted in the present thesis. The reason is that the final crack patterns are preceded by the FPZ which affects their tortuosity in the form of the standard deviation of the crack surface from the mean crack plane. This was reflected in the presented experimental results from the literature where both the FPZ and the tortuosity of the crack patterns were influenced similarly by the same factors. The relationship between the standard deviation of the crack patterns and the width of the FPZ is used in Chapter 4 to calibrate

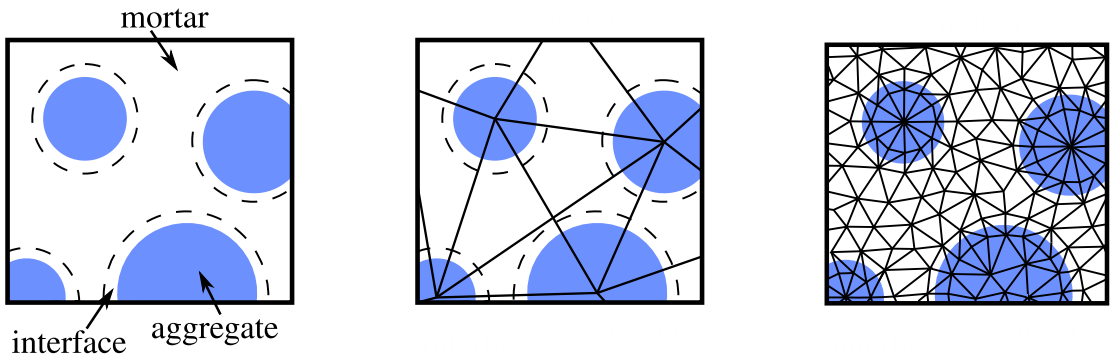

Figure 2.2: Schematic overview of meso-scale modelling approaches for the meso-structure shown in (a): (b) The analysed lattice is related to the meso-structure, (c) The meso-structure is not related to the analysed lattice.

a nonlocal constitutive law.

2.2 Meso-scale approach

Numerical approaches were applied to investigate the FPZ and some of them aimed at directly analysing the mechanical response of the meso-scale. According to a group of these models, concrete is considered as a three-phase composite including mortar, ITZs and aggregates and is analysed by structural truss or beam elements (Kawai, 1978). The displacements are calculated at the nodes of the elements and the material response is evaluated at a point between the two nodes (Cundall and Strack, 1979). A group of those models, the particle models, take into account the evolution of the nodal arrangement during the loading process and are suitable for large-strain problems. Another set of approaches, known as the lattice approaches, rely in a lattice of beam elements, that connects the centres of the cells remaining unchanged during loading (Kawai, 1980). This approach is computationally efficient and is suitable for the small-strain problems investigated in the present thesis (Herrmann et al., 1989).

In the lattice approaches, the concrete meso-structure is described in at least two ways (Figure 2.2). In the first approach, lattice elements connect the centres of the aggregates in order to model the kinematics of the meso-structure (Zubelewicz and Bažant, 1987). The nonlinearity of the material response between two aggregates is evaluated at single point between them by a stress–strain law. The second approach relies in mapping information of the heterogeneous meso-structure of concrete on a lattice in the form of spatially varying material properties (Schlangen and van Mier, 1992). Smaller lattice element sizes are used leading to an increased computational

cost because individual aggregates are represented by several lattice elements. In this approach, lattice nodes are placed randomly to ensure that the resulting failure patterns do not follow the mesh lines (Jirásek and Bažant, 1995). The lattice edges and their cross-sections are specified based on the Delaunay and the Voronoi tessellation of the set of lattice nodes, respectively (Bolander and Saito, 1998). This approach was shown to be suitable for fracture simulations and is applied in the present thesis (Bolander and Sukumar, 2005). Smaller aggregates are modelled by applying an auto-correlated random field on the fracture properties of mortar and ITZs, which is generated by a spectral representation technique (Shinozuka and Jan, 1972; Shinozuka and Deodatis, 1996). Furthermore, the constitutive response is evaluated at the centre of the Voronoi cross-section by damage constitutive laws, as it was suggested in Grassl and Bažant (2009). These material models are successful in describing mode-I fracture, analysed in the present thesis as shown in Grassl and Jirásek (2010). However, combinations of damage and plasticity constitutive laws can be used in other types of failure, for example uniaxial compressive failure, like the one presented by (Grassl et al., 2012).

Meso-scale analyses results have provided important insight in the fracture processes in concrete. The influence of the aggregate density on the fracture process was investigated in two- and three-dimensional concrete specimens subjected to uniaxial tension by Prado and van Mier (2003); Lilliu and van Mier (2003). The sequence of meso-scale failure mechanisms included debonding of the aggregates from the mortar matrix in the pre-peak and crack bridging along the main crack in the post-peak. For low aggregate densities, micro-cracks appeared due to debonding in the ITZs around aggregates that are far from the final macro-crack. The latter was formed as soon as the micro-crack density had sufficiently increased. For high aggregate densities, micro-cracks appeared around aggregates, that were closer to each other, and coalesced to form the final macro-crack. This effect led to a decreased pre-peak nonlinearity for increasing particle density in the final stress-strain curve. Grassl and Jirásek (2010) illustrated that parameters of macroscopic material models can be specified from the FPZ observed from meso-scale analyses results. A nonlocal damage model was calibrated by fitting the load-displacement curves and the dissipated energy profiles against the meso-scale analyses results. Grassl et al. (2012) investigated the influence of the beam depth and of the notch type in analyses of two-dimensional notched concrete beams, subjected to three-point bending. It was illustrated that the FPZ width depends on the notch type whereas the dissipated energy distribution along the ligament is insensitive to the boundary type. Grégoire et al. (2015) compared meso-scale analyses and experimental results of concrete beams subjected to three-point bending. The energy distribution of the recorded AE signals during failure was compared to meso-scale energy dissipation profiles. The agreement between the two graphs indicated that the meso-scale model described the evolution of the FPZ during failure consistently. Moreover, both the experimental and the numerical results indicated that the larger the ligament length the larger the size of the FPZ.

2.3 Macroscopic approaches

Concrete failure is commonly modelled by macroscopic material models, that are based on phenomenological descriptions of the material failure. These models are formulated within the framework of either damage mechanics or plasticity or a combination of both theories (Luccioni and Oller, 2003; Červenka and Papanikolaou, 2008; Hofstetter and Valentini, 2013).

Stress-based plasticity models rely in the decomposition of the total strains in elastic and inelastic plastic strains, that describe the permanent deformations and the path dependence observed in concrete during unloading and cyclic loading (van Mier, 1986; de Borst, 1987). Plastic strains increase so that the analysed stress state is always within the domain of admissible stress states, defined by the yield surface (Etse and Willam, 1994). This surface corresponds to the strength envelope at a certain loading stage and allows for the modelling of multi-axial stress states (Imran and Pantazopoulou, 1996; Bićanić and Pearce, 1996). The direction of the plastic strains is provided by the flow rule, which is a function of the plastic potential. Excessive volumetric expansion under high confinement followed by overprediction of the material strength is observed in associated flow rules, where the same function is used for both the plastic potential and the yield surface (Grassl et al., 2002; Grassl, 2004). A remedy to this problem are the non-associated flow rules, where the plastic potential is different from the yield function (Grassl, 2004; Papanikolaou and Kappos, 2007). Hardening or softening processes are included in the models by the cumulative plastic strain which is a variable of the yield surface and the plastic potential (Folino and Etse, 2012).

Furthermore, damage models are able to describe the reduction of stiffness during unloading or cyclic loading in tension and low confined compression, that was observed for example in Bahn and Hsu (1988). This is achieved in isotropic damage models by multiplying the effective stress, which is the product of the undamaged material stiffness matrix and the strain vector, by a scalar function of the damage parameter ranging between 0 and 1 for intact and fully damaged material. These material models are not able to describe the recovery of the initial material stiffness due to crack closure occurring upon change of the initial loading system in non-proportional loading experiments (Ortiz, 1985). Crack closure can be described by anisotropic damage laws, in which the damage variable is replaced by a damage tensor or a vector (Murakami and Ohno, 1981; Yazdani and Schreyer, 1988; Chaboche, 1993). A particular group of vectorial formulations of damage is applied in the present thesis. The effective stress tensor is decomposed in a tensile and a compressive tensor in the principal effective stress space and each part is multiplied by a separate damage parameter (Mazars and Pijaudier-Cabot, 1989; Fichant et al., 1999). According to Carol et al. (1994), the

damage surface is the equivalent of the yield surface in damage models and defines the domain of admissible stress states. The shape of the surface is controlled by the formulation of the equivalent strain (Tao and Phillips, 2005). The evolution of the damage surface at each loading stage is determined by the value of the set of the history parameters and the damage law (Voyiadjis and Kattan, 2009).

Damage-plasticity constitutive laws combine the advantages of both theories (Simo and Ju, 1987; Meschke et al., 1998; Jason et al., 2006). The advanced damage-plasticity model CDPM2, presented in Grassl et al. (2013), is applied in the present thesis. This constitutive law is able to describe the concrete behavior under multi-axial stress states, the irreversible deformations, stiffness decrease and the hardening observed during triaxial concrete failure.

Moreover, two versions of CDPM2 are used for structural analysis that rely in formulating the damage part, used to analyse softening, according to the nonlocal and the crack-band approach. If the local version of the constitutive law was applied, i.e. the tangential material stiffness, used to calculate the stress at a point, depends uniquely on the strain history at that point only, failure would localise in a zone of zero width leading to mesh-dependent results in the context of finite element analyses. Various researchers investigated this effect from a mathematical point of view by considering a one-dimensional rod subjected to longitudinal tension waves of constant amplitude that propagate from its edges to the middle of the structure resulting in a constantly increasing wave amplitude in the midpoint of the bar (Bazant and Pijaudier-Cabot, 1988; Rizzi et al., 1995; Liebe and Willam, 2001). During material softening, failure localised in a zone in the centre of the bar, such that waves with longer wavelengths than the localisation zone width cannot propagate (Pijaudier-Cabot and Benallal, 1993). A localisation zone of zero width would mean that wave propagation with real velocity is not possible in this medium and failure occurs with zero fracture energy. In the context of finite element analysis these constitutive laws would lead to mesh dependence because failure localises always in a single element zone and the total fracture energy would depend on the width of the localisation zone. Furthermore, local constitutive models fail to describe the localisation of failure in a finite zone, which is observed in experiments (Grégoire et al., 2015).

2.3.1 Nonlocal constitutive model

Nonlocal material models describe the stress state at a material point based on the strain state of all material points in its vicinity. This is a way to describe phenomeno-

logically interactions between material points taking place in lower scales due to friction, interparticle forces and micro-crack interactions (Kröner, 1967). If correctly formulated, nonlocal models describe the FPZ by regularised mesh-independent strain profiles (Pamin and de Borst, 1998; Bažant and Jirásek, 2002; Huerta et al., 2002).

Nonlocal models are divided in gradient and integral-type models depending on their formulation (Eringen and Edelen, 1972; Aifantis, 1984). Gradient formulations are separated in explicit, where the nonlocal state variable is a function of the spatial derivatives of the field of the local state variable, and implicit according to which the nonlocal variable is the solution of a second order nonhomogeneous differential equation (Mühlhaus and Alfantis, 1991; Fleck et al., 1994). In integral-type nonlocal models the nonlocal variable at a receiver material point is evaluated as a weighted average of the state variable at all source points in its vicinity (Pijaudier-Cabot and Bažant, 1987). The weight of the contribution of each material point is provided by the weight function, which is a decreasing function of the distance between the source and the receiver points. The weight function is formulated such that homogeneous state variable fields are preserved. Typical weight functions are the Gauss, Green and the Bell-shaped truncated polynomial functions. The width of the final failure zones depends on the value of the interaction radius, which is a parameter of the weight function. Peerlings et al. (1996) compared the solutions of a 1D bar subjected to tension, analysed by an implicit gradient and and an integral-type nonlocal model. It was shown, that the solution provided by applying an integral-type nonlocal model with a Green-type weight function is same solution to the one from an implicit gradient type model. Grassl and Jirásek (2010) compared the dissipated energy profiles from different weight functions for a one-dimensional specimen subjected to tension against meso-scale analyses results of a periodic specimen subjected to direct tension. It was illustrated, that integral-type nonlocal models with the Green-type weight function result in dissipated energy density profiles that fit better the meso-scale analyses results.

Original formulations of integral-type nonlocal models result in excessive spurious energy dissipation distributed in wide zones close to non-convex boundaries, such as notches. This effect is followed by an overestimation of the experimental peak load and fracture energy (Jirásek et al., 2004). The main reason are the nonlocal contributions of the undamaged source points around the notch that lead to a reduction of the nonlocal equivalent strains of the receiver points lying close to the notch tip. The evolution of the damage variables at these receiver points does not follow the increase of the stress that rises to very high levels and an increased spurious dissipation is observed. Another reason are the multi-axial stress states observed in notched specimens due to the significant stresses along the other two principal axes. This effect is more pronounced for material points lying in the vicinity of the notch tip. A different formulation of the equivalent strain could therefore result in a reduction of the analytically

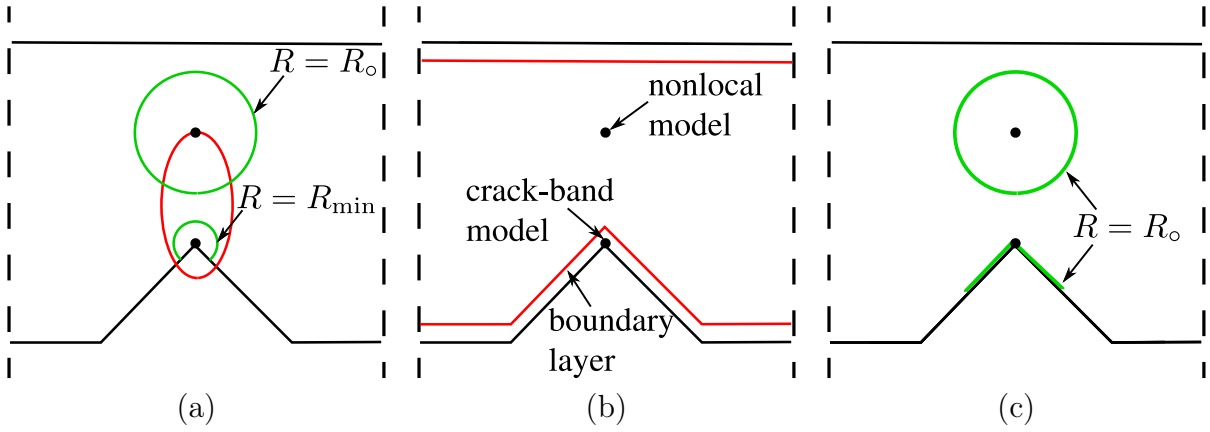

Figure 2.3: Schematic overview of distance-based nonlocal approaches for a V-Notched beam: (a) Bolander and Hikosaka (1995), (b) Bažant et al. (2010), (c) Krayani et al. (2009).

observed peak load (Jirásek and Bauer, 2012). In the present thesis, different nonlocal averaging approaches that can be applied to resolve this problem are investigated.

The first group of nonlocal models are referred to as distance-based approaches and involve modifying the interaction radius depending on the distance of the receiver point from the boundaries (Figure 2.3). Bolander and Hikosaka (1995) applied this concept for the material points within a predefined ellipse around a sharp notch. The interaction radius increased for increasing distance of the receiver point from a minimum value on the notch tip to the maximum value on the ellipse boundaries. A hybrid approach approach was proposed to analyse a beam subjected to three-point bending in Bažant et al. (2010). The material points close to the specimen boundaries were considered to form an outer layer, whose constitutive response was modelled by a crack-band model calibrated according to a stress-inelastic displacement law (see Section 2.3.2). Failure in the inner part of the structure was modelled by a nonlocal model. Krayani et al. (2009) assumed a symmetric equivalent strain field on the other side of the boundary. In this approach, the response of the material points close to the boundaries is almost local despite the use of a nonlocal material model because only the contributions from source points lying on the boundary are taken into account. In a finite element analysis the accuracy of the calculated values of the nonlocal parameters depends on the number of material points that are taken into account during nonlocal averaging. Hence, for a coarse finite element mesh this approach could lead to mesh-dependent results.

In stress-based approaches, nonlocal averaging is modified according to the stress state of the material points (Figure 2.4). Planas et al. (1993) argued that the most critical nonlocal contributions should be from source points lying across the FPZ and proposed that the weights of the nonlocal interactions of material points along the compressive principal axes should be reduced. In the case of notches or other physical boundaries, the stress-based approaches incorporate the influence of boundaries through the stress

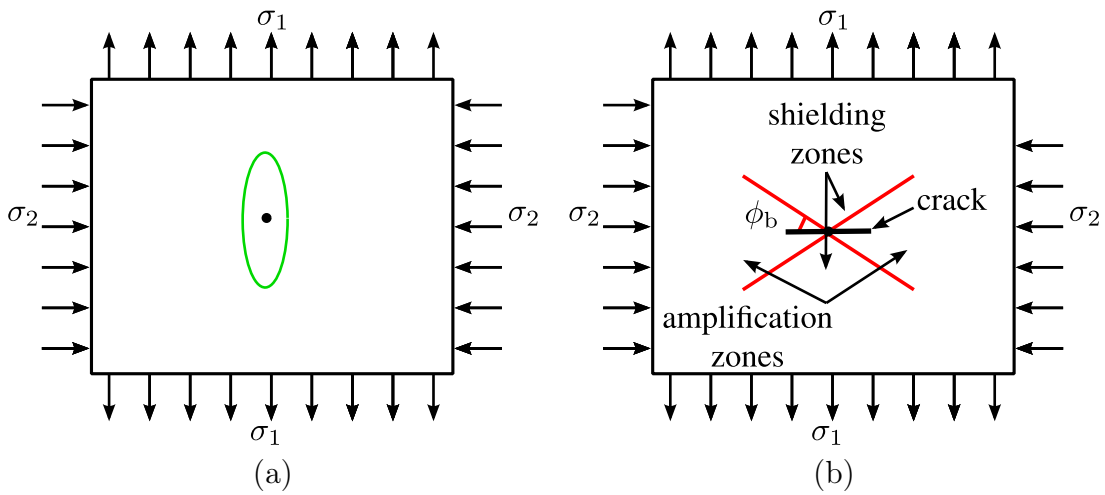

Figure 2.4: Schematic overview of the stress-based nonlocal approaches for a specimen subjected to tension with Poisson's ratio equal to zero. (a) Single nonlocal weights contour for a source point for different receiver points lying around it at the same distance (Giry et al., 2011). (b) Interaction zones of a crack according to the crack-interactions model (Bažant, 1994).

field. For example, on a free boundary of the specimen with no applied surface tractions, the principal stress directions are normal and tangential to the boundary and the principal stress perpendicular to the boundary vanishes. If the principal stress along the boundary is tensile, the internal length is reduced in the perpendicular direction. This produces a similar effect as in the distance-based approaches. Probably the first stress-based approach, motivated by the interactions between microcracks was formulated by Bažant (1994) and was analysed in a simplified form in Jirásek and Bažant (1994). In these studies the effective local stress state of both the source point with respect to the receiver point influenced the weight of its contribution resulting in amplification and shielding zones. In addition the damage-based approach presented in **?** inspired the work by Giry et al. (2011), who formulated a stress-based weight function by modifying the weight of source material points according to their stress state. A similar but more efficient approach will be presented in the present thesis which is based on the stress state of the receiver point.

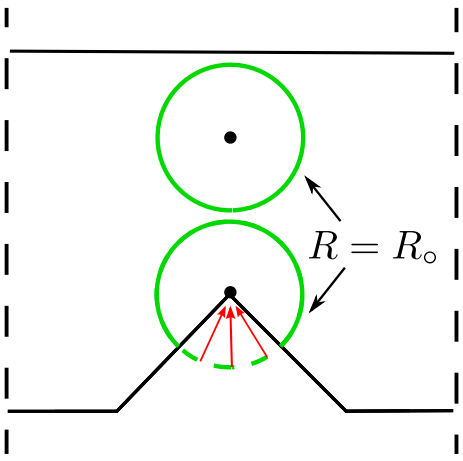

Figure 2.5: Illustration of the local complement method (Borino et al., 2002).

Moreover, an additional set of approaches is investigated that do not break the symmetry of the weight function with respect to the coordinates of the receiver and the source points (Borino et al., 2002). In a formulation, known as the local complement method, the calculated weight depends solely on the distance between the two points and the boundaries are taken into account by increasing the local contribution of the receiver point. This is achieved by increasing the weight of the local contribution to compensate for the missing part of the integration domain (Figure **??**). The nonlocal state variable is then calculated either as the arithmetic or the geometrical mean of the local and the nonlocal contributions (Borino et al., 2003; Grassl and Jirásek, 2008). Alternatively, material models, based on damage mechanics and perfect plasticity, do not break the symmetry of the weight function and may result in a reduction of the dissipation close to boundaries because the stresses are limited by the yield surface. Jirásek and Rolshoven (2003) showed that nonlocal perfectly plastic models result in localisation in a zone of zero width. In overnonlocal models (Vermeer and Brinkgreve, 1994), the state variables are determined from a linear combination of the nonlocal and the local variables. Localisation analysis on these models illustrated that mesh independent formulations are only the ones, where local and nonlocal contributions are multiplied by a negative and a positive factor, respectively (Di Luzio and Bažant, 2005). In addition, Grassl and Jirásek (2010) argued that these formulations should be applied in a damage-plasticity model in order to have a mesh-independent description of the plastic strains.

The boundaries should also be integrated in the model at a structural level. Jirásek et al. (2004) investigated several alternative representations of the boundaries of notched compact tension specimens. The notch was analysed by a fully damaged material, resulting in an unjustified dependence of the load-displacement curve on the notch thickness when the nonlocal variable was set equal to the average of the local damage energy release rate. The reason is that the damage release rate in the notched area is inversely proportional to the square of the notch thickness and this term does not cancel out during nonlocal averaging across the notch thickness leading to results sensitive to the notch geometry. In an alternative approach, boundaries were considered as nonlocal barriers blocking nonlocal interactions between points lying on either sides of the notch. This idea is physically motivated because there is no linear path connecting the two points that is entirely within the specimen and taking into account the lengths of alternative paths would result in negligible weights. This concept was not very efficient in decreasing the energy dissipation around the notch as the points that dissipate most of the energy are above the notch tip and are directly connected with each other. This approach will be applied in all nonlocal simulations in the present thesis due to its physical motivation.

A group of alternative averaging schemes, reported in the literature, were characterised

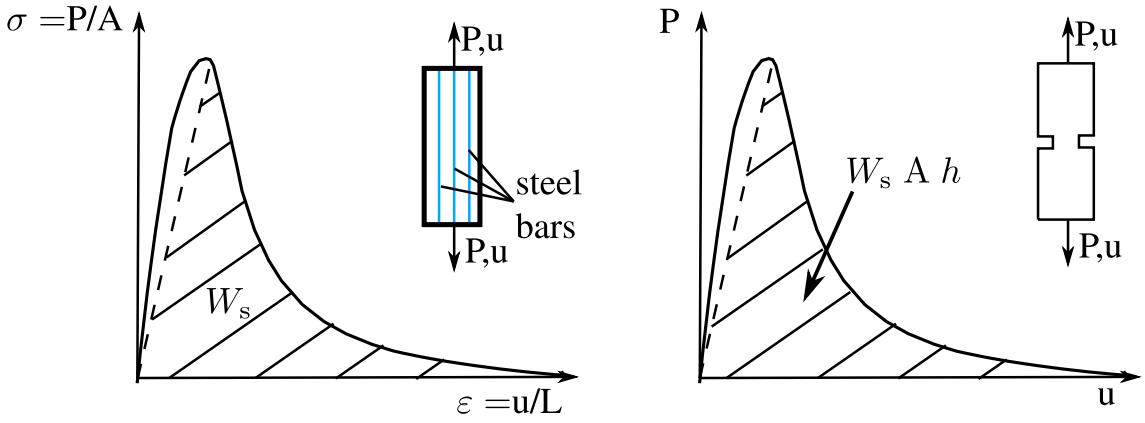

Figure 2.6: Schematic overview of the calibration methodology proposed in Bažant and Pijaudier-Cabot (1989). The cross-sectional area for both both specimens in the failure zone is equal to A. The width of the failure zone is equal to h.

by either a complex concept or by an increased computational load. These models will not be included in the analyses performed in the present thesis but are briefly reviewed. A set of approaches focus on the paths that the nonlocal contributions follow from the source to the receiver point in order to define the weight function (Ganghoffer and de Borst, 2000; Polizzotto et al., 2006). These approaches are computationally intensive due to the large number of potential paths that need to be investigated. Furthermore, Rojas-Solano et al. (2013) defined the weight function by calculating the weights of a source point for all receiver points based on the distribution of the state variable from the solution of an expanding elastic sphere centered the source point.

Another major topic in nonlocal models is the calibration of the interaction radius that determines the width of the final failure zones. A group of calibration approaches rely on reconstructing the dissipated energy profiles and strain profiles based on experimental results in order to determine the size of the FPZ width. Bažant and Pijaudier-Cabot (1989) investigated a Double Edge Notched (DEN) and an unnotched specimen subjected to tension (Figure 2.6). In the unnotched specimen localisation of failure was prevented by placing steel bars. The load-displacement curves were recorded for both specimens and were converted for the case of the unnotched specimen to stress-strain curves by dividing the load and the displacement by the specimen cross-sectional area and length, respectively. The experimental dissipated energy profile was reconstructed in both cases by considering that the global fracture energy is homogeneously distributed within the FPZ. The width of the FPZ was then calculated by dividing the integral of the load-displacement curve of the notched specimen with the cross-sectional area and with the integral of the stress-strain diagram of the unnotched one. The strain profile at peak was reconstructed for the notched specimen by assuming all material points within the FPZ are equally strained. A nonlocal model was used to analyse an one-dimensional specimen subjected to tension and was calibrated so that the integral of the strain profile at peak stress fits the integral of the reconstructed strain profile. This methodology does not account for the nonlinear dissipated energy and

strain distributions within the FPZ. Moreover, the FPZ is not uniquely determined as it depends on the constitutive laws used in the calibration. In the present thesis a new calibration methodology is proposed, which is based on the final crack patterns of notched specimens.

Another group of theoretical approaches proposed for explicit gradient-type nonlocal models were based on the Representative Volume Element (RVE) concept (Frantziskonis, 1995; Gitman et al., 2005). The RVE corresponds to the minimum volume of the laboratory scale specimen, whose experimental results can still be regarded as representative for the continuum. The RVE concept was applied for the calibration of the gradient models in the elastic regime by Gitman et al. (2006). However, as it was illustrated by Gitman et al. (2008), an RVE cannot be found in the softening regime.

Alternatively, calibration strategies based on inverse optimisation techniques may be applied. According to these approaches, the interaction radius is defined by minimising an objective function which is the sum of the difference between experimental variables and the corresponding analytical ones. The selection of the set of variables used in the calibration is important as it might lead to an ill-posed problem characterised by convergence problems due to the existence of multiple or no solutions (Carmeliet, 1999). When the results of a single experiment are used in the calibration, both global and local information need to be considered in the form of the load-displacement curve and local displacements at material points lying inside and outside the FPZ (Mahnken and Kuhl, 1999). Results from experimental campaigns with geometrically similar specimens can be used in the calibration of nonlocal models by using both global load-displacement curves and local displacements (Bellégo et al., 2003; Iacono et al., 2006). Iacono et al. (2008) calibrated a nonlocal model against the experimental results from specimens of different sizes subjected to three-point bending tests and uniaxial tension. It was illustrated that calibration provided unsatisfactory predictions for the tensile tests, which could be attributed to structural effects that influence the calibration process. Hence, a successful calibration algorithm needs to be based on both local and global parameters.

The present section focused on different nonlocal approaches formulated in the literature and on the calibration of nonlocal models. Among the different groups of nonlocal models, that were presented, the distance-based, the stress-based and the local complement formulations were based on simple concepts and took into account the influence of boundaries either implicitly or explicitly in the averaging scheme. In Chapter 4 nonlocal models belonging in these groups are applied to model different types of boundaries in order to evaluate their performance. Moreover, calibration methodologies based on theoretical approaches, inverse optimisation techniques and the reconstruction of

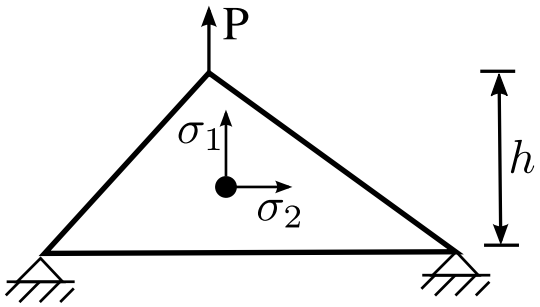

Figure 2.7: Schematic overview of the crack-band width h of the crack-band approach for the case of a triangular element and Poisson's ratio equal to zero.

the experimental dissipated energy profiles were discussed. It was concluded from the literature review that both global and local variables should be included in the calibration procedure in order to take into account the local dissipation within the FPZ during failure. Therefore, the calibration methodology that is presented in Chapter 5 is based on the experimental global load-displacement relationship and the local standard deviation of the experimental final crack patterns from the mean crack plane.

2.3.2 Crack-band approach

The initial motivation of this theory was that material failure can be modelled in tension as a band of parallel, densely distributed microcracks (Bažant and Oh, 1983). In crack-band models, failure localises in a single row of finite elements and the stress-strain relationship is adjusted based on the width of the band to match stress-inelastic displacement law. In Jirásek and Grassl (2008), it was observed that analysing a structured mesh using the crack band approach results in failure zones that follow the mesh lines. This phenomenon is defined in the literature as directional mesh bias. Jirásek and Bauer (2012) compared different definitions of the crack-band width in tension proposed in the literature. Beams subjected to three-point bending were analysed and it was concluded that independently of the number of Gauss Points per element the crack band width should be equal to the projected length at the centre of the element along the first principal strain axis at the initiation of damage (Figure 2.7).

In Bažant and Xiang (1997), the crack-band approach was extended in compression and shear failure by considering a band of splitting cracks that propagate perpendicular or at an angle to the loading axis but there is no consensus on how to define this band. A group of researchers suggested, that a stress-strain law is sufficient for providing mesh-independent results in compression (Grassl and Jirásek, 2006a; Grassl et al., 2013). Recently, Červenka et al. (2014) performed a mesh study by analysing cylindrical specimens subjected to compression that were investigated by Nakamura and Higai

(2001). The analytical results were shown to be mesh-dependent. The main reason of this response is the dense spacing of the cracks which means that failure localised in much smaller zones than the ones considered in stress-inelastic displacement law. This was illustrated in the contour plots of damage where failure localised in multi-element zones.

Chapter 3

Modelling approaches

Four macroscopic and one meso-scale approach are presented, which are applied in the subsequent chapters to model concrete failure. The macroscopic approaches are formulated within the context of continuum mechanics and the nonlinear material response is described by either nonlocal damage or nonlocal damage-plasticity constitutive laws. These material models are suitable for the nonlinear analysis of specimens, where tensile failure dominates, and are simpler than the advanced macroscopic damage-plasticity law CDPM2 presented in Chapter 6. In the meso-scale approach, concrete is considered as a heterogeneous three-phase composite consisting of mortar, aggregates and Interfacial Transition Zones (ITZs) between the two other phases. The meso-structure is modelled explicitly by a lattice approach combined with an isotropic damage mechanics constitutive law. Autocorrelated random fields are applied to model the spatial variation of the material properties. Special techniques are presented to eliminate the influence of the boundary conditions. These techniques are used to calibrate the macroscopic constitutive laws based on meso-scale analyses results.

3.1 Macroscopic approaches

3.1.1 Nonlocal isotropic damage models

In this section two damage constitutive laws are presented, that are based on isotropic damage mechanics. They are referred to as nonlocal isotropic damage model A and B and are used in Chapters 4 and 5, respectively. The stress-strain relationship is in both models

$$\boldsymbol{\sigma} = (1-\omega)\bar{\boldsymbol{\sigma}} = (1-\omega)\boldsymbol{D}_{\mathrm{e}} : \boldsymbol{\varepsilon} \tag{3.1}$$

where $\boldsymbol{\sigma}$ is the total stress tensor, ω is the damage variable, $\bar{\boldsymbol{\sigma}}$ is the effective stress tensor, $\boldsymbol{\varepsilon}$ is the strain and $\boldsymbol{D}_{\mathrm{e}}$ is the isotropic elastic stiffness that depends on Young's modulus E and Poisson's ratio ν.

Damage ω is determined by the damage function, which depends on the history variable κ_{d}. For the nonlocal isotropic damage model A,

$$\omega(\kappa_{\mathrm{d}}) = \begin{cases} 1 - \exp\left(-\dfrac{1}{m_{\mathrm{d}}}\left(\dfrac{\kappa_{\mathrm{d}}}{\varepsilon_0}\right)^{m_{\mathrm{d}}}\right) & , \kappa_{\mathrm{d}} \leq \varepsilon_1 \\ 1 - \dfrac{\varepsilon_3}{\kappa_{\mathrm{d}}} \exp\left(-\dfrac{\kappa_{\mathrm{d}} - \varepsilon_1}{\varepsilon_{\mathrm{f}}\left[1 + \left(\dfrac{\kappa_{\mathrm{d}} - \varepsilon_1}{\varepsilon_2}\right)^n\right]}\right) & , \kappa_{\mathrm{d}} > \varepsilon_1 \end{cases} \tag{3.2}$$

where

$$m_{\mathrm{d}} = \frac{1}{\ln(E\varepsilon_0/f_{\mathrm{t}})} \tag{3.3}$$

and f_{t} is the uniaxial tensile strength. Parameter ε_0 is the axial strain at peak stress, and ε_1, ε_2 and n are additional parameters that control the softening part of the stress-strain diagram.

Furthermore,

$$\varepsilon_{\mathrm{f}} = \frac{\varepsilon_1}{(\varepsilon_1/\varepsilon_0)^{m_{\mathrm{d}}} - 1} \tag{3.4}$$

and

$$\varepsilon_3 = \varepsilon_1 \exp\left(-\frac{1}{m_{\mathrm{d}}}\left(\frac{\varepsilon_1}{\varepsilon_0}\right)^{m_{\mathrm{d}}}\right) \tag{3.5}$$

This damage model exhibits pre- and post-peak nonlinearities in uniaxial tension as it is illustrated for the 1D case in Figure 3.1 (a).

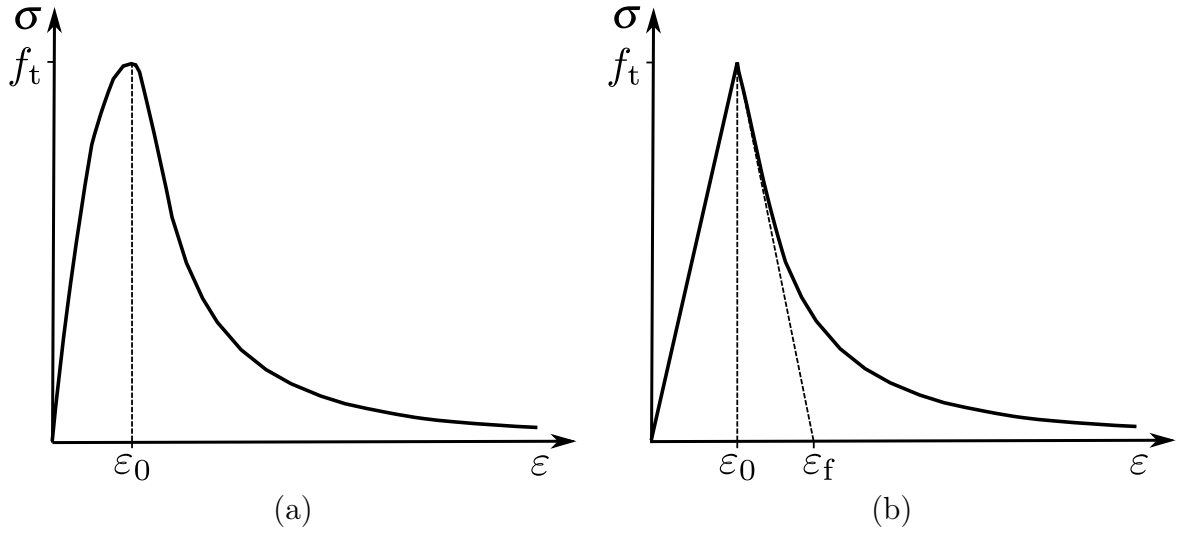

Figure 3.1: Schematic representation of the stress-strain relationship of the (a) nonlocal isotropic damage model A and the (b) nonlocal isotropic damage model B

In nonlocal isotropic damage model B, the function for ω is

$$\omega(\kappa_\mathrm{d}) = \begin{cases} 0 & , \kappa_\mathrm{d} \leq \varepsilon_\mathrm{o} \\ 1 - \left(\dfrac{\varepsilon_0}{\kappa_\mathrm{d}}\right) \exp\left(-\dfrac{\kappa_\mathrm{d} - \varepsilon_0}{\varepsilon_\mathrm{f} - \varepsilon_0}\right) & , \kappa_\mathrm{d} > \varepsilon_\mathrm{o} \end{cases} \tag{3.6}$$

Here, ε_0 is again the strain, at which peak stress is reached, and ε_f controls the slope of the softening curve at peak stress (Figure 3.1 (b)).

The history variable κ_d, used in (3.2) and (3.6) to obtain the damage parameter, represents the maximum level of nonlocal equivalent strain $\bar{\varepsilon}_\mathrm{eq}$ reached in the history of the material. It is determined by the loading-unloading conditions

$$f_\mathrm{d} \leq 0,\ \dot{\kappa}_\mathrm{d} \geq 0,\ \dot{\kappa}_\mathrm{d} f_\mathrm{d} = 0 \tag{3.7}$$

in which

$$f_\mathrm{d}(\bar{\varepsilon}_\mathrm{eq}, \kappa_\mathrm{d}) = \bar{\varepsilon}_\mathrm{eq} - \kappa_\mathrm{d} \tag{3.8}$$

is the damage loading function.

The nonlocal equivalent strain $\bar{\varepsilon}_\mathrm{eq}$ is evaluated as

$$\bar{\varepsilon}_\mathrm{eq}(\boldsymbol{x}) = \int_\mathrm{V} \alpha(\boldsymbol{x}, \boldsymbol{\xi})\, \varepsilon_\mathrm{eq}(\boldsymbol{\xi})\, \mathrm{d}\boldsymbol{\xi} \tag{3.9}$$

At a point $\boldsymbol{x}$, ε_eq is the weighted average of the value of the local equivalent strain ε_eq at all points $\boldsymbol{\xi}$ in the vicinity of $\boldsymbol{x}$ within the integration domain V (Figure 3.2(a)). The weight function $\alpha(\boldsymbol{x}, \boldsymbol{\xi})$ used in the nonlocal models should not modify uniform fields after averaging. According to the standard scaling approach, this is achieved by

normalising the original weight function $\alpha_0(\boldsymbol{x}, \boldsymbol{\xi})$ by its integral over the integration domain V (Pijaudier-Cabot and Bažant, 1987), as

$$\alpha(\boldsymbol{x}, \boldsymbol{\xi}) = \frac{\alpha_0(\boldsymbol{x}, \boldsymbol{\xi})}{\int\limits_{\mathrm{V}} \alpha_0(\boldsymbol{x}, \boldsymbol{\xi})\, \mathrm{d}\boldsymbol{\xi}} \tag{3.10}$$

In the present thesis, $\alpha_0(\boldsymbol{x}, \boldsymbol{\xi})$ corresponds to an exponential (Green-type) function

$$\alpha_0(\boldsymbol{x}, \boldsymbol{\xi}) = \exp\left(-\frac{\|\boldsymbol{x} - \boldsymbol{\xi}\|}{R}\right) \tag{3.11}$$

Here, R is the interaction radius, that determines the slope of the weight function α_0 for $\boldsymbol{\xi} \equiv \boldsymbol{x}$ and controls the size of the final failure zones (Figure 3.2(b)).

Modifications of the standard scaling scheme in order to model boundaries are presented in Chapter 4.

For the nonlocal isotropic damage model A, the formulation of the local equivalent strain $\varepsilon_{\mathrm{eq}}$, introduced in (3.9), is

$$\varepsilon_{\mathrm{eq}} = \frac{1}{E} \max_{I=1,2,3} \bar{\sigma}_I \tag{3.12}$$

where $\bar{\sigma}_I$ denotes the Ith principal component of the effective stress $\bar{\boldsymbol{\sigma}}$ introduced in (3.1). This equivalent strain formulation results in a Rankine strength envelope (Figure 3.3(a)). The damage law and the failure surface selected for this model result in a similar stress-strain behavior to the one provided by the damage-plasticity model presented in Section 3.1.2. Both material models will be applied in the comparative study presented in Chapter 4.

In nonlocal isotropic damage model B, $\varepsilon_{\mathrm{eq}}$ is formulated as

$$\varepsilon_{\mathrm{eq}} = \frac{1}{E} \sqrt{\sum_{I=1}^{3} < \bar{\sigma}_I >_+^2} \tag{3.13}$$

where $< \, . \, >_+$ are the MacAuley brackets (positive part operator). This equivalent strain formulation results in a more detailed description of the strength envelope for biaxial stress states, which is important for testing the calibration strategy shown in Chapter 5 (Figure 3.3(b)).

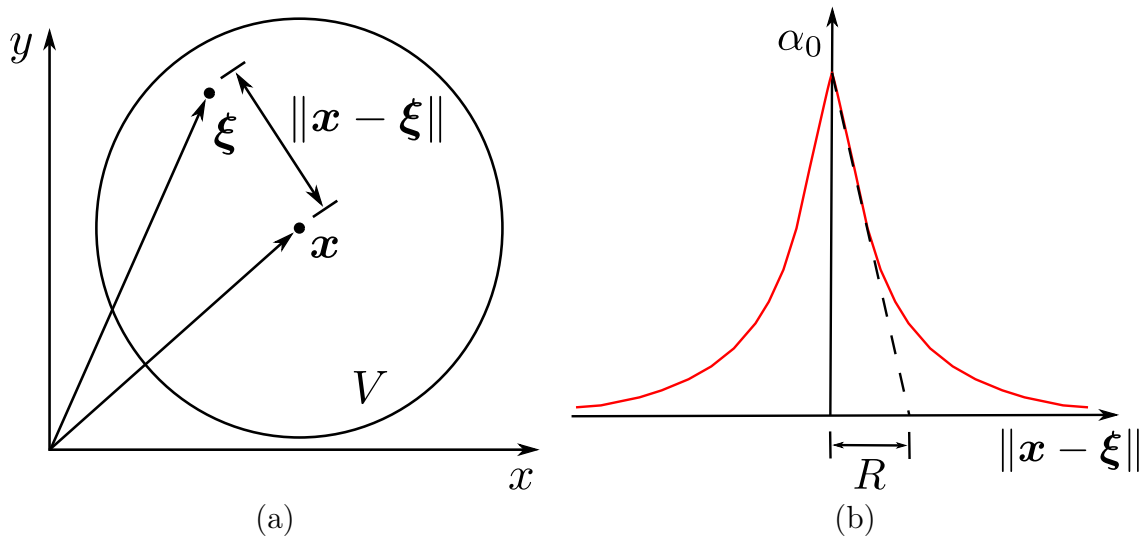

Figure 3.2: (a) Schematic representation of the nonlocal concept. (b) Exponential-type weight function α_0.

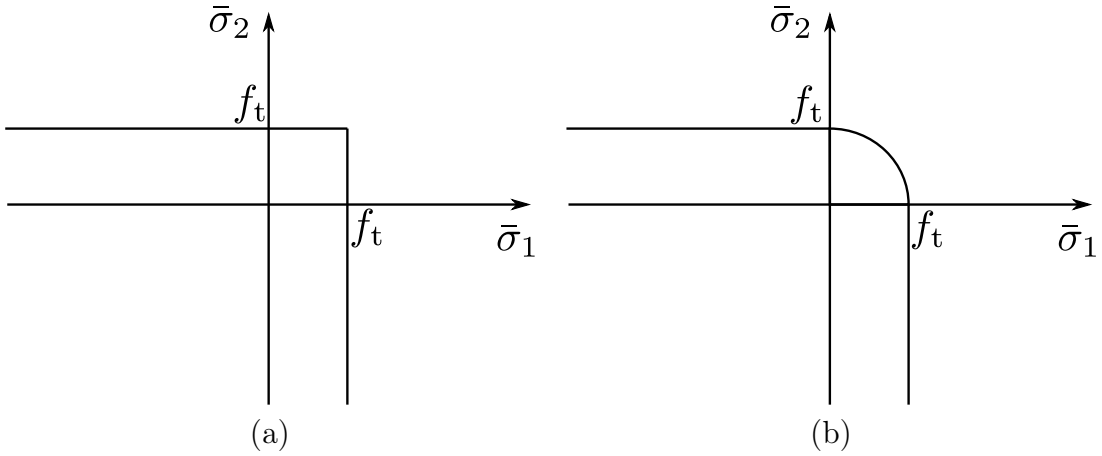

Figure 3.3: Plane stress representation of the damage surface at the onset of damage ($\varepsilon_{\text{eq}} = \varepsilon_0$) for the (a) nonlocal isotropic damage law A and (b) nonlocal isotropic damage law B.

3.1.2 Nonlocal damage-plasticity model

The other two macroscopic constitutive approaches are based on both isotropic damage mechanics and hardening plasticity. The constitutive relationship is

$$\boldsymbol{\sigma} = (1-\omega)\bar{\boldsymbol{\sigma}} = (1-\omega)\boldsymbol{D}_{\mathrm{e}} : (\boldsymbol{\varepsilon} - \boldsymbol{\varepsilon}_{\mathrm{p}}) \tag{3.14}$$

where $\boldsymbol{\varepsilon}_{\mathrm{p}}$ is the plastic strain. The plasticity part is formulated in the effective stress space. The domain of admissible stress states is described by the yield function $f_{\mathrm{p}}(\bar{\boldsymbol{\sigma}}, \sigma_{\mathrm{y}})$ that corresponds to a Rankine failure surface:

$$f_{\mathrm{p}}(\bar{\boldsymbol{\sigma}}, \sigma_{\mathrm{y}}) = \max_{I=1,2,3} < \bar{\sigma}_I >_+ - \sigma_{\mathrm{y}} \tag{3.15}$$

Here, σ_{y} is the yield stress, which is given by the hardening law

$$\sigma_{\mathrm{y}}(\kappa_{\mathrm{p}}) = \begin{cases} E_0 \kappa_{\mathrm{p}} \exp\left(-\dfrac{1}{m_{\mathrm{d}}}\left(\dfrac{\kappa_{\mathrm{d}}}{\varepsilon_{\mathrm{p,max}}}\right)^{m_{\mathrm{p}}}\right) & , \kappa_{\mathrm{p}} \leq \varepsilon_{\mathrm{p,max}} \\ f_{\mathrm{t}} & , \kappa_{\mathrm{p}} > \varepsilon_{\mathrm{p,max}} \end{cases} \tag{3.16}$$

where $\varepsilon_{\mathrm{p,max}}$ is the plastic strain at peak stress and κ_{p} is the plastic hardening variable (cumulative plastic strain) defined in rate form as $\dot{\kappa}_{\mathrm{p}} = \|\dot{\boldsymbol{\varepsilon}}_{\mathrm{p}}\|$. Exponent m_{p} is calculated as

$$m_{\mathrm{p}} = \frac{1}{\ln(E_0 \varepsilon_{\mathrm{p,max}} / f_{\mathrm{t}})} \tag{3.17}$$

The exponential terms in the first branches of the damage function of the nonlocal isotropic damage law, introduced in (3.2), and the hardening laws of the present constitutive laws in (3.16) are similar. However, the damage parameter used in the former model relates stresses to total strains, whereas in the present model the hardening law describes the effective stress-plastic strain relationship. Consequently, parameter E_0 in (3.16), is an additional model parameter, which is independent of the Young's modulus E used in (3.3). It corresponds to the initial hardening modulus and its value is typically very high to ensure that the nonlinearity at low stress levels is negligible.

The loading-unloading conditions of the plasticity part are

$$f_{\mathrm{p}} \leq 0,\ \dot{\lambda} \geq 0,\ \dot{\lambda} f_{\mathrm{p}} = 0 \tag{3.18}$$

In the damage part, the damage variable ω in (3.14) is determined by

$$\omega(\kappa_{\mathrm{d}}) = \begin{cases} 0 & , \kappa_{\mathrm{d}} \leq 0 \\ 1 - d_5 \exp(-d_1 (\kappa_{\mathrm{d}})^{d_2}) - (1-d_5)\exp(-d_3(\kappa_{\mathrm{d}})^{d_4}) & , \kappa_{\mathrm{d}} > 0 \end{cases} \tag{3.19}$$

with dimensionless parameters d_1 to d_5. The model parameters are calibrated according to the procedure described in Section 4.2. Variable κ_d is given by

$$\kappa_\mathrm{d} = \frac{\hat{\kappa}_\mathrm{p} - \varepsilon_\mathrm{p,max}}{\varepsilon_\mathrm{p,max}} \tag{3.20}$$

in which

$$\hat{\kappa}_\mathrm{p} = m\bar{\kappa}_\mathrm{p} + (1-m)\kappa_\mathrm{p} \tag{3.21}$$

Here, $\bar{\kappa}_\mathrm{p}$ is the nonlocal cumulative plastic strain, calculated as

$$\bar{\kappa}_\mathrm{p}(\boldsymbol{x}) = \int_\mathrm{V} \alpha(\boldsymbol{x},\boldsymbol{\xi})\, \kappa_\mathrm{p}(\boldsymbol{\xi})\, \mathrm{d}\boldsymbol{\xi} \tag{3.22}$$

where $\alpha(\boldsymbol{x},\boldsymbol{\xi})$ is the weight function defined in (3.10) and m is an additional model parameter. For $m = 1$ the nonlocal formulation is recovered and this model is called in the present thesis nonlocal damage-plasticity model. In Jirásek and Rolshoven (2003), it was shown that this model provides mesh-dependent results for a hardening law with constant yield stress in the post-peak. This issue is resolved if a over-nonlocal formulation is applied in which m should be larger than 1 as shown in Di Luzio and Bažant (2005). This approach was introduced in the context of nonlocal plasticity by Vermeer and Brinkgreve (1994) and was adapted to nonlocal damage-plasticity by Grassl and Jirásek (2006a). In the second model, defined in the present thesis as over-nonlocal damage-plasticity model, m is set equal to 2, which is the value used in a similar study in Grassl and Jirásek (2006a).

3.2 Meso-scale approach

In the meso-scale approach, the material meso-structure is analysed by a two-dimensional lattice of structural elements, as described in (Grassl and Jirásek, 2010). The lattice nodes are generated randomly subject to the constraint of minimum distance d_min (Zubelewicz and Bažant, 1987). A Delaunay triangulation is found for this set of nodes to define the lattice edges. The cross-sections of the lattice elements are the edges of the Voronoi diagram, which is the dual graph to the analysed lattice (Figure 3.4 (a)).

The meso-scale approach is limited to a two-dimensional plane stress analysis. Each lattice node possesses three degrees of freedom (two translations and one rotation). In the global coordinate system, shown in Figure 3.4(b), the degrees of freedom $\boldsymbol{u}_\mathrm{e} = (u_1, v_1, \phi_1, u_2, v_2, \phi_2)^\mathrm{T}$ are linked to the displacement discontinuities $\boldsymbol{u}_\mathrm{c} = (u_\mathrm{c}, v_\mathrm{c})$ in the

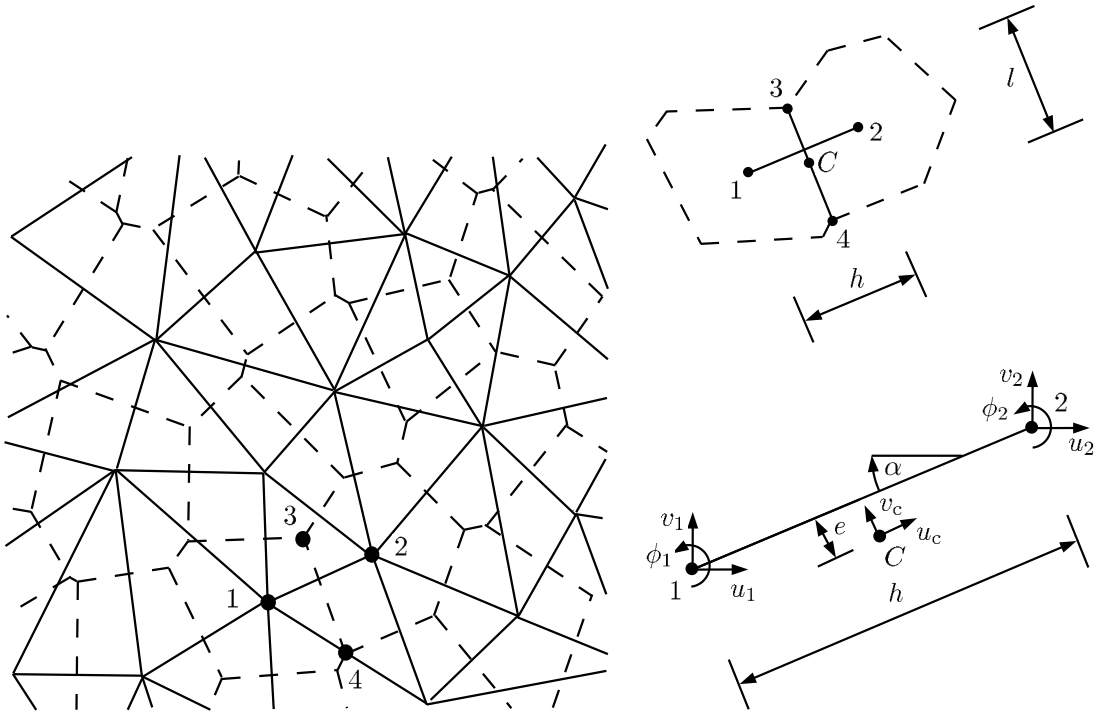

Figure 3.4: (a) Lattice based on Delaunay tessellation based on a random set of points. (b) Lattice element in the global coordinate system.

local coordinate system at Point C, which lies in the centre of a Voronoi cross-section. The relationship is

$$\boldsymbol{u}_{\mathrm{c}} = \boldsymbol{B}\boldsymbol{u}_{\mathrm{e}} \tag{3.23}$$

where

$$\boldsymbol{B} = \begin{bmatrix} -\cos\alpha & -\sin\alpha & -e & \cos\alpha & \sin\alpha & e \\ \sin\alpha & -\cos\alpha & -h/2 & \sin\alpha & \cos\alpha & -h/2 \end{bmatrix} \tag{3.24}$$

The displacement discontinuities $\boldsymbol{u}_{\mathrm{c}}$ are normalised by the length of the lattice element h in order to calculate the strains $\boldsymbol{\varepsilon} = (\varepsilon_{\mathrm{n}}, \varepsilon_s)^T = \boldsymbol{u}_{\mathrm{c}}/h$. The stiffness matrix of a lattice element is calculated in the local coordinate system by

$$\boldsymbol{K} = \frac{l}{h}\boldsymbol{B}^{\mathrm{T}}\boldsymbol{D}\boldsymbol{B} \tag{3.25}$$

where l is the length of the Voronoi segment, h is the length of the lattice element and $\boldsymbol{D}$ is the material stiffness.

An isotropic damage constitutive model is applied to describe the nonlinear stress-strain relationship within the lattice elements and the constitutive relationship is given in

$$\boldsymbol{\sigma} = (1-\omega)\boldsymbol{D}_{\mathrm{e}}\boldsymbol{\varepsilon} = (1-\omega)\bar{\boldsymbol{\sigma}} \tag{3.26}$$

where $\boldsymbol{\sigma} = (\sigma_{\mathrm{n}}, \sigma_{\mathrm{s}})^{\mathrm{T}}$ is the total stress, ω is the damage variable, $\boldsymbol{D}_{\mathrm{e}}$ is the elastic stiffness, $\boldsymbol{\varepsilon} = (\varepsilon_{\mathrm{n}}, \varepsilon_{\mathrm{s}})^{\mathrm{T}}$ is the strain, and $\bar{\boldsymbol{\sigma}} = (\bar{\sigma}_{\mathrm{n}}, \bar{\sigma}_{\mathrm{s}})^{\mathrm{T}}$ is the effective stress.

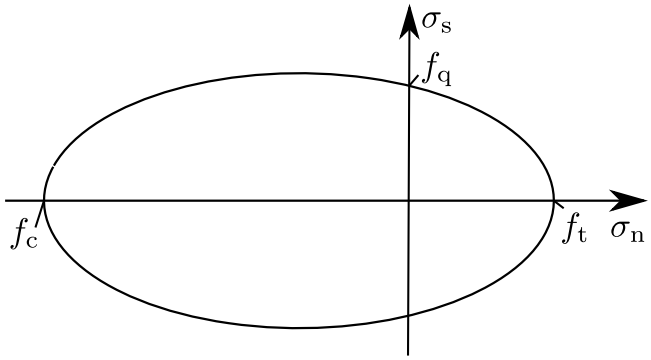

Figure 3.5: Elliptic strength envelope in the nominal stress space at the onset of damage ($\varepsilon_{eq} = \varepsilon_0$).

The elastic stiffness matrix

$$\boldsymbol{D}_e = \begin{bmatrix} E & 0 \\ 0 & \gamma E \end{bmatrix} \tag{3.27}$$

depends on the parameters E and γ that control Young's modulus and Poisson's ratio of the material. A relationship between these parameters and the elastic material properties has been established for a regular lattice for various structures in Griffiths and Mustoe (2001). For plane stress conditions the resulting Poisson's ratio is

$$\nu = \frac{1-\gamma}{3+\gamma} \tag{3.28}$$

and the Young's modulus is

$$E_m = 2E\left(\frac{1+\gamma}{3+\gamma}\right) \tag{3.29}$$

The evolution of the damage parameter ω depends on the equivalent strain ε_{eq} that corresponds to an elliptic strength envelope at the onset of damage (Figure 3.5). For pure tensile loading, the effective stress is limited by tensile strength $f_t = E\varepsilon_0$, whereas for pure compressive loading it is limited by the compressive strength $f_c = cf_t$. In pure shear, total stress is limited by the shear strength $f_q = qf_t$. The damage parameter ω is a function of the history parameter κ_d, which is equal the maximum equivalent strain ε_{eq} reached in the loading history. An exponential softening law is applied to describe the post-peak stress-strain response. The main parameter is w_f, that controls the initial slope of the softening curve and is related to the meso-level fracture energy $G_{ft} = f_t w_f$.

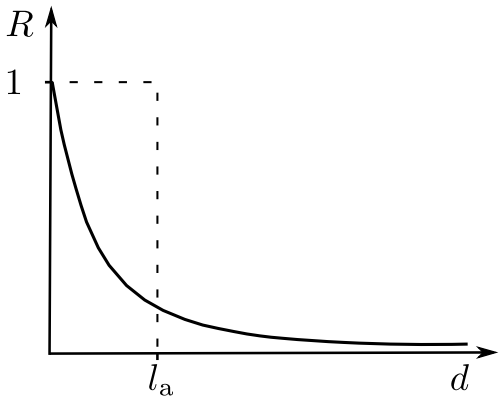

Figure 3.6: Exponential autocorrelation function of separation distance d.

The material heterogeneity is taken into account by mapping the spatially varying material properties to the material parameters of the elements of the lattice. Aggregates with diameters greater than $\phi_{\min}$ are modelled directly assuming linear elastic properties. The random distribution of aggregate diameters ϕ is defined by the cumulative distribution function used in Carpinteri et al. (2004). Aggregates are placed randomly within the specimen, avoiding overlaps with each other. The heterogeneity of the material properties of finer particles is taken into account by autocorrelated Gaussian random fields applied on the tensile strength and the fracture energy. The two random fields are generated based on a spectral representation method and are assumed to be fully correlated (Shinozuka and Jan, 1972; Shinozuka and Deodatis, 1996). In the present thesis, an exponential autocorrelation function is applied, formulated as

$$R(d) = \exp\left(-\frac{d^2}{b^2}\right) \tag{3.30}$$

which for a one-dimensional random field the autocorrelation function is calculated as

$$R(d) = \int_{-\infty}^{\infty} f(x) f(x-d) \mathrm{d}x \tag{3.31}$$

Here, parameter d is the separation distance between two points and x is the spatial coordinate. In 3.30, b is a parameter related to autocorrelation length l_a as

$$b = \frac{2\, l_a}{\sqrt{\pi}} \tag{3.32}$$

The autocorrelation length l_a is independent of the spacing $d_{\min}$ of the lattice nodes (Grassl and Bažant, 2009) and determines the area in which the random field assumes values of comparable magnitude (Figure 3.6). The autocorrelation length is related implicitly to the size of the heterogeneities as it determines the geometry of strong and weak zones within the specimen. A threshold is set in the Gaussian distribution in order to avoid negative values of strength and fracture energy.

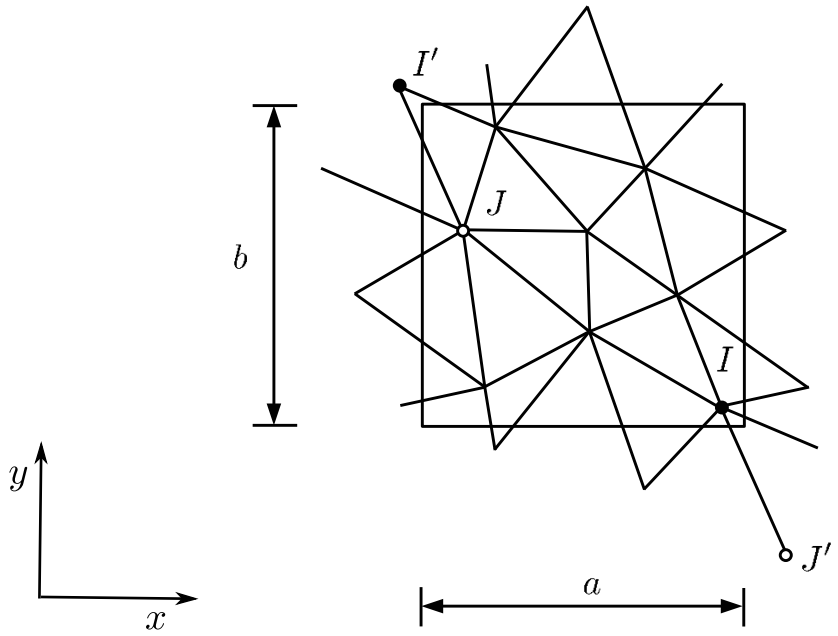

Figure 3.7: Periodic cell.

3.3 Calibration based on the direct tensile test

Special analysis setups are presented for the macroscopic and the meso-scale approaches, where a specimen is subjected to direct tension. The aim is to eliminate the influence of the boundary conditions and to take into account the nonlocal interactions in a multi-dimensional domain.

The meso-scale approach is applied to analyse an initially rectangular computational cell, that is periodically repeated parallel to its sides (Figure 3.7). The final results are neither influenced by the boundary conditions nor by the "wall effect" caused due to the inability of the aggregates to penetrate the boundaries (Unger and Eckardt, 2011). The periodic cell is generated by introducing three extra degrees of freedom (E_{x}, E_{y}, and E_{xy}) to the existing ones of the lattice nodes in order to describe the average strains of the computational cell (Grassl and Jirásek, 2010). Average strains are linked to average stresses. In this specimen, the application of mixed loading conditions is simplified. For example in the uniaxial tension case, the average strain E_{y} is incremented and the average lateral and shear stresses are set to zero.

A periodic mesh is generated such that for every node in an adjacent cell there is a periodic image in the analysed cell. Lattice elements with both nodes inside the computational cell are modelled according to the formulation presented in the previous section. A different formulation is adopted for the lattice elements, which intersect with the cell boundaries connecting nodes of the analysed cell and the of adjacent

cells. The degrees of freedom of the nodes outside the analysed cell are linked to the degrees of freedom of their periodic images inside the cell so that their rotations are equal and their translational degrees of freedom differ by a fixed contribution of the average strains. In Figure 3.7, the kinematics of the node J' of the lattice element IJ' are calculated based on only the displacements of J as

$$\begin{aligned} u_{J'} &= u_J + k_{\mathrm{x}} a E_{\mathrm{x}} + k_{\mathrm{y}} b E_{\mathrm{xy}} \\ v_{J'} &= v_J + k_{\mathrm{y}} b E_{\mathrm{y}} \end{aligned} \tag{3.33}$$

Here k_{x} and k_{y} are integer variables that take values 0, 1 or -1 depending on the position of J' (for this case $k_{\mathrm{x}} = k_{\mathrm{y}} = 1$). The rigid body rotation on the entire lattice is suppressed by constraining the rotation around the out-of-plane axis. The contribution of the average shear strain E_{xy} is therefore considered only for the calculation of the translations along the x-direction. Furthermore, both translations of a lattice node are fixed to suppress the other two rigid body modes. The transformation rule for the displacements of element IJ' is

$$\begin{pmatrix} u_I \\ v_I \\ \phi_I \\ u_{J'} \\ v_{J'} \\ \phi_{J'} \end{pmatrix} = \begin{bmatrix} 1 & 0 & 0 & 0 & 0 & 0 & 0 & 0 & 0 \\ 0 & 1 & 0 & 0 & 0 & 0 & 0 & 0 & 0 \\ 0 & 0 & 1 & 0 & 0 & 0 & 0 & 0 & 0 \\ 0 & 0 & 0 & 1 & 0 & 0 & k_{\mathrm{x}} a & 0 & k_{\mathrm{y}} b \\ 0 & 0 & 0 & 0 & 1 & 0 & 0 & k_{\mathrm{y}} b & 0 \\ 0 & 0 & 0 & 0 & 0 & 1 & 0 & 0 & 0 \end{bmatrix} \begin{pmatrix} u_I \\ v_I \\ \phi_I \\ u_J \\ v_J \\ \phi_J \\ E_{\mathrm{x}} \\ E_{\mathrm{y}} \\ E_{\mathrm{xy}} \end{pmatrix} \tag{3.34}$$

The meso-scale analyses are performed to obtain the mean average stress-average strain curve and the mean dissipated energy density profile parallel to the loading direction. This is not possible by processing the results of a single meso-scale analysis because for the same input there are different potential realisations of the meso-structure, of the auto-correlated random field and the lattice, leading to different results. Therefore, a set of 100 analyses was performed with the same input. As it was shown by Grassl and Jirásek (2010), this is a statistically representative sample to calculate the mean curves.

The location of the damage localisation area is included in the calculation of the dissipated energy density profiles. The position of the localisation zone is different in each meso-scale analysis. The mean profile was calculated by centering the individual curves in the middle of the specimen. Initially, the dissipation density profile was calculated for each meso-scale analysis by integrating along the x-axis and the point of maximum

dissipation was determined. Then, the profile was translated along the y-axis so that the point of maximum dissipation lay on the middle of the specimen. After the translation, the part of the profile outside the cell boundaries was shifted by a length of the periodic cell to fill in the missing one. This procedure is acceptable because the specimen material properties and boundary conditions are periodic.

The equivalent problem is formulated within the finite element framework and is analysed with nonlocal constitutive laws (Figure 3.8). This setup is used in the present thesis for the calibration of nonlocal models. A two-dimensional cell is analysed by a regular mesh of plane stress quadrilateral elements. Kinematic constraints are applied to the horizontal displacements of all nodes along the left boundary of the specimen and the transversal displacements of the nodes lying along the midheight of the specimen. A prescribed horizontal displacement is applied at a single node on the right boundary of the specimen. Additionally, nodal displacements are restrained such that all nodes lying along the same horizontal mesh line have the same transversal displacements and all nodes along the same vertical mesh line share the same horizontal displacement. Hence, the transversal strains are the same at all elements.

During failure, the position of the localised failure zone depends on the location of imperfections introduced within the specimen. In order to ensure that this zone is completely unaffected by the specimen boundaries, an element is slightly weakened in the middle of the specimen to trigger localisation in that area. In this setup, the transversal strain is uniform in the entire specimen and the mean transversal stress is always zero, whereas the resulting local transversal stress becomes nonzero after the onset of localisation. At this loading stage the local transversal stress varies and is typically tensile in the localisation zone and compressive in the rest of the specimen.

The computational effort is reduced by analysing a single row of elements with one integration point per element and by using a modified nonlocal weight function (Figure 3.8). The equivalent strain field is constant along axis s and the weight function formulated in a two-dimensional domain should depend only on one axial coordinate parallel to axis r as given in

$$\begin{aligned}\bar{\varepsilon}_{\mathrm{eq}}\left(x_r, x_s\right) &= \int_{-\infty}^{\infty}\int_{-\infty}^{\infty} \alpha_{\infty}\left(\sqrt{(x_r-\xi_r)^2+(x_s-\xi_s)^2}\right)\varepsilon_{\mathrm{eq}}(\xi_r)\mathrm{d}\xi_{\mathrm{r}}\mathrm{d}\xi_{\mathrm{s}} \\ &= \int_{-\infty}^{\infty} \alpha_{\infty}^{*}\left(x_r-\xi_r\right)\varepsilon_{\mathrm{eq}}(\xi_r)\mathrm{d}\xi_{\mathrm{r}} \end{aligned} \tag{3.35}$$

Setting the origin of the coordinate system at the receiver point, $r=\xi_r$ and $s=\xi_s$ the

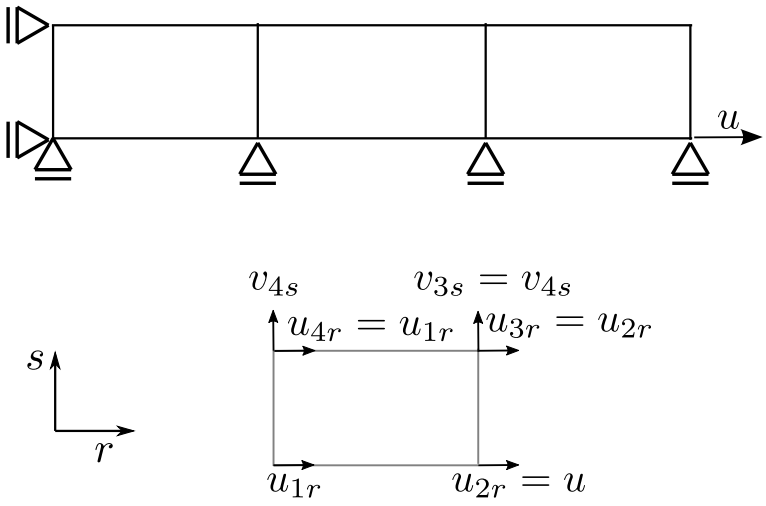

Figure 3.8: Geometry and loading setup of the specimen analysed with the nonlocal models.

weight function $\alpha^*_\infty(x_r - \xi_r)$ in (3.35) becomes

$$\alpha^*_\infty(r) = \int_{-\infty}^{\infty} \alpha_\infty \left(\sqrt{r^2 + s^2}\right) \mathrm{d}s \tag{3.36}$$

as a modified weight function (reduced from 2D to 1D). The integral of (3.36) is evaluated numerically because there is no closed form solution.

In the 3D domain, the modified weight function is formulated for the exponential weight function, given in (3.11), as

$$\alpha^*_\infty(r) = \int_{-\infty}^{\infty} \alpha_\infty \left(\sqrt{r^2 + s^2 + t^2}\right) \mathrm{d}s\, \mathrm{d}t = \frac{1}{4R^2} \exp\left(-\frac{|r|}{R}\right) (R + |r|) \tag{3.37}$$

Here, r, s and t are the distances between the receiver and source points along the x-, y- and z-axis of the coordinate system.

For certain weight functions, such as the Gaussian, the original and the modified weight functions are equal ($\alpha^*_\infty(x_r - \xi_r) = \alpha_\infty(x_r - \xi_r)$). This adjustment increases the efficiency of the model and the nonlocal constitutive laws are calibrated by taking into account nonlocal multi-dimensional interactions.

Chapter 4

Nonlocal boundary approaches

The first topic of the present thesis is the description of non-convex boundaries with nonlocal models and is addressed in this chapter. Nonlocal isotropic damage model A is combined with different averaging procedures and the resulting models are applied to modelling fracture. The macroscopic material models are calibrated by fitting the load-displacement curves and dissipated energy profiles of a specimen subjected to tension to the results of the meso-scale analyses for the direct tension test, as described in Grassl and Jirásek (2010). These analysis setups are used to eliminate the influence of boundaries on the results and to obtain the same solution from all averaging schemes. The calibrated models are applied to two-dimensional simulations of sharp-notched, V-notched and unnotched beams subjected to three-point bending. The performance of the nonlocal models is evaluated by comparing load-displacement curves and dissipated energy profiles along the ligament of the beams with the meso-scale results. As an alternative approach, both damage-plasticity laws, reported in Section 3.1.2, are also included in the comparative study.

4.1 Modified nonlocal approaches for modelling fracture close to boundaries

The nonlocal isotropic damage law A, reported in Section 3.1.2 is combined with different averaging approaches, which are based on three modifications of the standard scaling approach (Figure 4.1), given in (3.10): (i) the distance-based, (ii) the stress-

based, and (iii) the local complement approach. The resulting nonlocal models are characterised by a simple concept, are easy to implement and are computationally efficient.

The distance-based approach, shown in Figure 4.2, is similar to the approach described in Bolander and Hikosaka (1995). Standard scaling is applied to the basic weight function $\alpha_0(\boldsymbol{x}, \boldsymbol{y})$, which depends also on the minimum distance $d(\boldsymbol{x})$ of point $\boldsymbol{x}$ from the specimen boundary (Figure 4.2):

$$\alpha_0(\boldsymbol{x}, \boldsymbol{y}) = \exp\left(-\frac{\|\boldsymbol{x} - \boldsymbol{\xi}\|}{\gamma(\boldsymbol{x}) R}\right) \tag{4.1}$$

where

$$\gamma(\boldsymbol{x}) = \begin{cases} 1 & , d(\boldsymbol{x}) \geq tR \\ \dfrac{1-\beta}{tR} d(\boldsymbol{x}) + \beta & , d(\boldsymbol{x}) < tR \end{cases} \tag{4.2}$$

Here, β and t are the parameters of the distance-based approach. For a material point $\boldsymbol{x}$ lying on the boundary, the distance $d(\boldsymbol{x}) = 0$ and (4.2) yields $\gamma(\boldsymbol{x}) = \beta$. On the other hand, when $d(\boldsymbol{x})$ is greater than tR then $\gamma(\boldsymbol{x}) = 1$ and the standard scaling approach is recovered. In the boundary layer of thickness tR, the value of γ increases linearly from β to 1. For $\beta = 0$ the material behavior on the boundary is fully local.

The stress-based approach, shown in Figure 4.3, is motivated by the interaction of micro-cracks formulated by Bažant (1994) and was applied in a simplified form by Jirásek and Bažant (1994). A transformation matrix $\boldsymbol{T}$ is calculated that depends on the effective stress state $\bar{\boldsymbol{\sigma}}$ at $\boldsymbol{x}$:

$$\boldsymbol{T} = \begin{pmatrix} 1 & 0 \\ 0 & 1/\gamma \end{pmatrix} \begin{pmatrix} n_{1x} & n_{1y} \\ -n_{1y} & n_{1x} \end{pmatrix} = \begin{pmatrix} n_{1x} & n_{1y} \\ -n_{1y}/\gamma & n_{1x}/\gamma \end{pmatrix} \tag{4.3}$$

where n_{1x} and n_{1y} are the components of the unit eigenvector $\boldsymbol{n}_1$ associated with the maximum tensile principal eigenvalue $\bar{\sigma}_1$ of the effective stress tensor $\bar{\boldsymbol{\sigma}}$. Multiplication by $\boldsymbol{T}$ transforms an ellipse with principal axes aligned with the principal directions of $\bar{\boldsymbol{\sigma}}$ and major and minor semi-axes lengths 1 and γ into the unit circle. Hence, the weights of the contributions of source points $\boldsymbol{\xi}$ lying along the minor axis of the ellipse are decreased.

The new weight function

$$\alpha_0(\boldsymbol{x}, \boldsymbol{\xi}) = \exp\left(-\frac{\|\boldsymbol{T}(\boldsymbol{x}) \cdot (\boldsymbol{x} - \boldsymbol{\xi})\|}{R}\right) \tag{4.4}$$

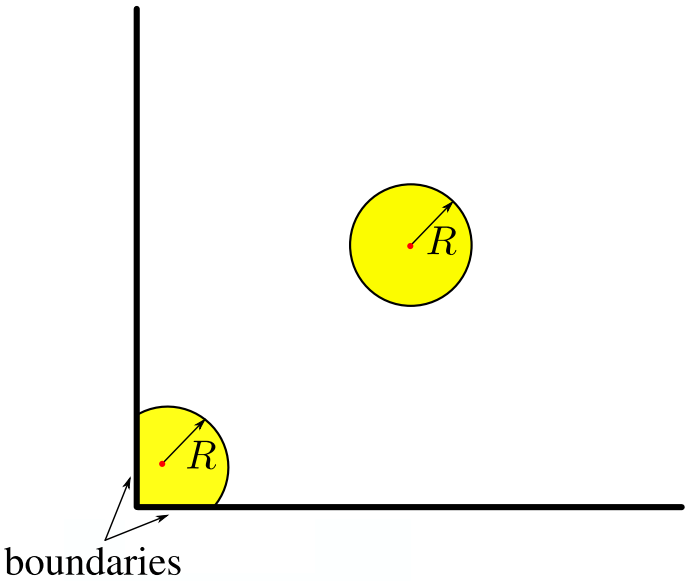

Figure 4.1: Illustration of the standard scaling approach.

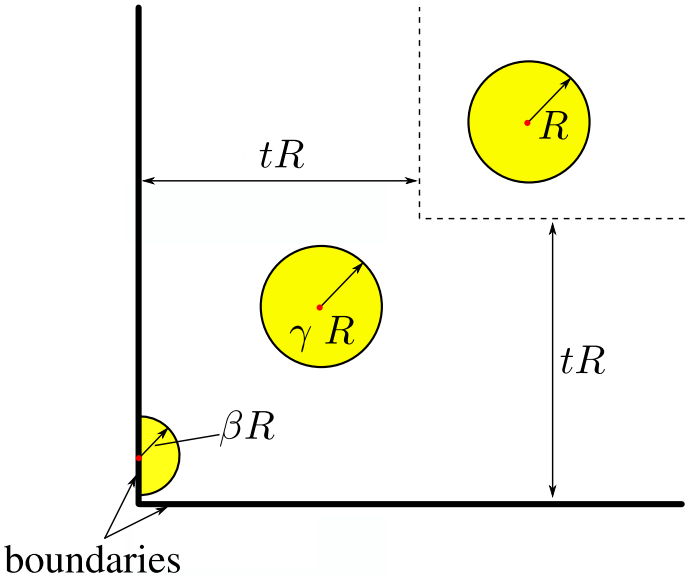

Figure 4.2: Illustration of the distance-based scaling approach.

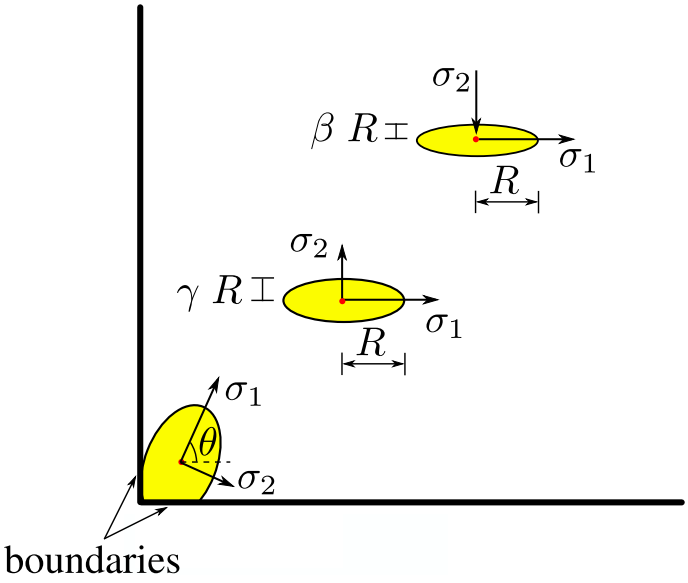

Figure 4.3: Illustration of the stress-based scaling approach.

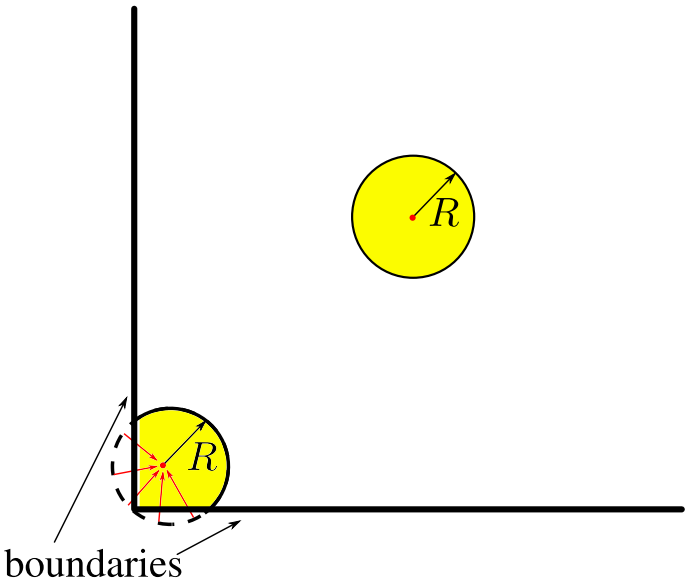

Figure 4.4: Illustration of the local complement scaling approach.

is influenced by the effective stress at point $\boldsymbol{x}$. In (4.3) γ is a scaling factor, defined as

$$\gamma(\boldsymbol{x}) = \begin{cases} \beta + (1-\beta)\left(\dfrac{<\bar{\sigma}_2>_+}{\bar{\sigma}_1}\right) & ,\bar{\sigma}_1 > 0 \\ 1 & ,\bar{\sigma}_1 \leq 0 \end{cases} \tag{4.5}$$

Here, β is a parameter of this approach, $\bar{\sigma}_2$ is the minimum (second in the 2D domain) principal effective stress and $< . >_+$ denotes again the MacAuley brackets (positive part operator). In uniaxial tension the principal effective stresses are $\bar{\sigma}_1 = \bar{\sigma}_\mathrm{t} > 0$ and $\bar{\sigma}_2 = 0$, which gives $\gamma = \beta$. A minimum value of γ is enforced by parameter β to ensure that the integration domain does not degenerate into an infinitely small area. In a finite element analysis, the calculation of the nonlocal parameters is based on the Gauss integration scheme and would be very inaccurate in the case of an infinitely small averaging domain. For equi-biaxial stress states all principal stresses are equal ($\bar{\sigma}_1 = \bar{\sigma}_2$), γ is equal to 1 and the matrix $\boldsymbol{T}$ is equal to the identity matrix such that $\|\boldsymbol{T}(\boldsymbol{x}) \cdot (\boldsymbol{x} - \boldsymbol{\xi})\| = \|(\boldsymbol{x} - \boldsymbol{\xi})\|$. Hence, the standard scaling approach is recovered.

In the stress-based approach, the assigned weights are modified based on the effective stress state of the receiver point $\boldsymbol{x}$. Boundaries are taken into account implicitly based on the resulting effective stress field. On a free boundary of a specimen with no applied surface tractions, the principal stress directions are normal and tangential to the boundary whereas the principal component that is perpendicular to the boundary vanishes. If the principal stress field along the boundary is tensile, the internal length is reduced in the perpendicular direction similarly to the distance-based approach.

All the aforementioned methods break the symmetry of the nonlocal weight function with respect to its arguments $\boldsymbol{x}$ and $\boldsymbol{\xi}$. A modification preserving this symmetry

was proposed by Borino et al. (2003) and will be referred as the local complement method (Figure 4.2). This methodology is based on increasing the weight of the local contribution to compensate for the missing contributions from material points of the nonlocal domain located beyond the physical boundary of the body. Mathematically, this can be described by a weight function

$$\alpha(\boldsymbol{x},\boldsymbol{\xi}) = \alpha_\infty(\boldsymbol{x},\boldsymbol{\xi}) + v(\boldsymbol{x})\delta(\boldsymbol{x}-\boldsymbol{\xi}) \tag{4.6}$$

where $\alpha_\infty(\boldsymbol{x},\boldsymbol{\xi})$ is the normalised weight function described in (3.10) for an infinite medium,

$$v(\boldsymbol{x}) = 1 - \int_V \alpha_\infty(\boldsymbol{x},\boldsymbol{\xi})\mathrm{d}\boldsymbol{\xi} \tag{4.7}$$

where $v(\boldsymbol{x})$ is the relative weight of the missing volume, and δ is the Dirac distribution. The function $\alpha_\infty(\boldsymbol{x},\boldsymbol{\xi})$ depends only on the distance between points $\boldsymbol{x}$ and $\boldsymbol{\xi}$ and is normalised according to the standard scaling approach such that the integral of $\alpha_\infty(\boldsymbol{x},\boldsymbol{\xi})$ in an infinite integration domain is equal to unity. In an infinitely large medium, the standard scaling approach is recovered because $v(\boldsymbol{x}) = 0$.

The physical meaning of (4.6) is that the nonlocal variable, e.g. nonlocal equivalent strain, is computed as the linear combination of the weighted average evaluated with a fixed weight function $\alpha_\infty(\boldsymbol{x},\boldsymbol{\xi})$ and an additional term that contains the local value

$$\bar{\varepsilon}_{\mathrm{eq}}(\boldsymbol{x}) = \int_V \alpha_\infty(\boldsymbol{x},\boldsymbol{\xi})\varepsilon_{\mathrm{eq}}(\boldsymbol{\xi})\mathrm{d}\boldsymbol{\xi} + v(\boldsymbol{x})\varepsilon_{\mathrm{eq}} \tag{4.8}$$

The extra term is called the local complement.

4.2 Calibration

The nonlocal damage and the two damage plasticity constitutive laws were calibrated against meso-scale analyses results. The aim was to determine the basic parameters from the direct tension test, reported in Section 3.3, in which the influence of the boundaries is eliminated. In an infinitely large periodic specimen, all the nonlocal averaging approaches lead to the same results and therefore only the standard scaling approach is used in the calibration of the nonlocal models.

The periodic cell, presented in Section 3.3, with edge size $\alpha = 100$ mm was analysed with the meso-scale approach. The lattice was generated with $d_{\min} = 0.75$ mm. The aggregate volume fraction was chosen as $\rho = 0.3$ with maximum and minimum aggregate

Table 4.1: Material parameters of the meso-scale model

	E [GPa]	γ	f_t [MPa]	q	c	G_f [N/m]
Mortar	30	0.33	5.3	2	10	93
ITZ	45	0.33	1.8	2	10	31
Aggregate	90	0.33	-	-	-	-

diameters ϕ_max =12 mm and ϕ_min =4.75 mm, respectively. The material parameters for each phase of concrete are shown in Table 4.1. The random field was characterised by an autocorrelation length $l_\mathrm{a} = 1$ mm and a coefficient of variation $c_\mathrm{v} = 0.2$. The mean average stress-average strain curve and the dissipated energy density profile parallel to the loading direction were calculated from a set of 100 analyses.

The nonlocal models were calibrated against the meso-scale results by analysing the equivalent problem, specified in Section 3.3. The specimen was analysed by a row of quadrilateral elements with length and width equal to a =100 mm. The resulting load-displacement diagrams were converted into average stress-average strain after dividing by the initial cross-sectional area and by the initial specimen length, respectively. The nonlocal isotropic damage model A and the two damage-plasticity approaches were calibrated against the meso-scale analyses results by getting the best fit of the average stress-average strain curve and of the mean dissipated energy density profile. In all cases standard scaling was applied and the value of the interaction radius R of the nonlocal model is specified by fitting the width of the dissipated energy density profiles with the meso-scale approach results. The elastic parameters provided by the calibration procedure are $E = 29.6$ GPa and $\nu = 0.2$ for all macroscopic constitutive laws. The remaining parameters of the damage model are: $f_\mathrm{t} = 2.86$ MPa, $\varepsilon_\mathrm{max} = 0.000198$, $\varepsilon_1 = 0.00024$, $\varepsilon_2 = 0.00052$, $n = 0.85$ and $R = 4$ mm. The parameters of the plastic part of the damage-plasticity models control the pre-peak part of the load-displacement curve and their optimised values are: $f_\mathrm{t} = 2.86$ MPa, $\varepsilon_\mathrm{p,max} = 0.0001234$, $E_0 = 1480$ GPa. Optimised parameters of the damage part of the damage-plasticity model, which control softening, were specified as $d_1 = 0.08$, $d_2 = 1.3$, $d_3 = 0.04$, $d_4 = 1$ and $d_5 = 0.65$ and $R = 5$ mm for the nonlocal damage-plasticity model ($m = 1$), and $d_1 = 0.08$, $d_2 = 1.3$, $d_3 = 0.08$, $d_4 = 0.9$ and $d_5 = 0.6$ and $R = 2.4$ mm for the over-nonlocal damage plasticity model ($m = 2$).

The results of the calibration are shown in Figure 4.5 in the form of average stress-average strain curves and dissipated energy density profiles across the fracture process zone. The stress-strain curves of the nonlocal models agree very well with the meso-scale results. The dissipation profile of the nonlocal damage model fits the curve obtained from meso-scale analyses. The over-nonlocal damage-plasticity model ($m = 2$) results in a profile, which has a different shape to the meso-scale one and its width was

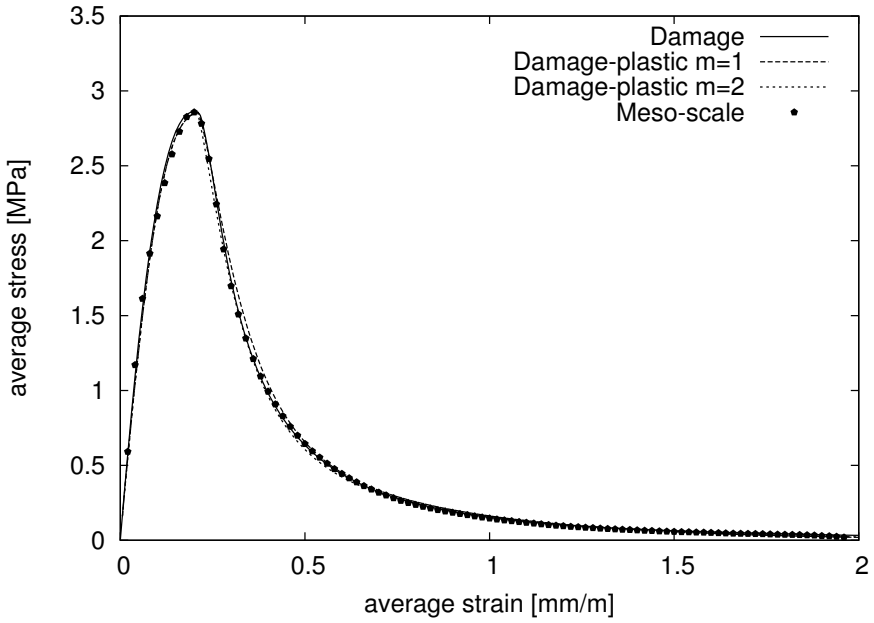

Figure 4.5: Average stress-average strain curves of the direct tension specimen.

adjusted to get the best fit in the least-square sense. The nonlocal formulation ($m = 1$) is leading to mesh-independent load-displacement curves, as illustrated by Grassl and Jirásek (2006a). However, the shape of the dissipation profile cannot be captured properly because the plastic strains localise into a single element and the dissipation in the damaged zone outside the fully localised plastic zone is very small. Hence, the total dissipation is enforced to be the same as in the meso-scale analysis.

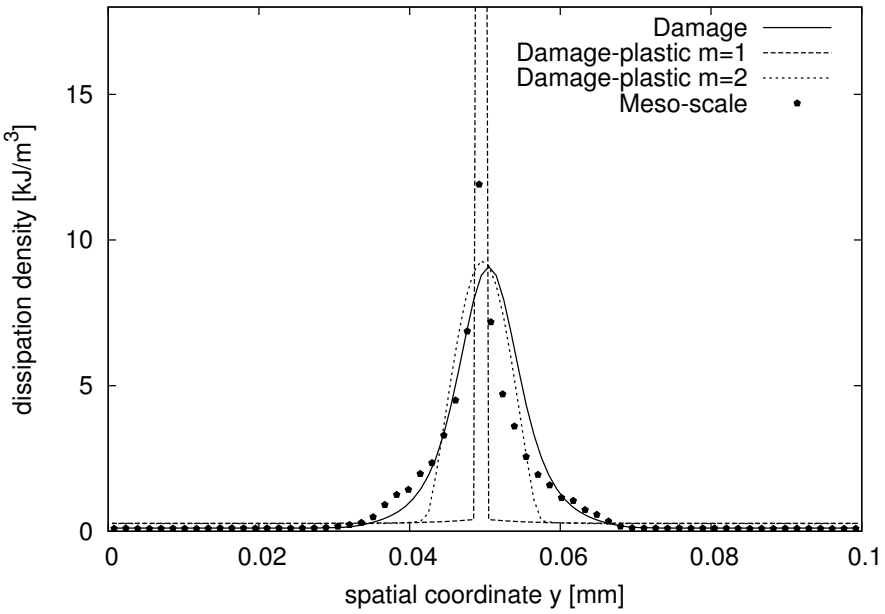

Figure 4.6: Dissipated energy density across the fracture process zone in the last loading step of the direct tension specimen.

4.3 Analyses

The performance of the four nonlocal damage and the two damage-plasticity approaches, described in Sections 4.1 and 3.1.2, is evaluated in modelling specimens with different types of boundaries. The calibrated constitutive laws are applied to model concrete beams subjected to three-point bending in 2D plane-stress conditions. Different types of boundaries are investigated by modelling an unnotched beam ($\alpha = 90°$), a sharp notched beam ($\alpha = 0°$) and a V-notched beam ($\alpha = 45°$), as shown in Figure 4.7. From each analysis the load-displacement curve and the dissipated energy profile along the beam ligament were extracted and compared to the meso-scale results, that are averages of 100 analyses and were reported in Grassl et al. (2012). Hence, the performance of the nonlocal approaches in modelling boundaries is evaluated.

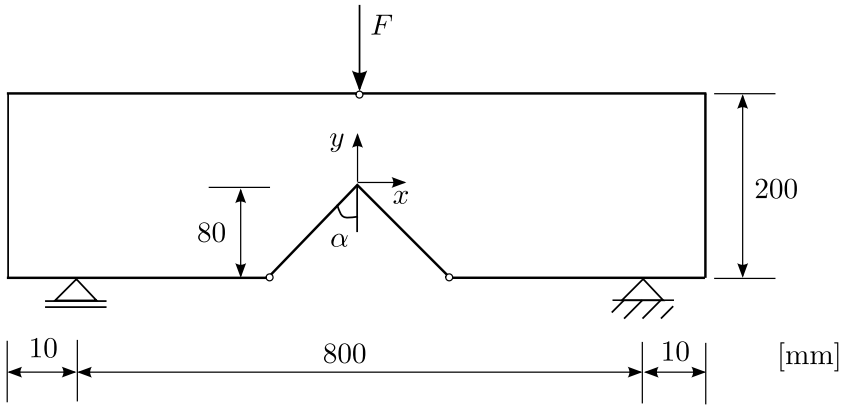

Figure 4.7: Geometry and loading setup of the notched beams subjected to three point bending.

4.3.1 Nonlocal damage models

The results from the analyses with the different nonlocal damage approaches are presented in this section. The additional parameters of the modified averaging schemes were chosen as $\beta = 0.15$, and t = 1.0 for the distance-based approach and as $\beta = 0.15$ for the stress-based approach. The load-displacement curves and the dissipated energy profiles from the beam analyses with the four nonlocal damage approaches are shown in Figures 4.8-4.13. The dissipated energy profiles are presented only for the first 3 cm of the ligament, where the influence of the notch is pronounced, in order to improve the clarity of the figures. In Figures 4.8-4.10, it can be seen that the peak load of the meso-scale approach is overestimated by all nonlocal models for all beam geometries.

Away from the notch, the energy dissipation is almost uniform and is slightly overestimated for all nonlocal averaging methodologies. This effect may be attributed to the multiaxiality of the stress state. In the bending test the second and third principal effective stresses at all material points along the ligament are nonnegligible and close to the notch the stress state is highly biaxial. Therefore, applying a different formulation of the local equivalent strain could resolve this issue as it was illustrated in Jirásek and Bauer (2012).

For the unnotched specimen ($\alpha = 90°$) all models overestimate the peak load but the predicted energy dissipation on the specimen boundary is comparable to the meso-scale analyses results. However, the standard and the stress-based model still overpredict the energy dissipation close to the boundary, which is underestimated by the distance-based and the local complement approach.

In the vicinity of the notch, a much higher dissipation is observed for the beams with $\alpha = 0°$ and $45°$, which is not in accordance with the meso-scale analyses results (Figures 4.8 and 4.9). The distance-based approach results in a reduction of the dissipation within a zone of radius tR away from the boundary but outside this region the dissipation profile is similar to the analyses with the standard scaling approach (Figures 4.11 and 4.12). The stress-based approach leads to a lower dissipation density compared to standard scaling for all beams. For the local complement method, a relationship may be identified between geometry of the notch and the performance of the nonlocal model. In the sharp-notched ($\alpha = 0°$) beam, excessive dissipation is still observed around the notch whereas in the V-notched case there is a good agreement with meso-scale analyses results. It can be concluded, that the larger the missing area, outside the beam, the smaller the dissipated energy close to the notch compared to the standard scaling approach.

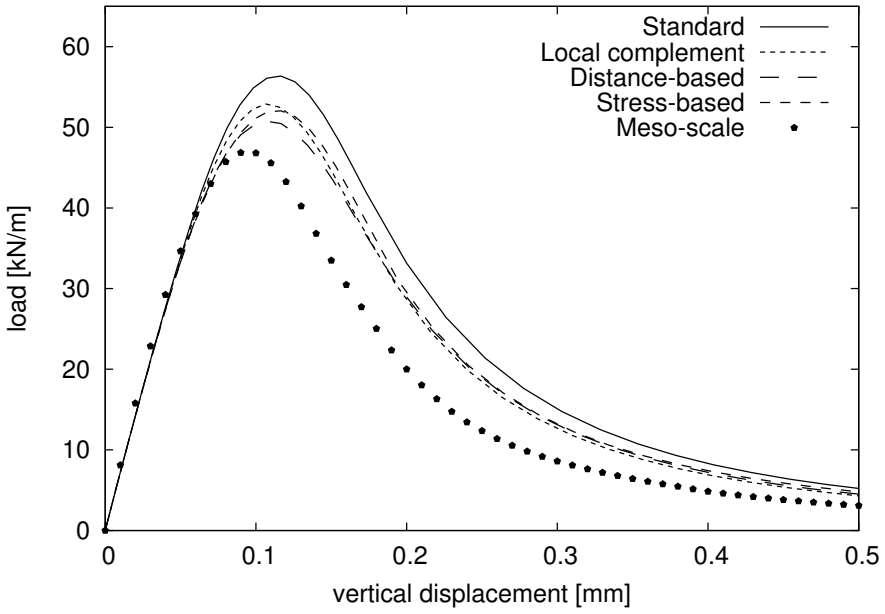

Figure 4.8: Comparison of the load-displacement curves of four nonlocal damage approaches and meso-scale analysis for specimen with a sharp notch ($\alpha = 0°$).

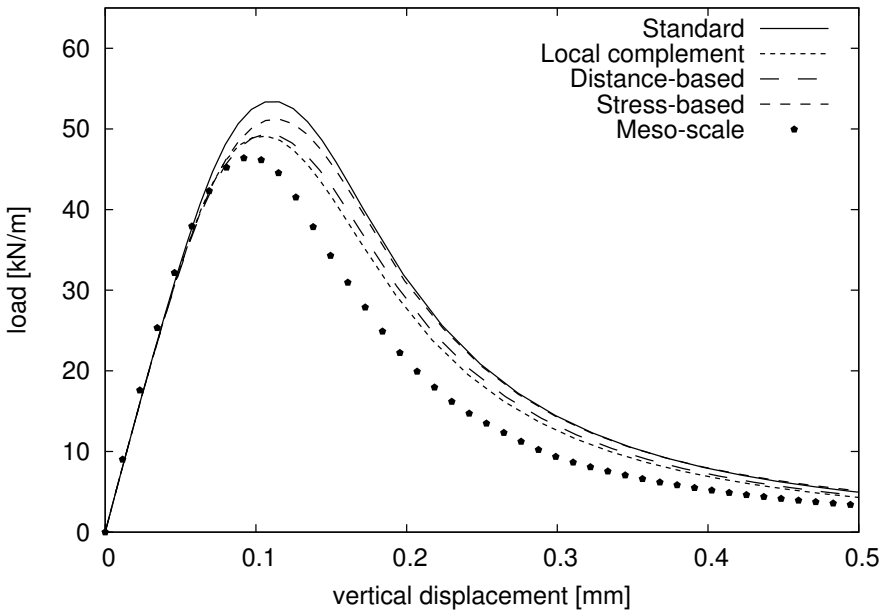

Figure 4.9: Comparison of the load-displacement curves of four nonlocal damage approaches and meso-scale analysis for specimen with a V-notch ($\alpha = 45°$).

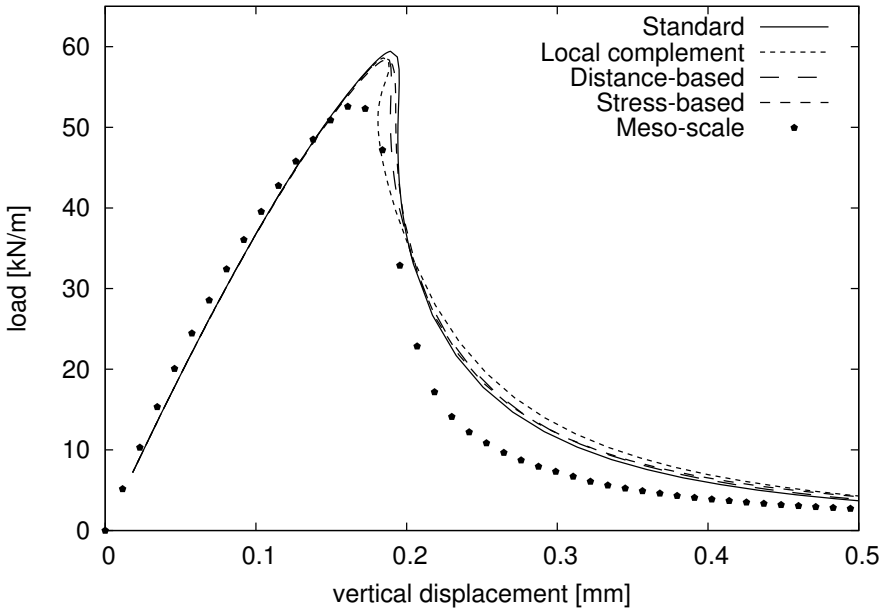

Figure 4.10: Comparison of the load-displacement curves of four nonlocal damage approaches and meso-scale analysis for the unnotched specimen ($\alpha = 90°$).

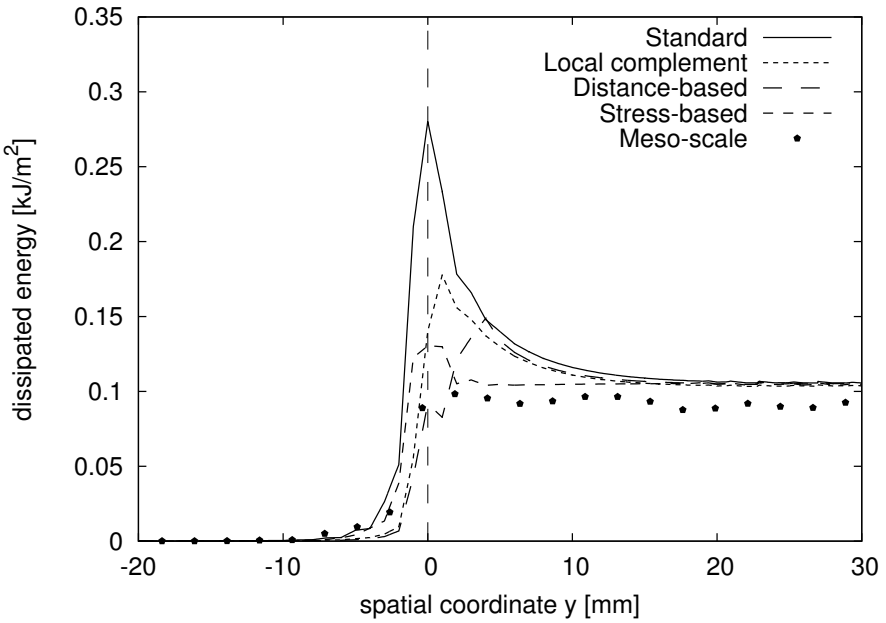

Figure 4.11: Comparison of the dissipated energy profiles of four nonlocal damage approaches and meso-scale analysis for specimen with a sharp notch ($\alpha = 0°$).

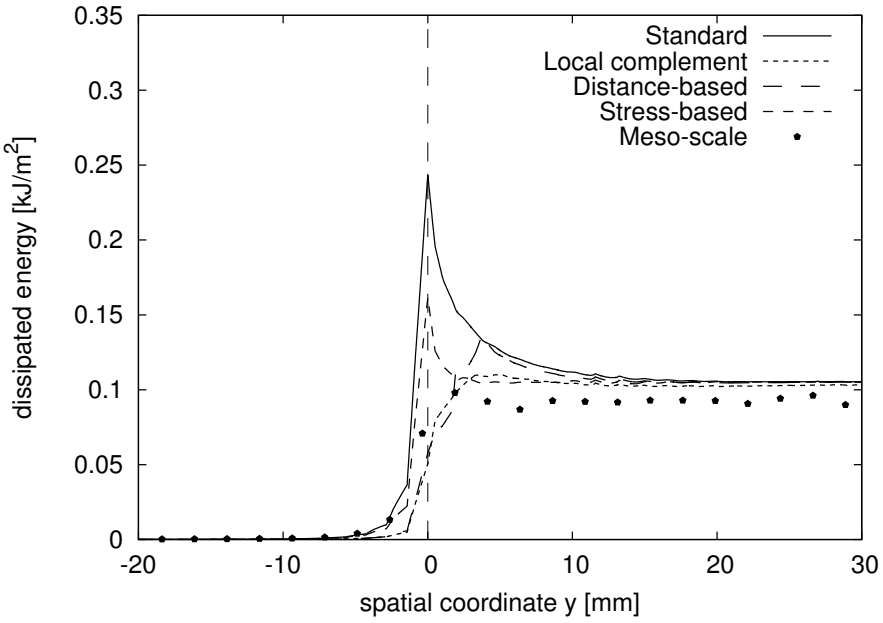

Figure 4.12: Comparison of the dissipated energy profiles of four nonlocal damage approaches and meso-scale analysis for specimen with a V-notch ($\alpha = 45°$).

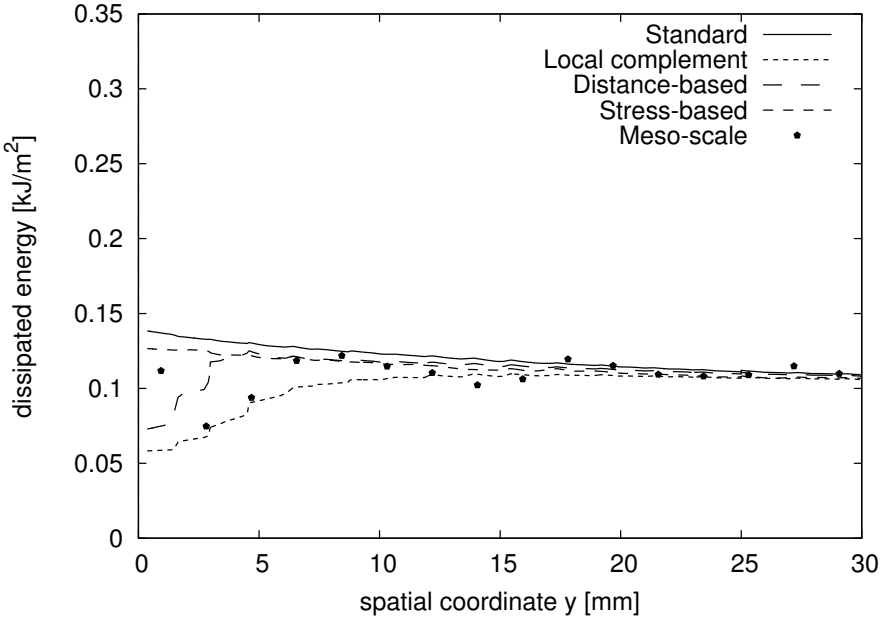

Figure 4.13: Comparison of the dissipated energy profiles of four nonlocal damage approaches and meso-scale analysis for the unnotched specimen ($\alpha = 90°$).

The evolution of the constitutive response provides more insight into the performance of the nonlocal approaches. For each nonlocal approach the point with the highest nonlocal equivalent strain next to the notch tip of the V-notched beam was investigated. In the distance-based approach, this point lay on the left and in all other models on the right of the notch (Figure 4.14(a)). The nonlocal equivalent strain versus the local one is plotted in Figure 4.15. For an infinitely small interaction domain the nonlocal and the local equivalent strains are equal. However, the assumed averaging domain is nonzero and the nonlocal equivalent strain of the material points lying in the centre of the fracture process zone is reduced due to the contributions from points, that are subjected to lower strains. This effect is more pronounced close to the notch, where material points exhibit higher local equivalent strains than their neighbouring points as it is illustrated in the contour plots in Figures 4.14(b)-(d). In addition, the peak stress at these material points is not equal to the tensile strength, set in the present analyses to $f_{\mathrm{t}} = 2.86$ MPa, which could be the case if local equivalent strains were used instead of the nonlocal ones (Figure 4.13). However, nonlocal equivalent strains are always lower than the local ones leading to lower values of the damage parameter and the damage evolution does not follow the increase of the effective stress field. Hence, an artificial strengthening of the material is observed followed by excessive dissipation near the notch, which is stronger for the standard scaling approach (Figure 4.13).

The reader might think that this artificial strengthening effect occurs also in the direct tension model that was used for the calibration of those models. This statement is not true because the evolution of the strain field in this case is different. Before reaching the peak load, the strains are uniformly distributed throughout the specimen, which means that the local and consequently the nonlocal equivalent strain fields are uniform so that the peak stress should always be equal to the chosen tensile strength. Moreover, in the inelastic regime the strains localise but the field is still uniform along the axis perpendicular to the loading direction and only the variation along the loading direction may slightly reduce the calculated nonlocal equivalent strains. On the other hand, the strain field of the analysed beams is always non-uniform and varies in all directions.

Moreover, nonlocal averaging does not remove the singularity of the strain field close to the notch. Before the onset of damage, the solution corresponds to the elastic solution and the stress is calculated based on the local strain state. The type of singularity depends on the type of the notch but the stresses are unbounded at the notch. Hence, the peak stress recorded in Figure 4.13 for the V-notched beam could be arbitrarily large depending on the distance of the examined point from the notch tip.

Parameter β controls the amount of nonlocal interactions in the weight function $\alpha(\boldsymbol{x}, \boldsymbol{\xi})$ for both the distance- and the stress-based approach. Small values of β result in a

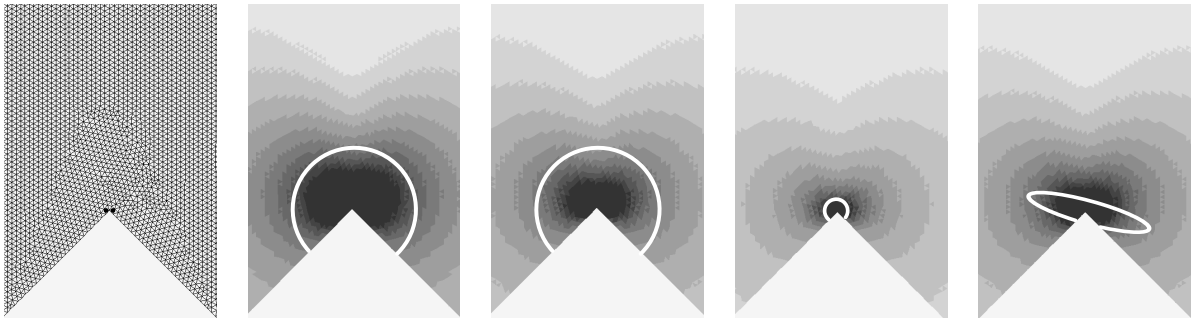

Figure 4.14: (a) Finite element mesh near the V-notch, (b)–(e) contour plots of the local equivalent strain for the four damage models: (b) standard averaging, (c) local complement, (d) distance-based approach and (e) stress-based approach, plotted for the states marked in Figure 4.15. The white shapes indicate the boundaries of the region that contributes to the weighted average of equivalent strain at the integration point near the notch considered in Figure 4.15. The black colour indicates $\varepsilon_{\text{eq}} \geq 0.0001$. Only a part of the beam depth is shown.

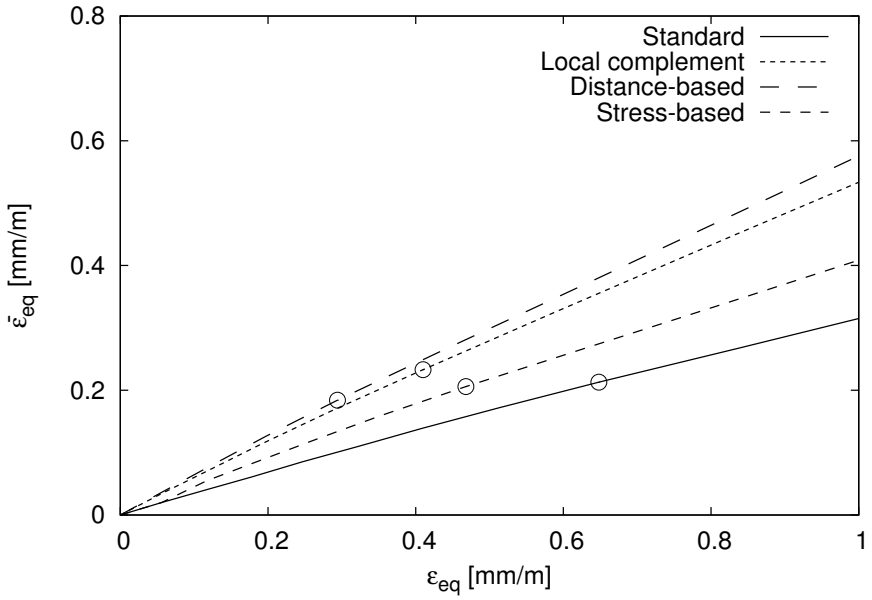

Figure 4.15: Nonlocal versus local equivalent strain of an integration point directly above the V-shaped notch for the four nonlocal damage models.The circles indicate the state for which the contour plot of local equivalent strain in Figure 4.14 is shown.

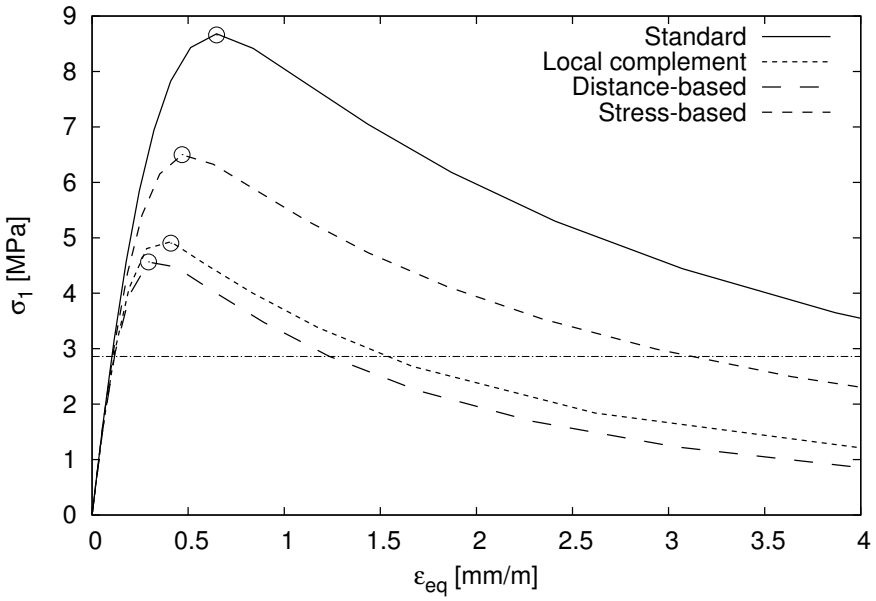

Figure 4.16: Maximum principal stress versus local equivalent strain for an integration point directly above the V-shaped notch for the four nonlocal damage models. The circles indicate the state for which the contour plot of local equivalent strain in Figure 4.14 is shown.

narrower contours of the weight function around receiver point $\boldsymbol{x}$ and for $\beta = 0$ the model becomes local because the nonlocal equivalent strain $\bar{\varepsilon}_{\text{eq}}$ becomes equal to the local one. In order to obtain mesh-independent results, i.e. damage and strains localise in multi-element bands, non-zero values of β should be chosen and the mesh size should be smaller than the width of the final failure zone. The minimum value of $\beta = 0.15$ was enforced for the meshes analysed in the present study so that failure was described accurately without the need to select extremely small mesh sizes.

In Figure 4.17, the influence of parameter β on the final results is investigated for both the distance- and the stress-based approaches. The V-notched specimen is used for the comparisons because it represents an intermediate case between the unnotched and the sharp-notched beam. In both averaging techniques, β controls the dissipation around the notch. The smaller the values of β, the stronger is the reduction of the dissipated energy. Furthermore, in the stress-based approach parameter β influences only the dissipation around the notch leaving the shape of the dissipated energy profile unchanged. It may be concluded that the value of β should be chosen as small as possible for the stress-based approach, same as in Giry et al. (2011). The distance-based approach results in a reduction of the peak value of the dissipated energy, but its effect is limited within distance $tR = 4$ mm from the boundary.

The influence of the values of t is investigated and the distribution of dissipated energy along the ligament of the V-notched specimen is plotted for $t = 1$, 2 and 4 with

fixed $\beta = 0.35$ and $R = 4$ mm in Figure 4.19. As expected, the reduction of the dissipation around the notch is stronger for higher values of t and is always limited within a distance tR from the specimen boundaries. Furthermore, large values of t may result in an underestimation of the dissipated energy which may be prevented by selecting larger values of β. However, as illustrated by the dashed and dotted curves in Figure 4.19 (b), values of $\beta > 0.35$ typically lead to the formation of a local dissipation peak at the notch tip, even for values of t larger than 1. Certain combinations of parameters β and t lead to a successful prediction of the dissipation near the notch but the profile is still irregular. A further improvement is achieved by using a smooth dependence of the reduction factor γ on the distance from the boundary, instead of the piecewise linear dependence according to formula (4.2). The exponential formula

$$\gamma(\boldsymbol{x}) = 1 - (1 - \beta) \exp\left(-\frac{d(\boldsymbol{x})}{tR}\right) \tag{4.9}$$

still uses just two parameters, same as the piecewise linear formula (4.2), but it can eliminate the local peak and provide a very good overall shape of the dissipation density distribution, as illustrated in Figure 4.19 (b) for $\beta = 0.3$ and $t = 1$. In the exponential formula (4.9), the effect of the boundary on the reduction of the nonlocal interaction distance does not vanish for $d(\boldsymbol{x}) \geq tR$, and so the value $t = 1$, which was too small for the piecewise linear formula (4.2), turns out to be appropriate.

Parameter β, that controls the minimum interaction radius, is the most critical one of both nonlocal approaches. Low values of β correspond to assigning lower weights to points that lie further away from boundaries and have lower local equivalent strains upon damage initiation compared to the points lying on the boundary. The nonlocal equivalent strain for the reduced interaction radius is then higher and follows the increase of the local equivalent strain leading to lower local dissipation. Compared to the standard approach, the stress-based approach includes one parameter less than in the distance based approach and is easier to calibrate. However, the additional parameter t in the distance-based approach is physically motivated from experimental results, where it was demonstrated that the FPZ decreases as the crack front propagates away from the boundary.

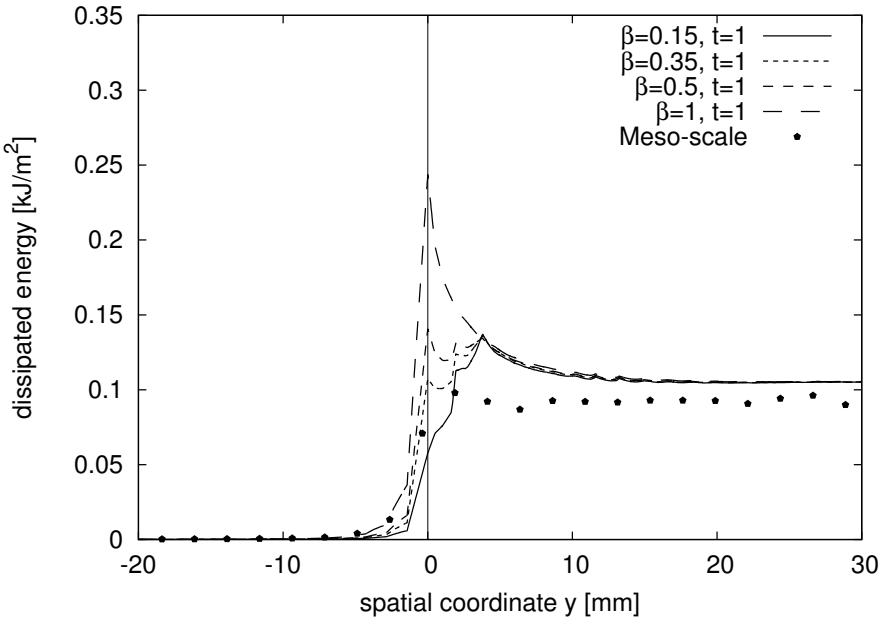

Figure 4.17: Effect of parameter β on the dissipated energy profiles along the ligament length for the V-notched specimen ($\alpha = 45°$) and the distance-based approach.

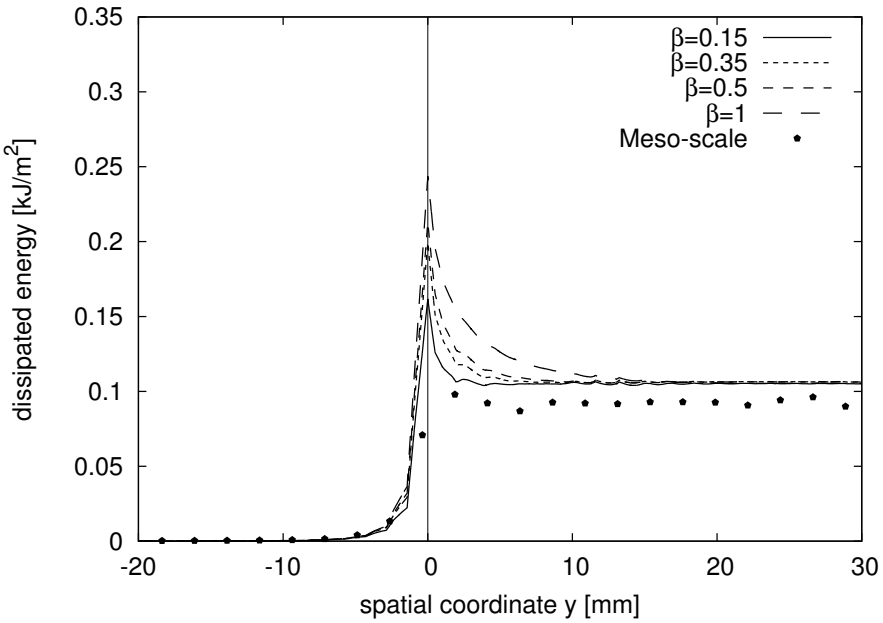

Figure 4.18: Effect of parameter β on the dissipated energy profiles along the ligament length for the V-notched specimen ($\alpha = 45°$) and the stress-based damage approach.

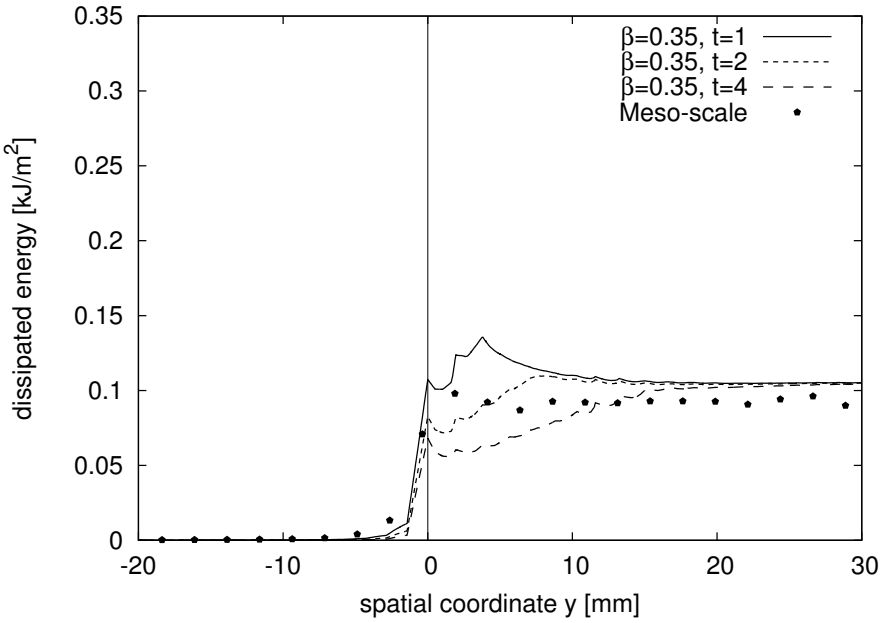

Figure 4.19: Variation of parameter t at fixed $\beta = 0.35$ of the distance-based approach on the dissipated energy profiles along the ligament length for the V-notched specimen ($\alpha = 45°$).

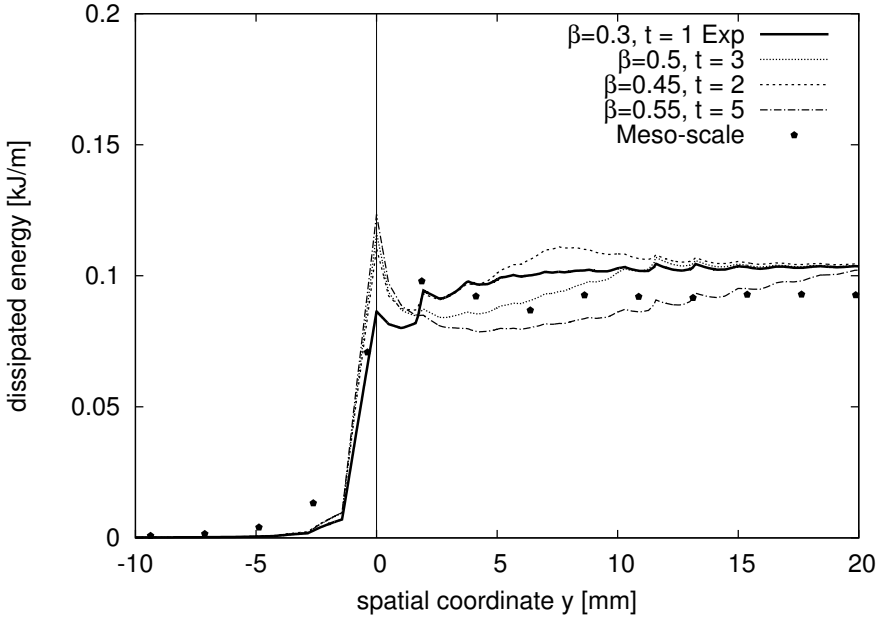

Figure 4.20: Variation of parameters t and β of the distance-based approach on the dissipated energy profiles along the ligament length for the V-notched specimen ($\alpha = 45°$).

4.3.2 Nonlocal damage-plastic models

Nonlocal approaches based on a combination of isotropic damage mechanics and perfect plasticity were also investigated in this study. In these models, the effective stress is limited due to the perfect plasticity and cannot increase beyond the value specified by the yield surface. At a point lying on the boundary, the increase of the damage parameter and nonlocal equivalent strain might not follow the increase of the local equivalent strain due to the contributions of points with low equivalent strains but the effective stress cannot exceed the yield value. Hence, lower local dissipation is expected compared to the one provided by the standard nonlocal damage approach.

The nonlocal damage-plasticity models are limited to analyse the three point bending beam geometries and are compared to meso-scale results in Figures 4.21-4.26. In these models the maximum principal stress cannot exceed the tensile strength, which should lead to lower dissipation around the notch than in the nonlocal damage approaches. However, the overnonlocal formulation with $m = 2$ exhibits a high peak in dissipation at the notch which is comparable to the nonlocal damage model with standard averaging. Furthermore, in the nonlocal damage-plasticity model with $m = 1$ there is excessive dissipation near the notch that is slightly higher than the dissipation along the ligament of the beam.

In damage-plasticity models the effective stress is calculated based on a hardening law which in the present case allows only for limited hardening in the pre-peak (Figure 4.5). The tensile strength cannot exceed the specified tensile strength as it is demonstrated for one element just above the notch in Figure 4.27 by plotting the maximum tensile principal stress versus maximum tensile principal strain. The excess in dissipation may not be attributed to the development of very large stresses but only to the slower evolution of the damage variable compared to the local cummulative plastic strains, which is induced by the nonlocality. Finally, the over-nonlocal damage-plasticity model ($m = 2$) ensures that a distributed and mesh-independent plastic strain profile is obtained (Figure 4.28(b)). This is not the case for the nonlocal damage-plasticity model, as shown in Figure 4.28(a), for which a better fit with the meso-scale results is obtained Figures 4.22.

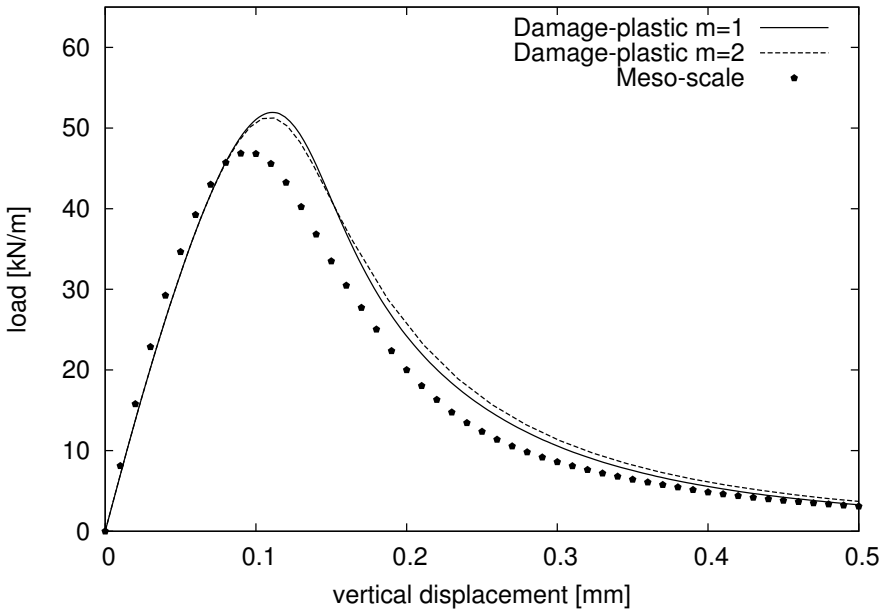

Figure 4.21: Comparison of the load-displacement curves of the nonlocal ($m = 1$) and the over-nonlocal ($m = 2$) damage-plastic approaches and meso-scale analysis for the sharp-notched specimen ($\alpha = 0°$).

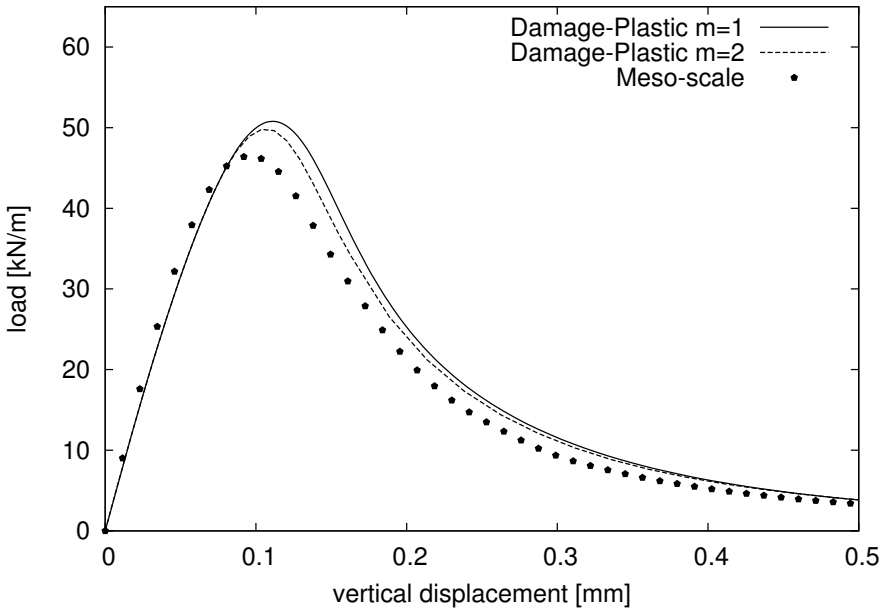

Figure 4.22: Comparison of the load-displacement curves of the nonlocal ($m = 1$) and the over-nonlocal ($m = 2$) damage-plastic approaches and meso-scale analysis for the V-notched specimen ($\alpha = 45°$).

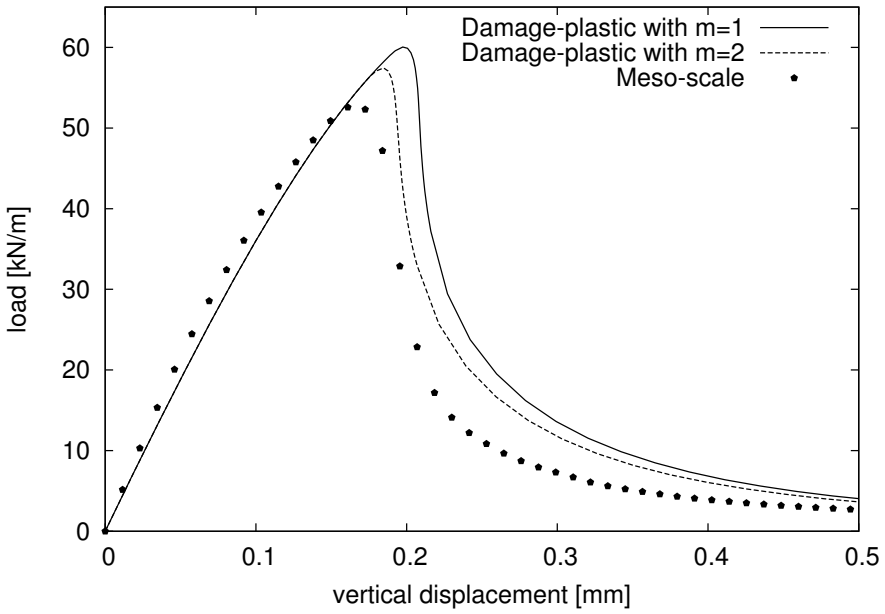

Figure 4.23: Comparison of the load-displacement curves of the nonlocal ($m = 1$) and the over-nonlocal ($m = 2$) damage-plastic approaches and meso-scale analysis for the unnotched specimen ($\alpha = 90°$).

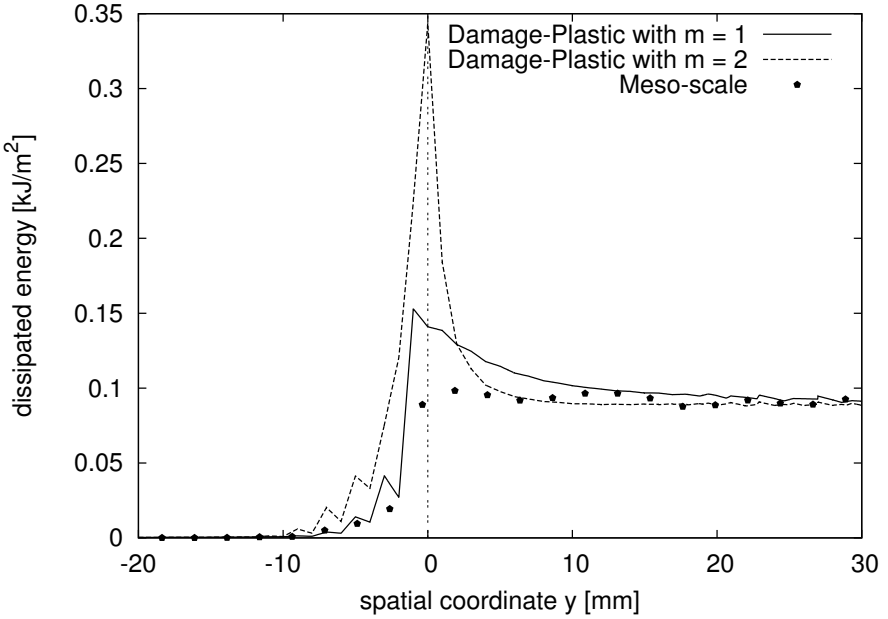

Figure 4.24: Comparison of the dissipated energy profiles of the nonlocal ($m = 1$) and the over-nonlocal ($m = 2$) damage-plastic approaches and meso-scale analysis for the sharp-notched specimen ($\alpha = 0°$).

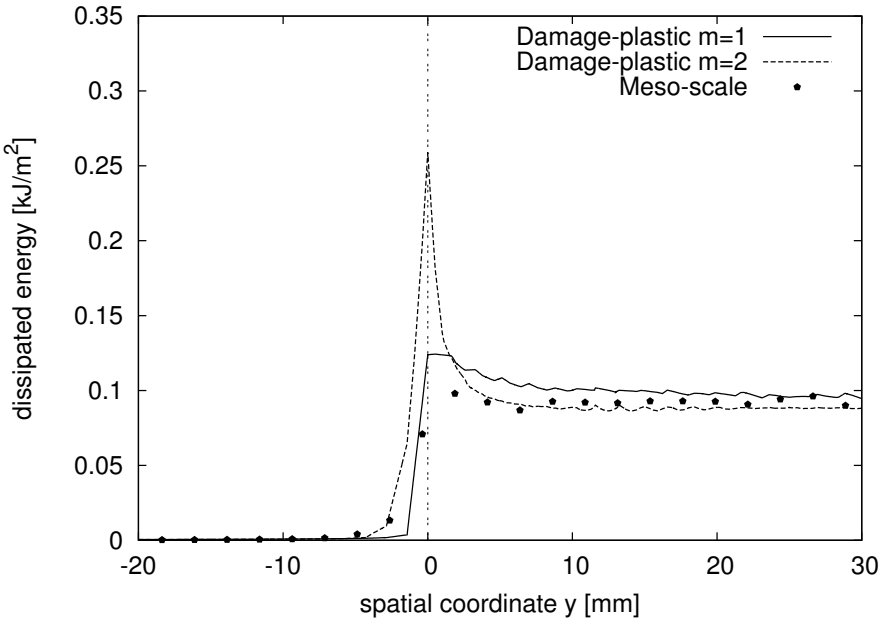

Figure 4.25: Comparison of the dissipated energy profiles of the nonlocal ($m = 1$) and the over-nonlocal ($m = 2$) damage-plastic approaches and meso-scale analysis for the V-notched specimen ($\alpha = 45°$).

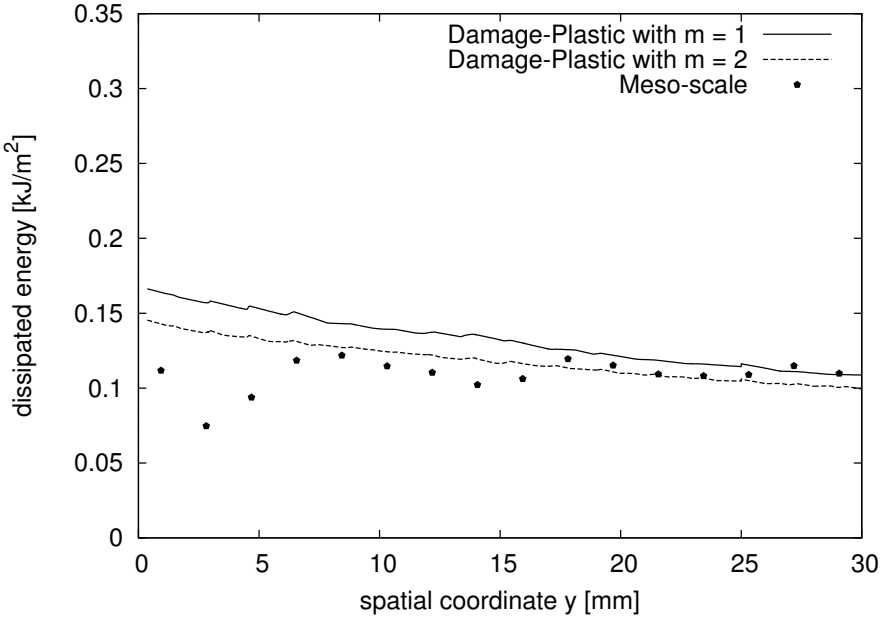

Figure 4.26: Comparison of the dissipated energy profiles of the nonlocal ($m = 1$) and the over-nonlocal ($m = 2$) damage-plastic approaches and meso-scale analysis for the unnotched specimen ($\alpha = 90°$).

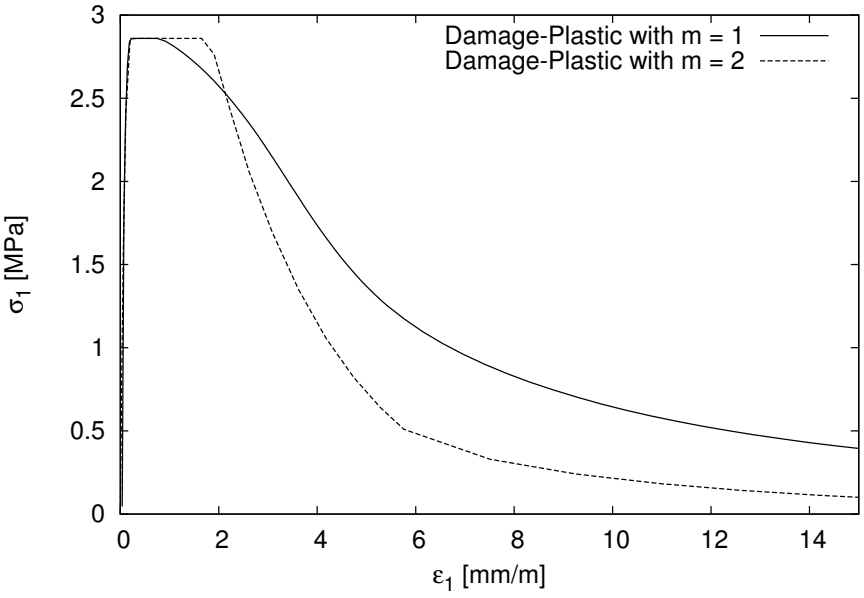

Figure 4.27: Results for the damage-plastic model for the V-notched specimen ($\alpha = 45°$) in the form of maximum principal stress versus strain for an element just above the notch.

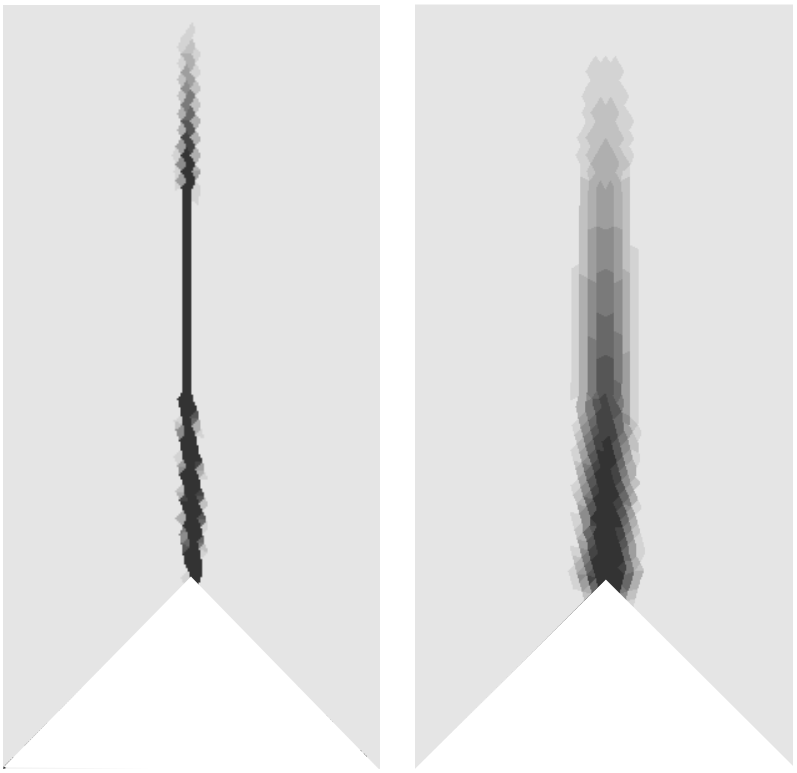

(a) (b)

Figure 4.28: Contour plots of the local plastic hardening parameter for (a) $m = 1$ and (b) $m = 2$ at a displacement of 1.88 mm in Figure 4.22. Black colour indicates $\varepsilon_1 > 0.1$. Only a part of the depth of the beam is shown.

4.4 Discussion

The modelling of boundaries with nonlocal models is addressed in this chapter. An isotropic damage model was combined with four different averaging procedures and a damage-plasticity model was formulated according to the nonlocal and the overnonlocal approach. The constitutive laws were applied to model fracture in beams subjected to three-point bending with three different notch geometries and their results were compared with meso-scale analyses results.

The nonlocal damage model formulated according to the standard scaling approach overestimates the dissipation around the notch which leads to an overprediction of the peak load of the beam. This effect is attributed to the slow evolution of the nonlocal equivalent strain compared to the local one. The modified averaging approaches reduce this excess in energy dissipation close to the notch and result in a better agreement with the meso-scale analyses results. The reduction of the spurious energy dissipation close the notch depends in the local complement method on the type of notch. The distance-based approach requires two additional input parameters, compared to the standard scaling approach, whereas the stress-based approach requires only one and the local complement method does not include any extra parameters.

The damage-plasticity approaches, considered in this study do not require any additional parameters and are still leading to an overestimation of the dissipated energy close to the notch. This effect is more pronounced in the case of the overnonlocal formulation whereas it is limited for the standard averaging methodology for which a better agreement with the meso-scale results is achieved. However, in the nonlocal damage-plasticity model ($m = 1$) the width of the fracture process zone depends on the mesh size.

Chapter 5

A strategy to calibrate nonlocal models for modelling quasi-brittle fracture

The present chapter focuses on the calibration of nonlocal models, which is the second topic addressed in the present thesis. A novel strategy to calibrate nonlocal models is proposed based on the experimental final crack patterns. The calibration procedure is simple and relies in scanning and statistically processing the final fracture surface. The tolerances of the scanning setup are considerably lower than the ones of the AE techniques used for the determination of the FPZ. The interaction radius of the nonlocal model is calibrated by matching the experimental and numerical standard deviations of the crack patterns and the dissipated energy density profile of the 1D bar subjected to direction tension, presented in Section 4.2. The selection of the variables used in the calibration is physically motivated and does not rely solely on the convergence behaviour of the calibration procedure, which is the case in inverse analysis techniques. The main assumption is that the majority of the fracture energy is dissipated in a localised rough crack and is validated from the meso-scale analyses results of a periodic specimen. An application of calibration strategy is presented and the parameters of the nonlocal isotropic damage model B, presented in Section 3.1.1, are determined based on experimental crack patterns of a beam subjected to three-point bending.

5.1 Calibration strategy

The objective of the calibration procedure is to provide the value of the interaction radius R, that enters the weight function $\alpha_0(\boldsymbol{x}, \boldsymbol{\xi})$ in nonlocal models and determines the width of the final FPZ (see (3.10)). The calibration procedure, illustrated in

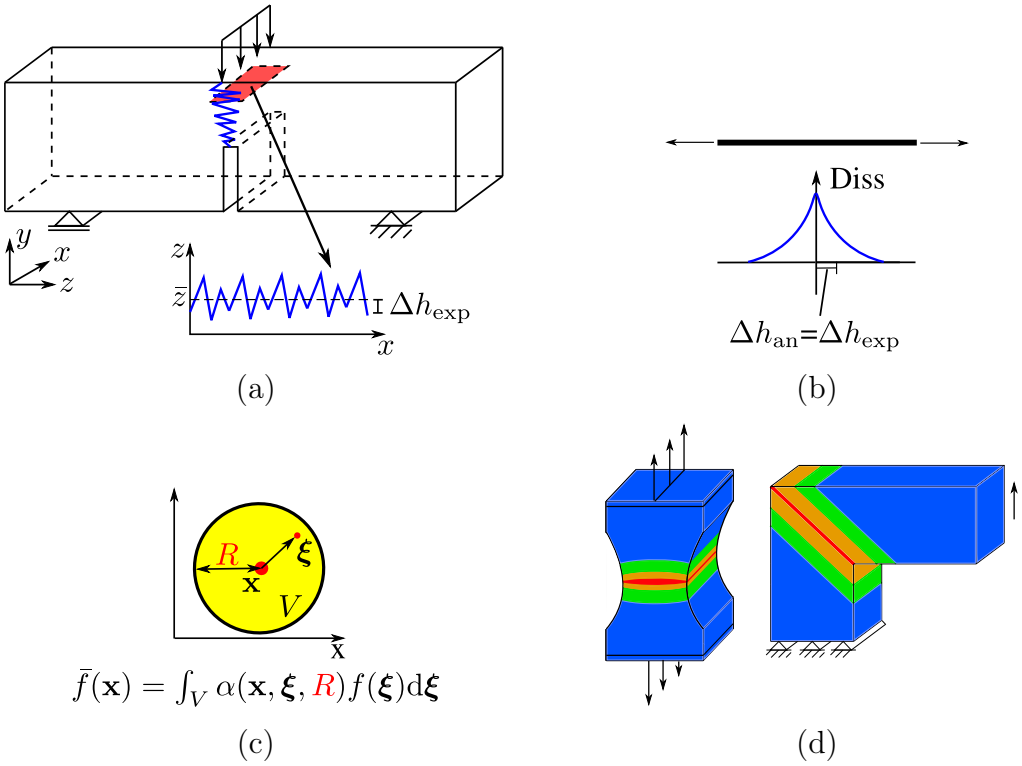

Figure 5.1: Schematic overview of the calibration strategy: (a) Experimental input, (b) Calibration, (c) Nonlocal constitutive model and (d) Structural analysis.

Figure 5.1, may be summarised in the following steps:

1. Perform a fracture test and calculate the fracture energy and the roughness distribution, which is the distribution of the heights of the material points lying on the fracture surface from the mean crack plane (Figure 5.1(a)). Evaluate the experimental standard deviation of the roughness distribution Δh_{exp} from the mean crack plane.

2. Determine the dissipated energy density profile of a 1D bar subjected to tension, analysed with the nonlocal model, based on either a numerical analysis or a closed-form solution (Figure 5.1(b)). Evaluate the analytical standard deviation Δh_{an} of this dissipated energy density profile (Figure 5.1(b)). Here, the standard deviation is computed as the spatial deviation from the material point of maximum dissipation energy density of the profile. This standard deviation has, similarly to the one calculated in the previous step, the unit of length.

3. Calibrate the nonlocal interaction radius R and the other constitutive model parameters such that the standard deviation of the dissipated energy density profile in step 2 is equal to the standard deviation of the roughness distribution measured in step 1, and the numerically obtained dissipated energy per nominal fracture surface is equal to the experimental one (Figure 5.1(c)).

The calibrated nonlocal interaction radius R can then be used in nonlinear analyses of structures in which tensile failure dominates (Figure 5.1(d)).

The experimental standard deviation of the roughness distribution Δh_{exp} is an important input in the described calibration process. Suitable fracture tests need to be performed, such as three-point bending or compact tension test and scanning setups, like optical profilometers, need to be applied to scan the final fracture surface. This results in points located on a regular grid, whose heights are measured from a reference plane. Boundary effects are excluded by discarding areas close to the notch or to the surface of the compressive zone of the specimens. The measurements of the points, lying within the accepted zone of the fracture surface, are then corrected by a multiple linear regression analysis to remove errors due to an overall tilt of the fracture surface, that is introduced during sample preparation. The corrected fracture surface is processed by calculating the height z_i as an average of the heights of the four corner points that define each crack facet i (see Fig. 5.2). Initially the mean of all height heights z_i is calculated as

$$\bar{z} = \sum_{i=1}^{N} w_i z_i \tag{5.1}$$

Here, w_i are the weights of the individual fracture facets, which for the evaluation of the Δh_{exp} are evaluated as

$$w_i = \frac{A_i}{\sum_{k=1}^{N} A_k} \tag{5.2}$$

where A_{i} is the area of each facet. It is assumed that all fracture facets dissipate the same energy, since information about individual dissipation for each fracture facet is normally not available from optical profiling. Then, the standard deviation is defined as

$$\Delta h = \sqrt{\sum_{i=1}^{N} w_i (z_i - \bar{z})^2} \tag{5.3}$$

The local dissipation density is available in the meso-scale analyses in Section 5.2 and it is included in the evaluation of the standard standard deviation by modifying (5.2) to

$$w_i = \frac{A_i d_i}{\sum_{k=1}^{N} A_k d_k} \tag{5.4}$$

where d_i is the dissipation per unit area of the fracture facet i.

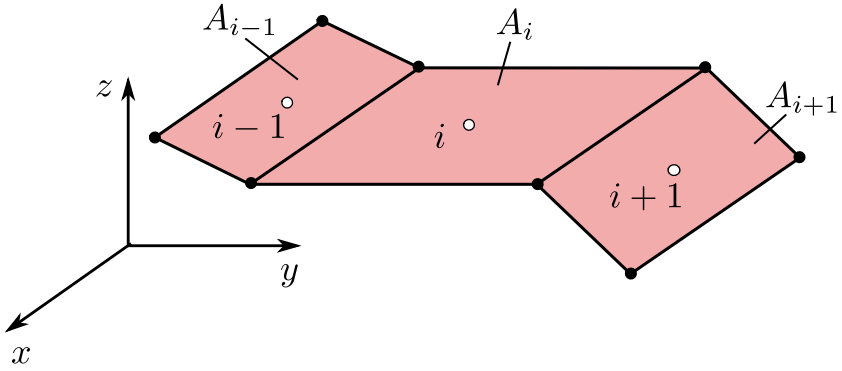

Figure 5.2: Description of the values retrieved from each crack facet for the statistical evaluation of the final crack pattern and of the assumed dissipated energy density distributions.

5.2 Meso-scale validation of the main assumptions

The calibration procedure, presented in the previous section, is based on the assumptions that the majority of the fracture energy is dissipated in the localised macro-crack and that Δh_{exp} calculated for uniform dissipation energy density in (5.3) along the fracture surface is a good approximation of the nonuniform dissipation case in (5.4), which is typical in heterogeneous materials. In the present section, the validity of these two assumptions and the influence of the size of the heterogeneity on Δh_{exp} were investigated by means of meso-scale analyses of a specimen subjected to direct tension.

The meso-scale modelling approach has already been described in Chapter 3 and was used to analyse a periodic cell subjected to direct tension, presented in Section 3.3. The edge length of the cell was $a = 100$ mm. In these analyses, the heterogeneities were taken into account based on autocorrelated random fields. Four different autocorrelation lengths were investigated $l_{\text{a}} = 0.5, 1, 2, 4$ mm and the coefficient of variation was set equal to $c_{\text{v}} = 0.2$ for all analyses. The other model parameters were chosen so that the overall macroscopic properties resulted in Young's modulus $E = 30$ GPa, Poisson's ratio $\nu = 0.2$, tensile strength $f_{\text{t}} = 4.6$ MPa and fracture energy $G_{\text{F}} = 160$ J/m^2. For each parameter set, the average response was evaluated from 100 analyses.

Initially, the results of an individual meso-scale analysis for $l_{\text{a}} = 1$ mm are discussed. The average stress-strain curve for a single meso-scale analysis is shown in Figure 5.3 and the crack patterns for the three marked loading stages are presented in Figure 5.4. In this figure, the gray lines correspond to the Voronoi cross-sections of damaged lattice elements, whose dissipation does not increase in the current step whereas the red lines correspond to the ones whose dissipation increases. Before reaching peak average stress, dissipated energy is distributed over the entire specimen, whereas just after peak, many

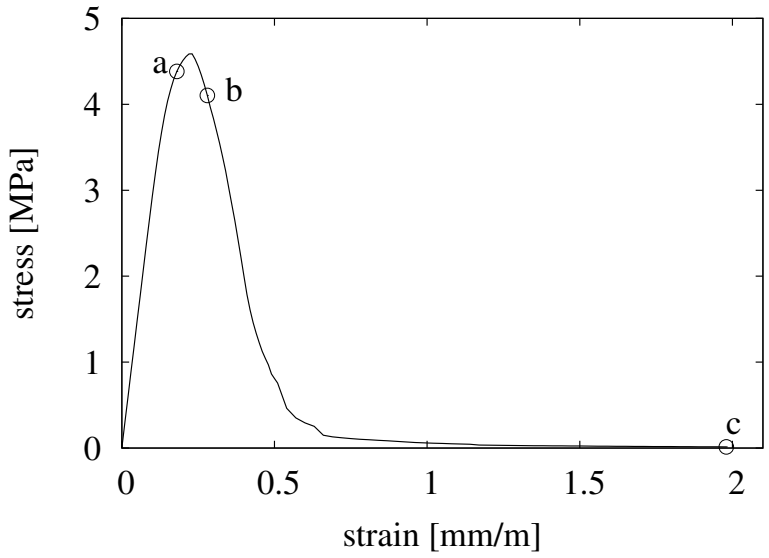

Figure 5.3: (a) Stress-strain curve for a single meso-scale analysis with three stages marked for which the fracture patterns are shown in Figure 5.4.

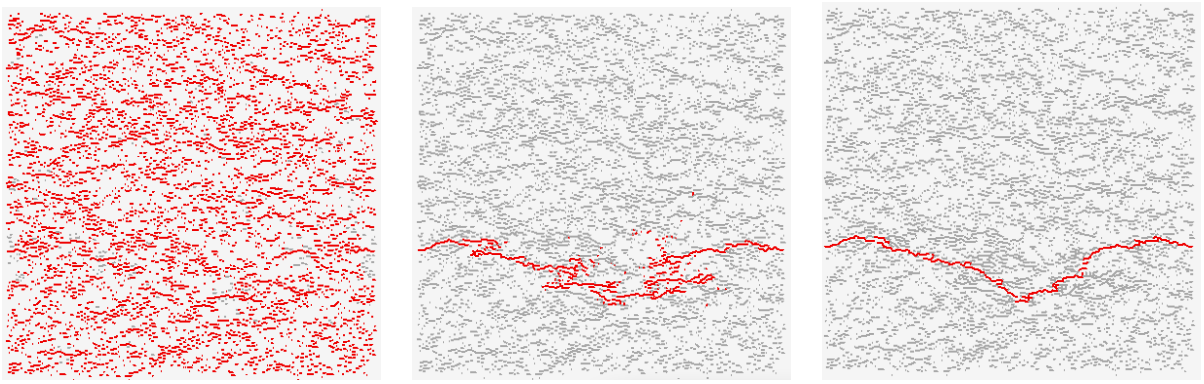

(a) (b) (c)

Figure 5.4: Crack patterns for three stages of loading marked in Fig 5.3(a). Dark gray (red in colour) lines indicate cross-sections of elements which dissipate energy at this stage of analysis. Light gray lines indicate cross-sections of elements which dissipated energy at previous steps but not at the current.

of the elements start to unload and failure is limited to a localised crack, in which fracture energy is dissipated for the remaining part of the analysis. The final crack was assumed to be formed by cross-sections of the elements which dissipate energy during the last step of the analysis (Figure 5.4(c)). In this analysis, the majority of the energy is dissipated in the final localised crack. Furthermore, the average response of the set of meso-scale simulations for $l_a = 1$ mm was investigated to demonstrate that the described failure process was representative of the average failure response of meso-scale analyses. The average stress-strain curve and the average energy density profiles in the direction of loading were constructed as described in Section 3.3. The mean amount of energy dissipated by the localised crack corresponds to approximately 79.5% of the mean total dissipated energy. Furthermore, the average energy increment profiles in the direction of loading are shown in Figure 5.6 for the three steps marked in Figure 5.5. Before peak, the energy is almost uniformly distributed, whereas in the

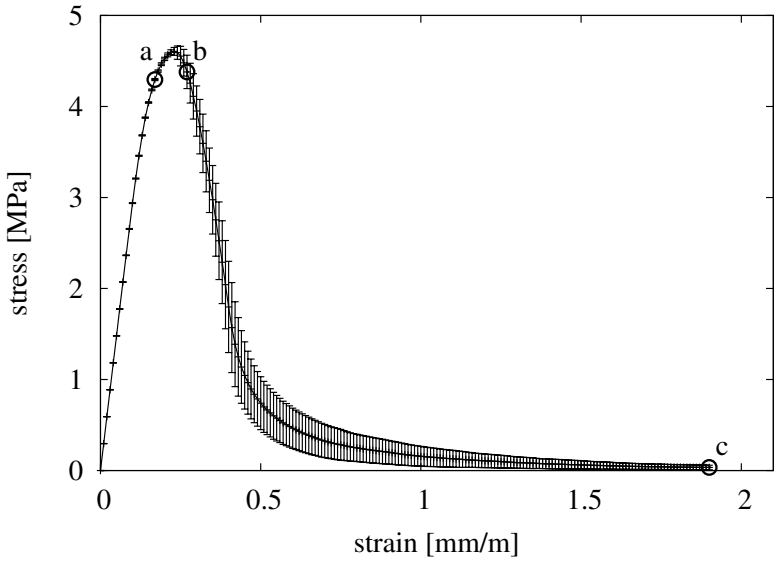

Figure 5.5: (a) Average stress-strain curve for 100 meso-scale analyses.

post-peak regime the energy profile localises with its width remaining almost constant during the fracture process. Thus, the first assumption of the calibration approach is confirmed because the majority of energy is dissipated in the final crack.

The second assumption of the calibration approach is that the standard deviation of the roughness distribution can be determined from the geometry of the final crack by ignoring the dissipation of individual crack segments. The validity of this assumption is assessed by applying two approaches to evaluate the average dissipated energy density profile for the set of analyses corresponding to $l_{\mathrm{a}} = 1$ mm. In the first one, each facet of the final localised crack was assigned a uniform energy dissipation, determined from the total dissipated energy divided by the total fracture surface. According to the second approach, the actual energy dissipation obtained from the meso-sale analyses was used. These two energy profiles are presented in Figure 5.7. The width and shape of the profiles of the two approaches are almost identical. Hence, the second assumption of the calibration approach is validated.

In the present study heterogeneities are modelled by autocorrelated random fields and the heterogeneity size is implicitly determined by the autocorrelation length l_{a}, as described in Section 3.2. The influence of l_{a} on the width of the FPZ is investigated by evaluating the standard deviation Δh, defined in (5.3), for all four autocorrelation lengths. The standard deviations Δh of the individual analyses are averaged and the results are shown in Figure 5.8. For increasing autocorrelation length l_{a}, the value of Δh increases leading to a wider fracture zone. Examples of the final crack patterns from arbitrarily chosen analyses with $l_{\mathrm{a}} = 0.5, 1, 2$ and 4 mm are shown in Figure 5.9. For individual analyses, the correlation between l_{a} and the crack standard deviation is not always obvious. For instance, the value of Δh of the crack patterns for $l_{\mathrm{a}} = 2$ mm

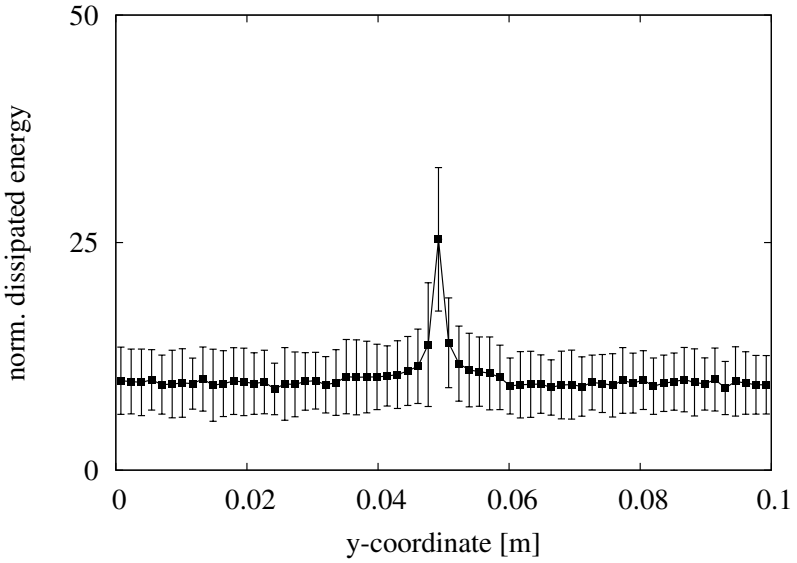

(a) Load step a

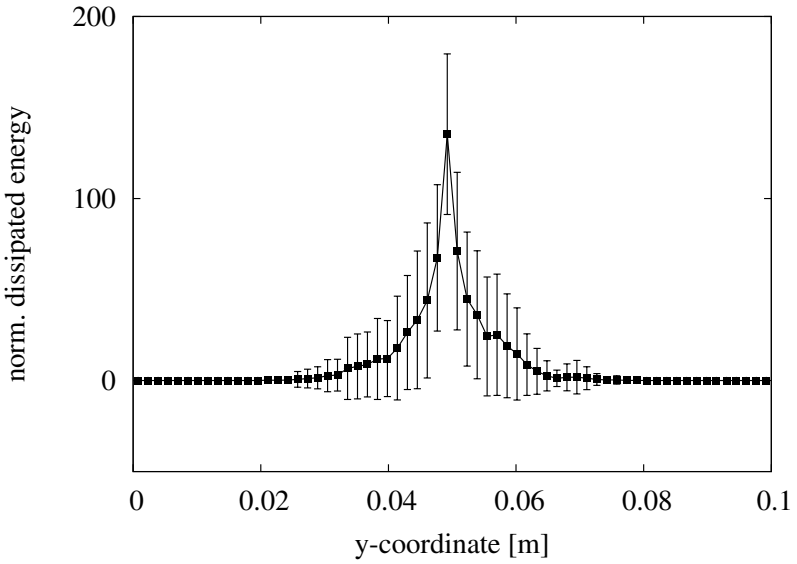

(b) Load step b

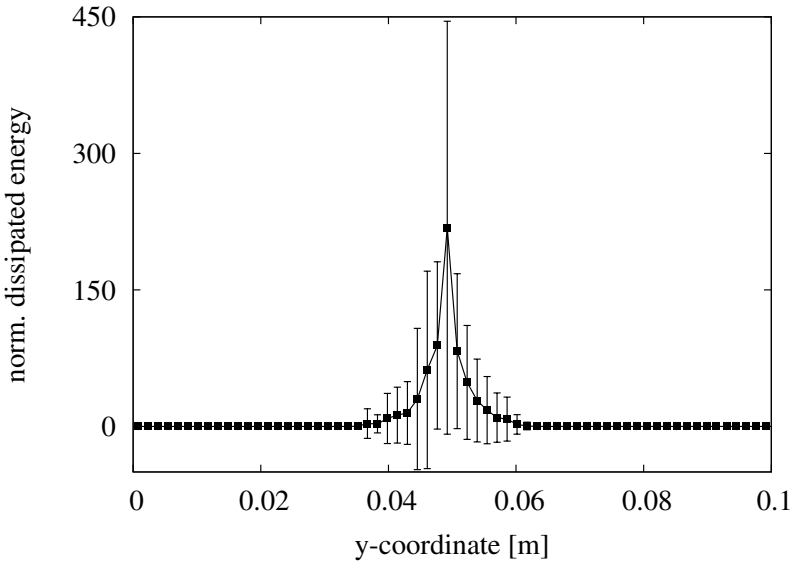

(c) Load step c

Figure 5.6: Profiles of the increment of dissipated energy across the FPZ at the load steps marked in 5.5.

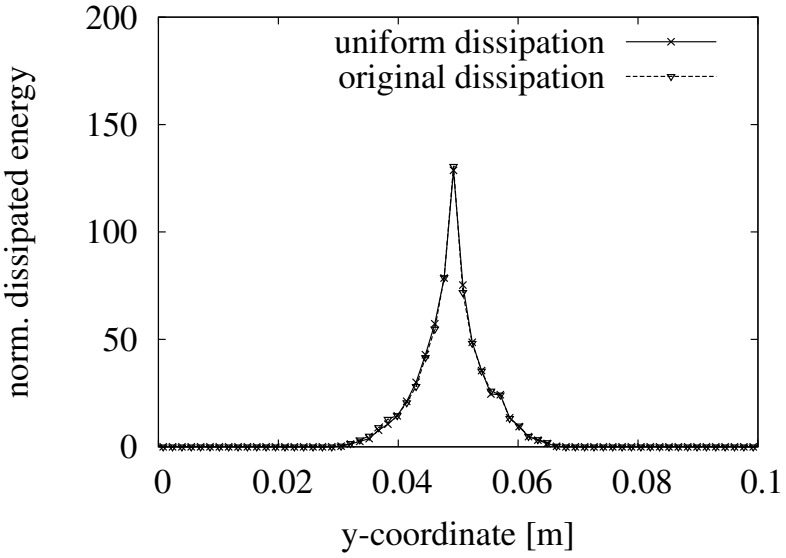

Figure 5.7: Comparison of the reconstructed and the original dissipated energy density profiles for the auto-correlation length $l_{\mathrm{a}} = 1$ mm.

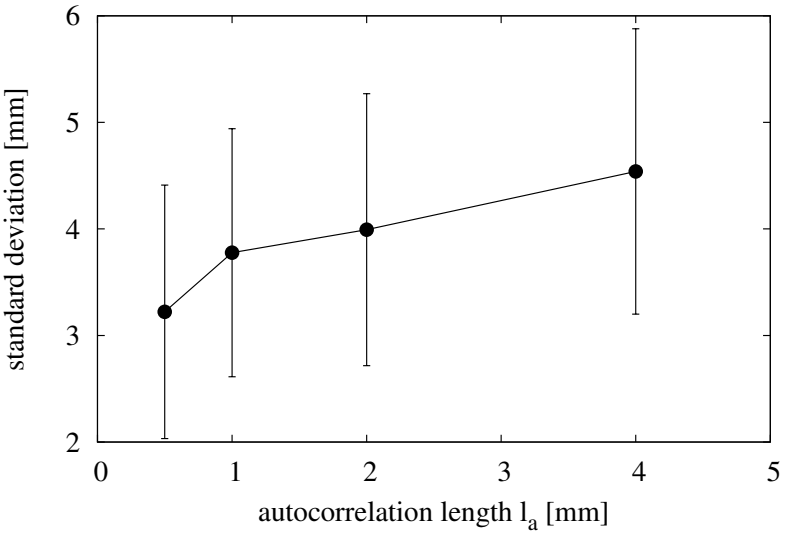

Figure 5.8: Influence of the auto-correlation length l_{a} on the mean of the standard deviation Δh obtained from 100 meso-scale analyses.

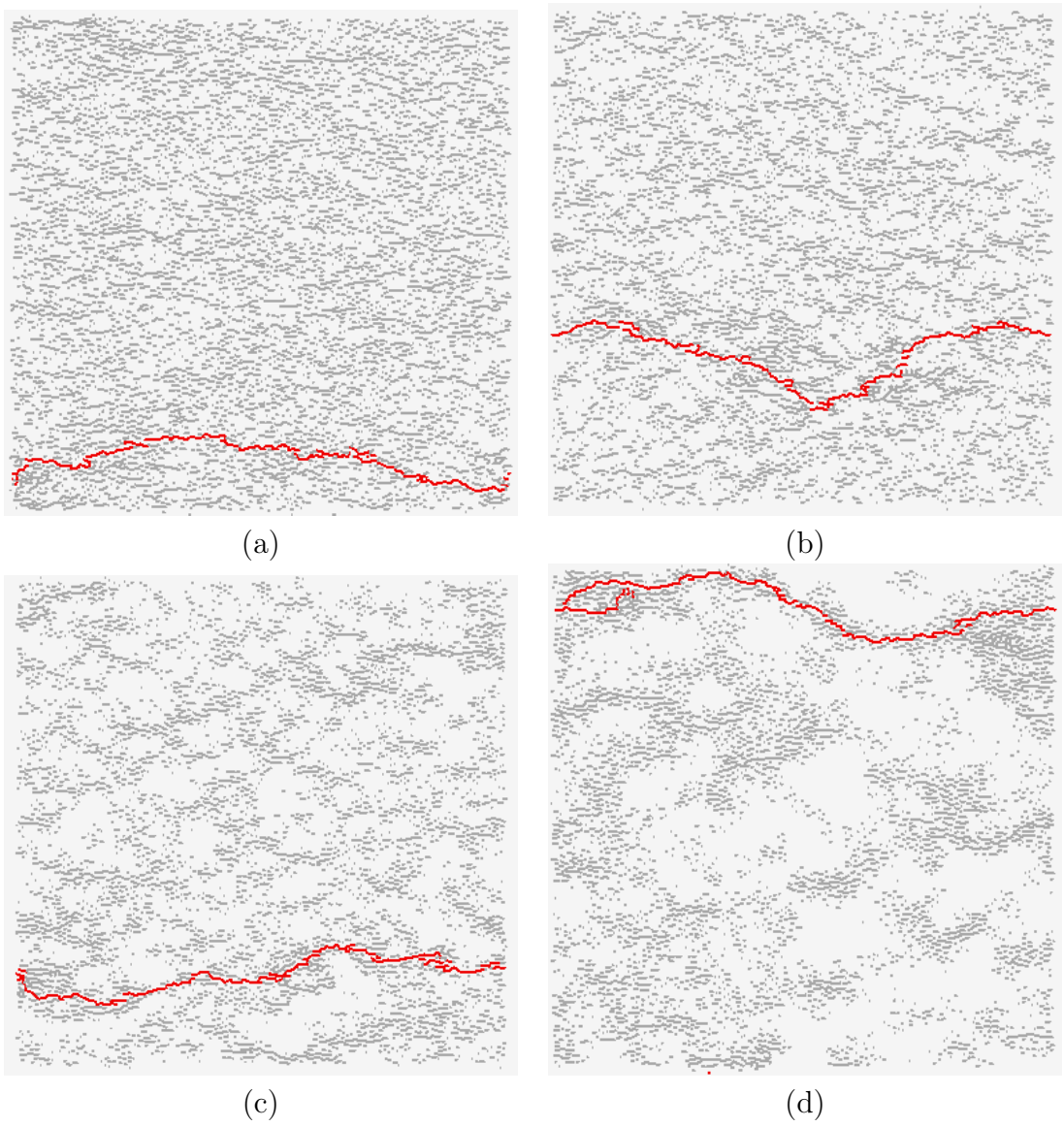

Figure 5.9: Final crack patterns for autocorrelation lengths (a) $l_a = 0.5$, (b) 1, (c) 2 and (d) 4 mm.

appears to be smaller than for for $l_a = 1$ mm. However, the relationship between l_a and the average Δh shown in Figure 5.8 is evident in the average response of 100 analyses.

The overall response of the analyses with the three different autocorrelation lengths is very similar to those with $l_a = 1$ mm. Again, the majority of energy is dissipated in a single localised crack. The ratio of localised energy dissipated in the final crack versus the total energy dissipated is not influenced by l_a. For all three sets of analyses, approximately 80% of the energy is dissipated in the localised crack.

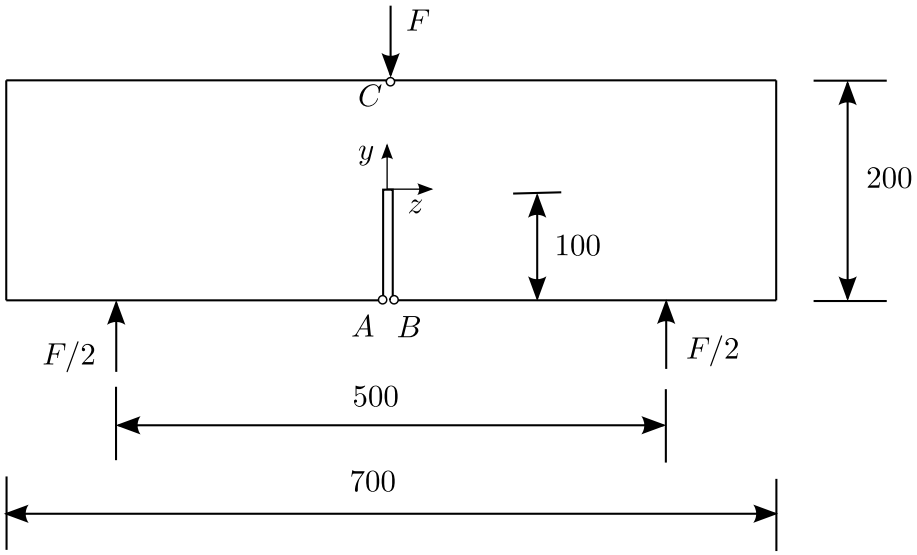

Figure 5.10: Geometry and loading setup of the three-point bending test for roughness measurements and nonlocal analysis. The out of plane thickness is 50 mm.

5.3 Application

In this section, an application of the calibration procedure, introduced in Section 5.1, is described. Firstly, the author scanned the experimental fracture surfaces of a beam subjected to three-point bending, which was originally tested in Grégoire et al. (2015). The standard deviation Δh_{exp} was calculated according to the procedure described in Section 5.1. Then, the nonlocal isotropic damage model B, presented in Section 3.1.1, was combined with distance-based averaging, described in (4.1) and (4.9), and was calibrated. The interaction radius was specified so that the standard deviation of the dissipated energy density profile from the analysis the 1D specimen subjected to tension matched the experimental one. The calibrated material model was applied to model in 2D the three-point bending test used to obtain the roughness distribution. The aim was to check if the FPZ calculated from the 2D analysis is in agreement with the one used for the calibration.

The notched beam used in the calibration was the HN200 specimen that was originally tested as part of study comparing the results of lattice modelling of fracture with acoustic emission measurements reported in Grégoire et al. (2015) and its geometry is shown in Figure 5.10. The mechanical concrete properties are: Young's modulus $E = 37$ GPa, tensile strength $f_{\text{t}} = 3.9$ MPa and Poisson's ratio $\nu = 0.2$. The concrete used in this test had a maximum aggregate size of 10 mm. For the fracture energy, a value of $G_{\text{F}} = 80$ J/m^2 was assumed in the present study. A focused area of the fracture surface away from the notch and the upper boundary of the specimen was scanned with an non-contact optical profiler Conoprobe 1000 with a lens with focal length 75 mm (Figure 5.11). The scans were performed in the Institut de Mécanique

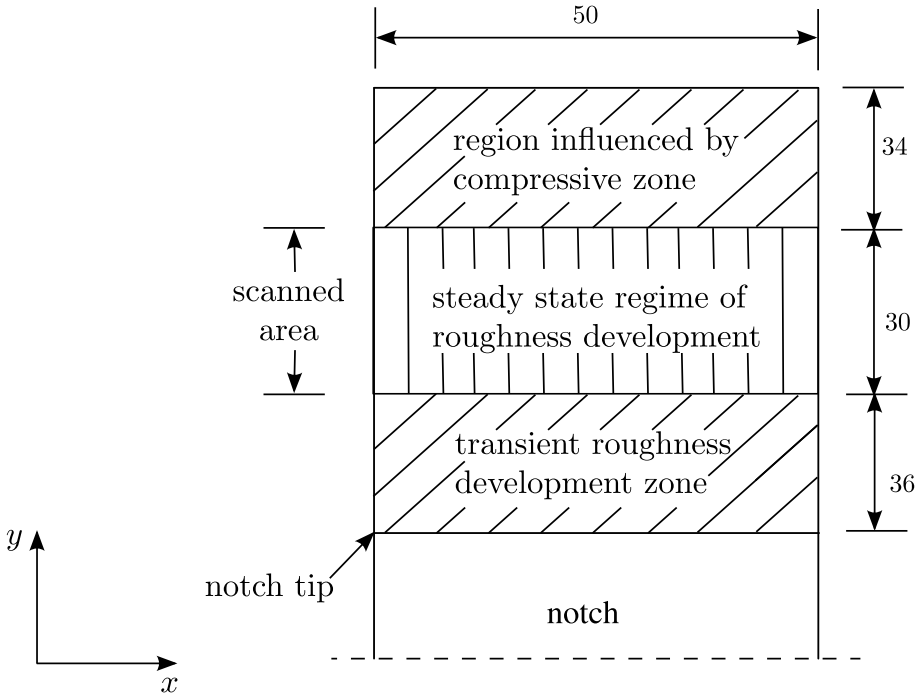

Figure 5.11: Geometry of the scanned region.

et d'Ingénierie of the University of Bordeaux. The scanned surface was statistically corrected, as discussed in Section 5.1, and the geometry of the roughness distribution with respect to the mean crack plane is shown in Figure 5.12. The standard deviation of the roughness distribution was calculated as $\Delta h_{\text{exp}} = 1.23$ mm.

The nonlocal interaction radius R was calibrated on a 1D tensile specimen so that the standard deviation of the dissipation density distribution Δh_{num} matches the experimental one, Δh_{exp}. The analysis setup was described in Section 3.8 but truss elements are used instead of 2D plane stress elements. The response is considered independent of boundaries by setting $\gamma = 1$ in the weight function $\alpha_0(\boldsymbol{x}, \boldsymbol{\xi})$ in (4.9) for all points along the 1D specimen. The purpose of the 1D nonlocal analysis is to specify the interaction radius R that will be used in 2D analyses and the nonlocal averaging is modified to account for two-dimensional interactions. This is achieved by formulating the nonlocal equivalent strain for the 1D analyses according to (3.35). The input parameters for the nonlocal model related to stiffness and strength were chosen as $E = 37$ GPa, $\nu = 0.2$, $\varepsilon_0 = f_{\text{t}}/E = 0.000105$, based on the reported experimental values. The remaining two parameters, i.e. the interaction radius R and the softening parameter ε_{f}, are calibrated simultaneously so that the numerical standard deviation matches the experimental one ($\Delta h_{\text{num}} = \Delta h_{\text{exp}}$) and the energy dissipated per unit area of fracture surface is equal to the total numerical fracture energy per cross-sectional area. The values of the model parameters, specified from the calibration procedure, were $\varepsilon_{\text{f}} = 0.0062$ and $R = 0.48$ mm for $G_{\text{F}} = 80$ N/m^2. It is noted that the calibrated value of the interaction radius is significantly smaller than the value used in Chapter 4. This may be attributed to the very weak aggregates used the experiments under consideration that failed during fracture leading to low values of the experimental standard deviation of

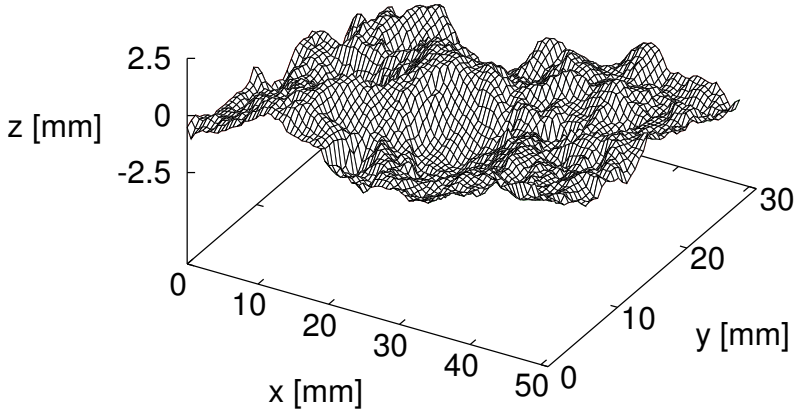

Figure 5.12: Surface plot of measured roughness after correction.

the crack surface from the mean crack plane. The stress-strain curve and the energy density profile is shown for the optimal set of parameters is shown in Figure 5.13.

In this application it was assumed that Δh_{exp} can be used to calibrate the input parameters of a nonlocal model used for 1D uniaxial direct tension analyses. To demonstrate the validity of this assumption, the calibrated nonlocal damage model was applied to analyse the notched beam used for the determination of the FPZ. The beam in Figure 5.10 is modelled by 2D triangular plane stress constant strain finite elements. The mesh in the middle region of the beam was refined to obtain a detailed representation of the dissipation density within the FPZ. In this analysis, the distance-based nonlocal averaging approach with parameters $\beta = 0.3$ and $t = 1$ was used in order to eliminate boundary effects (see Section 4.1). The analytical and experimental load-CMOD curves are shown in Figure 5.15(a). Furthermore, the profile of the average dissipated energy across the ligament of the beam for the focused region in Figure 5.11 is shown in Figure 5.15(b). The two dissipation density profiles in Figure 5.15 are very similar. However, the dissipation density in the 2D profile is slightly overestimated in the centre of the profile. The standard deviation computed from the dissipation profile is 1.35 mm, which is comparable to the experimental value of $\Delta h_{\text{exp}} = 1.23$ mm.

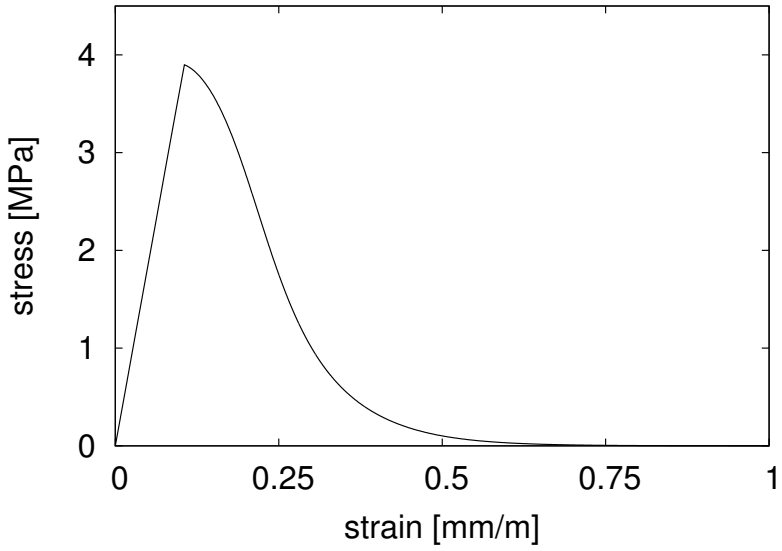

Figure 5.13: Average stress-strain curve of the 1D specimen subjected to direct tension

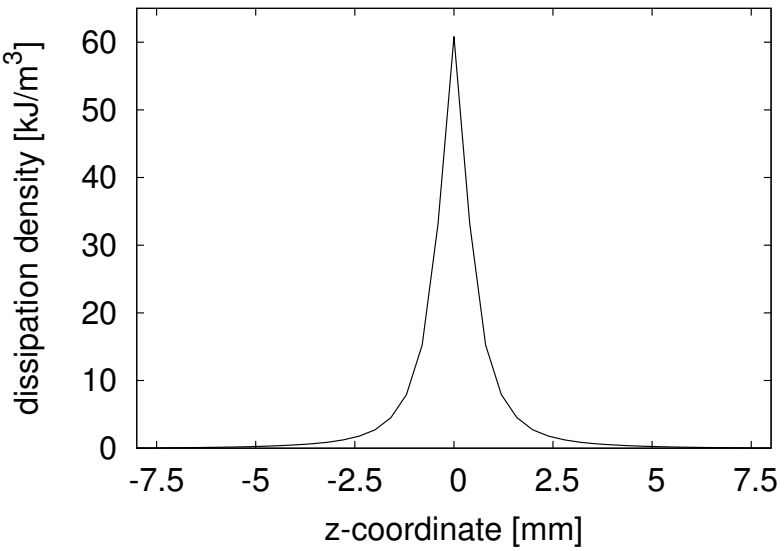

Figure 5.14: Dissipated energy density profile at the final loading stage in the centre of the 1D specimen subject to direct tension.

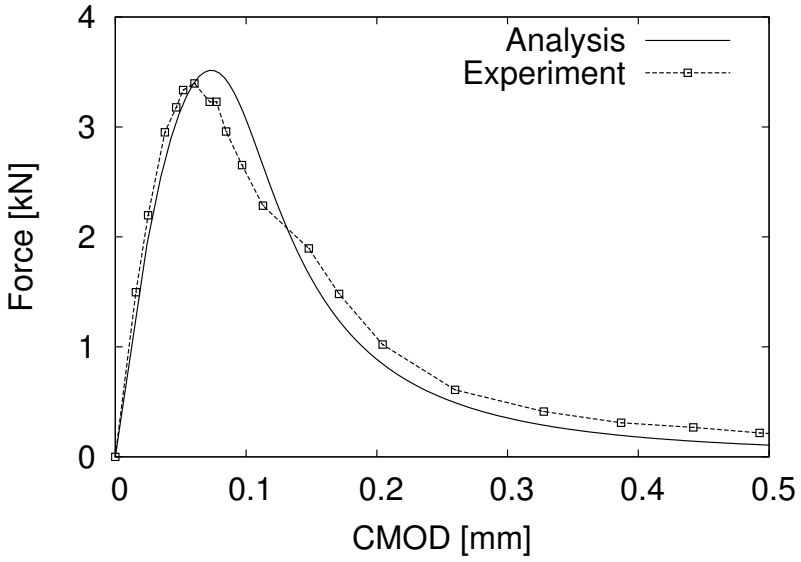

Figure 5.15: Comparison of the analytical and the experimental load-CMOD curves.

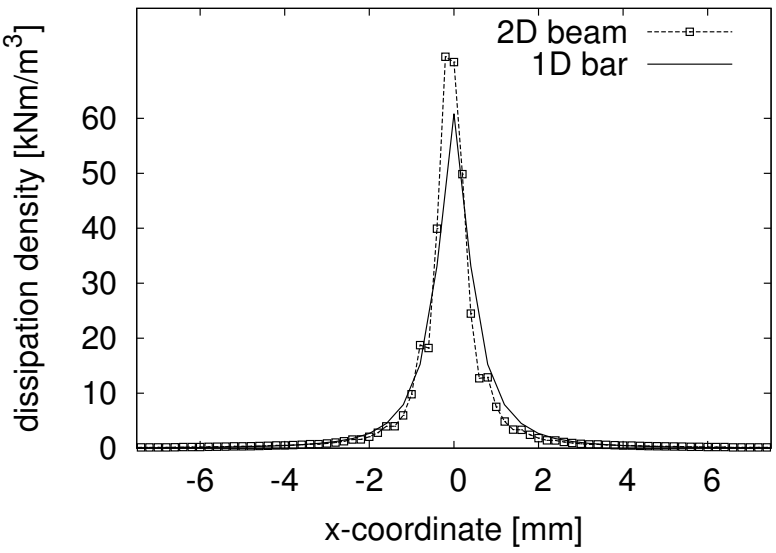

Figure 5.16: Comparison of the dissipation density profile of the 2D notched beam across the ligament and the profile from the 1D specimen subjected to direct tension.

5.4 Discussion

A new calibration strategy for integral-type nonlocal models was proposed. The fundamental assumption of the calibration process is that the majority of the fracture energy is dissipated in the main localised final crack, which was validated based on lattice analyses results of a periodic specimen subjected to direct tension. It was illustrated that approximately 80% of the total fracture energy is dissipated in the final localised crack, which is in agreement with the results presented in other studies, for example Cedolin et al. (1987). The local dissipation of each crack segment may be ignored in the calculation of the standard deviation of the roughness distribution without having a significant influence on the calculated value. The lattice analyses indicated that the width of the FPZ increases on average with increasing size of the heterogeneities, that were modelled by the autocorrelation length l_a of the random fields for strength and fracture energy. In the literature investigations on the size of the FPZ showed a similar trend between the d_{max} and the FPZ width (Mihashi et al., 1991; Otsuka and Date, 2000). The calculated FPZ width in the form of dissipated energy increment profiles does not become zero during the final loading steps. This illustrates that there is no direct link between the interaction radius and the damage levels as it was stated for example in (Pijaudier-Cabot and Dufour, 2010). The calibration strategy was applied and a nonlocal model was calibrated based on the experimental results of a beam subjected to three-point bending. It was concluded that the FPZ width observed in the 1D model, used for the calibration, is comparable to the one calculated from the 2D beam analysis results. Hence, the simplistic 1D model provides a good approximation of the FPZ away from the boundaries in the center of the beam and can be used in the calibration process.

Chapter 6

Modelling failure of reinforced concrete members with nonlocal and crack-band approaches

The last topic addressed in the present thesis is the capability of nonlocal and crack-band models to describe failure in reinforced concrete structures mesh-independently. The damage-plasticity model CDPM2, originally presented in Grassl et al. (2014), is extended according to the nonlocal approach. Permanent deformations observed in confined compression are represented in CDPM2 by plastic deformations. Multi-axial stress states are included in the formulation of the yield surface, which is characterised by parabolic meridians and by a variable shape on the deviatoric plane, ranging from triangular to almost circular for increasing confinement. The shape and the size of the yield surface and the plastic potential evolve during failure depending on the value of the hardening variable. Stiffness degradation is described by the damage part, in which two damage variables are applied to account for crack closing during non-proportional loading. The nonlocal and the crack-band models are applied for the analysis of a reinforced concrete beam (Leonhardt and Walther, 1962) and a column (Němeček et al., 2005) for which experimental results were reported in the literature. These tests were selected because the specimens exhibit both localised and distributed failure and the material points are subjected to various stress states. The material parameters were determined by a calibration procedure, which is based on the analysis of a one-dimensional bar subjected to direct tension, presented in Section 5.3. The results of the two approaches are compared in the form of load-displacement curves as well as contour plots of principal strains and damage variables.

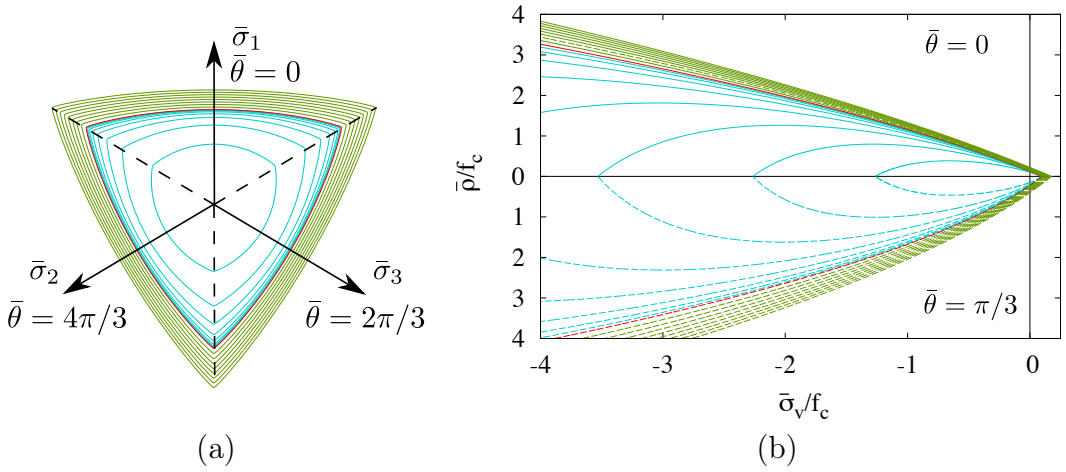

(a) (b)

Figure 6.1: Evolution of the (a) deviatoric section of the yield surface for a constant volumetric stress of $\bar{\sigma}_\mathrm{v} = -f_\mathrm{c}/3$ and of (b) the meridional sections for $\bar{\theta} = 0$ and $\bar{\theta} = \pi/3$ during hardening. Cyan, red and green sections correspond to values of κ_p that refer to stress states in the pre-peak domain, at peak stress and in the post-peak domain.

6.1 Local concrete damage-plasticity model CDPM2

The concrete damage-plasticity model CDPM2 is based on a combination of damage mechanics and effective stress-based plasticity. The effective stress $\bar{\boldsymbol{\sigma}}$ is calculated from the plasticity part

$$\bar{\boldsymbol{\sigma}} = \boldsymbol{D}_\mathrm{e} \left(\boldsymbol{\varepsilon} - \boldsymbol{\varepsilon}_\mathrm{p} \right) \tag{6.1}$$

The evaluation of the stress-strain law relies on the split of the effective stress $\bar{\boldsymbol{\sigma}}$ in a tensile $\bar{\boldsymbol{\sigma}}_\mathrm{t}$ and a compressive $\bar{\boldsymbol{\sigma}}_\mathrm{c}$ part, which is achieved in several steps. Firstly, the principal effective stress $\bar{\boldsymbol{\sigma}}_\mathrm{P}$ is decomposed in a positive $\bar{\boldsymbol{\sigma}}_\mathrm{Pt} =< \bar{\boldsymbol{\sigma}}_\mathrm{P} >_+$ and a negative $\bar{\boldsymbol{\sigma}}_\mathrm{Pc} =< \bar{\boldsymbol{\sigma}}_\mathrm{P} >_-$ part based on the sign of the principal components. Here, $< . >_+$ and $< . >_-$ denote the positive and negative part operators. Then, $\bar{\boldsymbol{\sigma}}_\mathrm{Pt}$ and $\bar{\boldsymbol{\sigma}}_\mathrm{Pc}$ are rotated back to the original coordinate system in order to form $\bar{\boldsymbol{\sigma}}_\mathrm{t}$ and $\bar{\boldsymbol{\sigma}}_\mathrm{c}$. The constitutive relationship is formulated as

$$\boldsymbol{\sigma} = \left(1 - \omega_\mathrm{t}\right) \bar{\boldsymbol{\sigma}}_\mathrm{t} + \left(1 - \omega_\mathrm{c}\right) \bar{\boldsymbol{\sigma}}_\mathrm{c} \tag{6.2}$$

where ω_t and ω_c are the two scalar damage parameters, ranging from 0 (undamaged) to 1 (fully damaged).

In the plasticity part, the domain of admissible effective stress states is described by the yield function $f_\mathrm{p}(\bar{\sigma}_\mathrm{v}, \bar{\rho}, \bar{\theta}, \kappa_\mathrm{p})$ formulated in the principal effective stress (Haigh-Westergaard) space using the volumetric stress $\bar{\sigma}_\mathrm{v}$, the deviatoric effective stress $\bar{\rho}$ and

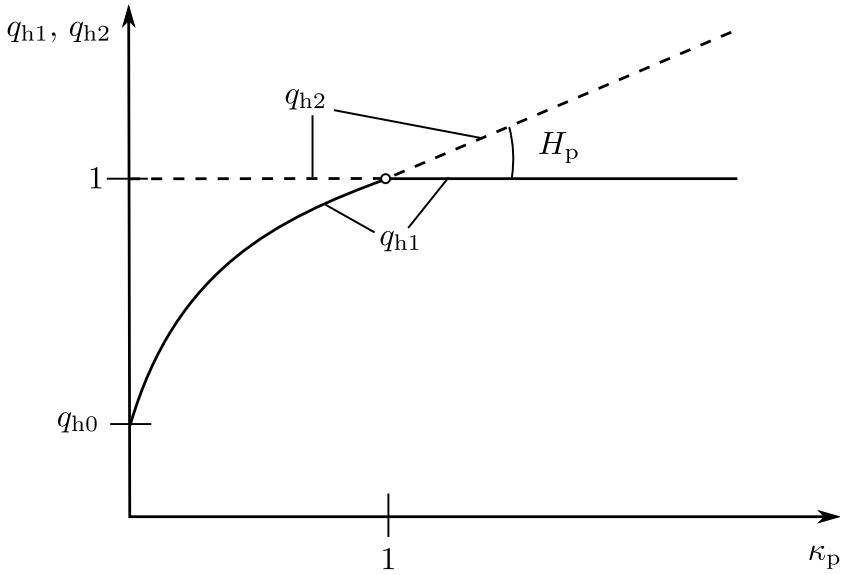

Figure 6.2: The two hardening laws q_{h1} (solid line) and q_{h2} (dashed line).

the Lode angle $\bar{\theta}$ as coordinates (Figure 6.1). The yield surface has the form

$$f_p(\bar{\sigma}_V, \bar{\rho}, \bar{\theta}; \kappa_p) = \left\{ [1 - q_{h1}(\kappa_p)] \left(\frac{\bar{\rho}}{\sqrt{6} f_c} + \frac{\bar{\sigma}_V}{f_c} \right)^2 + \sqrt{\frac{3}{2}} \frac{\bar{\rho}}{f_c} \right\}^2 + m_0 q_{h1}^2(\kappa_p) q_{h2}(\kappa_p) \left[\frac{\bar{\rho}}{\sqrt{6} f_c} r(\cos\bar{\theta}) + \frac{\bar{\sigma}_V}{f_c} \right] - q_{h1}^2(\kappa_p) q_{h2}^2(\kappa_p) \tag{6.3}$$

Here, q_{h1}, q_{h2} are the hardening functions of the hardening variable κ_p (Figure 6.2). The parameters f_c and f_t are the compressive and tensile strength of concrete. The meridians of the yield surface $f_p = 0$ are parabolic, and the deviatoric sections vary from triangular at low confinement to almost circular, according to the values of the function $r(\cos\bar{\theta})$ (Willam and Warnke, 1974), as given in

$$r(\cos\bar{\theta}) = \frac{4(1-e^2)\cos^2\bar{\theta} + (2e-1)^2}{2(1-e^2)\cos\bar{\theta} + (2e-1)\sqrt{4(1-e^2)\cos^2\bar{\theta} + 5e^2 - 4e}} \tag{6.4}$$

The eccentricity parameter e in (6.4), is calculated according to the formula specified in Jirásek and Bažant (2002), p. 365:

$$e = \frac{1+\epsilon}{2-\epsilon}, \text{ where } \epsilon = \frac{f_t}{f_{bc}} \frac{f_{bc}^2 - f_c^2}{f_c^2 - f_t^2} \tag{6.5}$$

where f_{bc} is the strength in equibiaxial compression. The friction parameter m_0 is calculated as

$$m_0 = \frac{3\,(f_c^2 - f_t^2)}{f_c f_t} \frac{e}{e+1} \tag{6.6}$$

The flow rule provides the direction of the plastic flow and is defined as

$$\dot{\boldsymbol{\varepsilon}}_p = \dot{\lambda} \frac{\partial g_p}{\partial \bar{\boldsymbol{\sigma}}} (\bar{\sigma}_v, \bar{\rho}, \kappa_p) \tag{6.7}$$

Here $\dot{\boldsymbol{\varepsilon}}_{\mathrm{p}}$ is the rate of the plastic strains, $\dot{\lambda}$ is the rate of the plastic multiplier and $g_{\mathrm{p}}(\bar{\sigma}_{\mathrm{v}}, \bar{\rho}, \kappa_{\mathrm{p}})$ is the plastic potential function. The flow rule is non-associated, i.e. the yield function f_{p} and the plastic potential g_{p} do not coincide, which results in a better description of the volumetric expansion during confined compression (Grassl, 2004). The plastic potential is

$$\begin{aligned} g_{\mathrm{p}}(\bar{\sigma}_{\mathrm{V}}, \bar{\rho}; \kappa_{\mathrm{p}}) = & \left\{ [1 - q_{\mathrm{h1}}(\kappa_{\mathrm{p}})] \left(\frac{\bar{\rho}}{\sqrt{6} f_{\mathrm{c}}} + \frac{\bar{\sigma}_{\mathrm{V}}}{f_{\mathrm{c}}} \right)^2 + \sqrt{\frac{3}{2}} \frac{\bar{\rho}}{f_{\mathrm{c}}} \right\}^2 \\ & + q_{\mathrm{h1}}^2(\kappa_{\mathrm{p}}) \left(\frac{m_0 \bar{\rho}}{\sqrt{6} f_{\mathrm{c}}} + \frac{m_{\mathrm{g}}(\bar{\sigma}_{\mathrm{V}}, \kappa_{\mathrm{p}})}{f_{\mathrm{c}}} \right) \end{aligned} \tag{6.8}$$

where

$$m_{\mathrm{g}}(\bar{\sigma}_{\mathrm{V}}, \kappa_{\mathrm{p}}) = A_{\mathrm{g}}(\kappa_{\mathrm{p}})\, B_{\mathrm{g}}(\kappa_{\mathrm{p}})\, f_{\mathrm{c}} \exp \frac{\bar{\sigma}_{\mathrm{V}} - q_{\mathrm{h2}}(\kappa_{\mathrm{p}}) f_{\mathrm{t}}/3}{B_{\mathrm{g}}(\kappa_{\mathrm{p}})\, f_{\mathrm{c}}} \tag{6.9}$$

is a variable controlling the ratio of volumetric and deviatoric plastic flow. The functions $A_{\mathrm{g}}(\kappa_{\mathrm{p}})$ and $B_{\mathrm{g}}(\kappa_{\mathrm{p}})$ depend on the value of $q_{\mathrm{h2}}(\kappa_{\mathrm{p}})$ and are derived from assumptions on the plastic flow in uniaxial tension and compression in the post-peak regime.

The calibration of $A_{\mathrm{g}}(\kappa_{\mathrm{p}})$ and $B_{\mathrm{g}}(\kappa_{\mathrm{p}})$ is illustrated in the next two paragraphs. Here, the notation $\mathbf{m} \equiv \dfrac{\partial g_{\mathrm{p}}}{\partial \boldsymbol{\sigma}}$ is adopted. In the principal stress space, the plastic flow tensor $\mathbf{m}$ has three components, m_1, m_2 and m_3 associated with the three principal stress components. The flow rule (6.7) is split into a volumetric and a deviatoric part and the gradient of the plastic potential is decomposed in

$$\mathbf{m} = \frac{\partial g}{\partial \bar{\boldsymbol{\sigma}}} = \frac{\partial g}{\partial \bar{\sigma}_{\mathrm{V}}} \frac{\partial \bar{\sigma}_{\mathrm{V}}}{\partial \bar{\boldsymbol{\sigma}}} + \frac{\partial g}{\partial \bar{\rho}} \frac{\partial \bar{\rho}}{\partial \bar{\boldsymbol{\sigma}}} \tag{6.10}$$

Taking into account that $\partial \bar{\sigma}_{\mathrm{V}} / \partial \bar{\boldsymbol{\sigma}} = \boldsymbol{\delta}/3$ and $\partial \bar{\rho} / \partial \bar{\boldsymbol{\sigma}} = \bar{\boldsymbol{s}}/\bar{\rho}$, restricting attention to the post-peak regime (in which $q_{\mathrm{h1}} = 1$) and differentiating the plastic potential (6.8), we rewrite equation (6.10) as

$$\mathbf{m} = \frac{\partial g}{\partial \bar{\boldsymbol{\sigma}}} = \frac{\partial m_{\mathrm{g}}}{\partial \bar{\sigma}_{\mathrm{V}}} \frac{\boldsymbol{\delta}}{3 f_{\mathrm{c}}} + \left(\frac{3}{f_{\mathrm{c}}} + \frac{m_0}{\sqrt{6} \bar{\rho}} \right) \frac{\bar{\boldsymbol{s}}}{f_{\mathrm{c}}} \tag{6.11}$$

Experimental results for concrete loaded in uniaxial tension indicate that the strains perpendicular to the loading direction are elastic in the softening regime. Thus, the plastic strain rate in these directions should be equal to zero ($m_2 = m_3 = 0$). Under uniaxial tension, the effective stress state in the post-peak regime is characterised by $\bar{\sigma}_1 = f_{\mathrm{t}} q_{\mathrm{h2}}$, $\bar{\sigma}_2 = \bar{\sigma}_3 = 0$, $\bar{\sigma}_{\mathrm{V}} = f_{\mathrm{t}} q_{\mathrm{h2}}/3$, $\bar{s}_1 = 2 f_{\mathrm{t}} q_{\mathrm{h2}}/3$, $\bar{s}_2 = \bar{s}_3 = -f_{\mathrm{t}} q_{\mathrm{h2}}/3$ and $\bar{\rho} = \sqrt{2/3} f_{\mathrm{t}} q_{\mathrm{h2}}$. Substituting this into (6.11) and enforcing the condition $m_2 = m_3 = 0$, we obtain

$$\frac{\partial m_{\mathrm{g}}}{\partial \bar{\sigma}_{\mathrm{V}}} \Big|_{\bar{\sigma}_{\mathrm{V}} = f_{\mathrm{t}} q_{\mathrm{h2}}/3} = \frac{3 f_{\mathrm{t}} q_{\mathrm{h2}}}{f_{\mathrm{c}}} + \frac{m_0}{2} \tag{6.12}$$

In uniaxial compression experiments, a volumetric expansion is observed in the softening regime. Thus, the inelastic lateral strains are positive while the inelastic axial strain is negative. In the present approach, a constant ratio $D_\mathrm{f} = -m_2/m_1 = -m_3/m_1$ between lateral and axial plastic strain rates in the softening regime is assumed. The effective stress state at the end of hardening under uniaxial compression is characterised by $\bar{\sigma}_1 = -f_\mathrm{c} q_\mathrm{h2}$, $\bar{\sigma}_2 = \bar{\sigma}_3 = 0$, $\bar{\sigma}_\mathrm{V} = -f_\mathrm{c} q_\mathrm{h2}/3$, $\bar{s}_1 = -2f_\mathrm{c} q_\mathrm{h2}/3$, $\bar{s}_2 = \bar{s}_3 = f_\mathrm{c} q_\mathrm{h2}/3$ and $\bar{\rho} = \sqrt{2/3} f_\mathrm{c} q_\mathrm{h2}$. Substituting this into (6.11) and enforcing the condition $m_2 = m_3 = -D_\mathrm{f} m_1$, we get

$$\frac{\partial m_\mathrm{g}}{\partial \bar{\sigma}_\mathrm{V}} \Big|_{\bar{\sigma}_\mathrm{V} = -f_\mathrm{c} q_\mathrm{h2}/3} = \frac{2D_\mathrm{f} - 1}{D_\mathrm{f} + 1} \left(3q_\mathrm{h2} + \frac{m_0}{2} \right) \tag{6.13}$$

Substituting the specific expression for $\partial m_\mathrm{g}/\partial \bar{\sigma}_\mathrm{V}$ constructed by differentiation of (6.9) into (6.12) and (6.13), we obtain two equations from which parameters

$$A_\mathrm{g} = \frac{3f_\mathrm{t} q_\mathrm{h2}}{f_\mathrm{c}} + \frac{m_0}{2} \tag{6.14}$$

$$B_\mathrm{g} = \frac{(q_\mathrm{h2}/3)\,(1 + f_\mathrm{t}/f_\mathrm{c})}{\ln A_\mathrm{g} - \ln(2D_\mathrm{f} - 1) - \ln(3q_\mathrm{h2} + m_0/2) + \ln(D_\mathrm{f} + 1)} \tag{6.15}$$

can be computed. The gradient of the dilation variable m_g in (6.9) decreases with increasing confinement. The limit $\bar{\sigma}_\mathrm{V} \to -\infty$ corresponds to purely deviatoric flow. Similarly to the previous version of the constitutive law, CDPM1 (Grassl and Jirásek, 2006b), the plastic potential does not depend on the third Haigh-Westergaard coordinate (Lode angle $\bar{\theta}$).

The dimensionless hardening functions q_h1 and q_h2, introduced in (6.3) and (6.8), depend on the value of the hardening variable κ_p and control the size and the shape of the yield surface and the plastic potential. The first hardening law is

$$q_\mathrm{h1}(\kappa_\mathrm{p}) = \begin{cases} q_\mathrm{h0} + (1 - q_\mathrm{h0})\left(\kappa_\mathrm{p}^3 - 3\kappa_\mathrm{p}^2 + 3\kappa_\mathrm{p}\right) - H_\mathrm{p}\left(\kappa_\mathrm{p}^3 - 3\kappa_\mathrm{p}^2 + 2\kappa_\mathrm{p}\right) & \text{if } \kappa_\mathrm{p} < 1 \\ 1 & \text{if } \kappa_\mathrm{p} \geq 1 \end{cases} \tag{6.16}$$

The second hardening law q_h2 is given by

$$q_\mathrm{h2}(\kappa_\mathrm{p}) = \begin{cases} 1 & \text{if } \kappa_\mathrm{p} < 1 \\ 1 + H_\mathrm{p}(\kappa_\mathrm{p} - 1) & \text{if } \kappa_\mathrm{p} \geq 1 \end{cases} \tag{6.17}$$

The initial inclination of the hardening curve q_h1 at $\kappa_\mathrm{p} = 0$ is positive and finite, and the inclinations of q_h1 on the left of $\kappa_\mathrm{p} = 1$ and q_h2 on the right of $\kappa_\mathrm{p} = 1$ are equal to H_p, as depicted in Figure 6.2. For $H_\mathrm{p} = 0$, the hardening law reduces to the one proposed in Grassl and Jirásek (2006b). The hardening variable κ_p is defined in rate form

$$\dot{\kappa}_\mathrm{p} = \frac{\|\dot{\boldsymbol{\varepsilon}}_\mathrm{p}\|}{x_\mathrm{h}(\bar{\sigma}_\mathrm{V})} \left(2\cos\bar{\theta}\right)^2 = \frac{\dot{\lambda}\|\boldsymbol{m}\|}{x_\mathrm{h}(\bar{\sigma}_\mathrm{V})} \left(2\cos\bar{\theta}\right)^2 \tag{6.18}$$

Here, the rate of the hardening variable is equal to the norm of the plastic strain rate scaled by a hardening ductility measure

$$x_{\mathrm{h}}\left(\bar{\sigma}_{\mathrm{V}}\right) = \begin{cases} A_{\mathrm{h}} - \left(A_{\mathrm{h}} - B_{\mathrm{h}}\right) \exp\left(-R_{\mathrm{h}}(\bar{\sigma}_{\mathrm{V}})/C_{\mathrm{h}}\right) & \text{if } R_{\mathrm{h}}(\bar{\sigma}_{\mathrm{V}}) \geq 0 \\ E_{\mathrm{h}} \exp(R_{\mathrm{h}}(\bar{\sigma}_{\mathrm{V}})/F_{\mathrm{h}}) + D_{\mathrm{h}} & \text{if } R_{\mathrm{h}}(\bar{\sigma}_{\mathrm{V}}) < 0 \end{cases} \tag{6.19}$$

For pure volumetric stress states, $\bar{\theta}$ is not uniquely defined and it is set in 6.19 to $\pi/3$. The dependence of the scaling factor x_{h} on the volumetric stress $\bar{\sigma}_{\mathrm{V}}$ is constructed such that the model response is more ductile under compression than in tension. The variable

$$R_{\mathrm{h}}(\bar{\sigma}_{\mathrm{V}}) = -\frac{\bar{\sigma}_{\mathrm{V}}}{f_{\mathrm{c}}} - \frac{1}{3} \tag{6.20}$$

is a linear function of the volumetric effective stress. Model parameters $A_{\mathrm{h}}, B_{\mathrm{h}}, C_{\mathrm{h}}$ and D_{h} are calibrated from the values of strain at peak stress under uniaxial tension, uniaxial compression and triaxial compression, whereas the parameters E_{h} and F_{h} are determined from the conditions of a smooth transition between the two parts of equation (6.19) at $R_{\mathrm{h}} = 0$:

$$\begin{aligned} E_{\mathrm{h}} &= B_{\mathrm{h}} - D_{\mathrm{h}} \\ F_{\mathrm{h}} &= \frac{\left(B_{\mathrm{h}} - D_{\mathrm{h}}\right) C_{\mathrm{h}}}{A_{\mathrm{h}} - B_{\mathrm{h}}} \end{aligned} \tag{6.21}$$

This definition of the hardening variable is identical to the one in CDPM1 described in Grassl and Jirásek (2006b), where the calibration procedure for this part of the model is described.

The loading-unloading conditions are

$$f_{\mathrm{p}} \leq 0, \qquad \dot{\lambda} \geq 0, \qquad \dot{\lambda}\, f_{\mathrm{p}} = 0 \tag{6.22}$$

In the damage part, the evolution of ω_{t} and ω_{c} is controlled for tension and compression by variables $\varepsilon^{\mathrm{t}}_{\mathrm{eq}}$ and $\varepsilon^{\mathrm{c}}_{\mathrm{eq}}$, which are functions of the equivalent strain $\varepsilon_{\mathrm{eq}}$. Damage is initiated when the maximum equivalent strain reaches the threshold $\varepsilon_0 = f_{\mathrm{t}}/E$. For uniaxial tension only, the equivalent strain could be chosen as $\varepsilon_{\mathrm{eq}} = \bar{\sigma}_{\mathrm{t}}/E$, where $\bar{\sigma}_{\mathrm{t}}$ is the effective uniaxial tensile stress and damage initiation would be linked to the axial elastic strain. However, for general triaxial stress states a more advanced equivalent strain expression is required, which predicts damage initiation when the strength envelope is reached. This expression is determined by solving a quadratic equation, that is defined by setting the yield surface ($f_{\mathrm{p}} = 0$) equal to 0. In this equation the hardening functions are set to $q_{\mathrm{h1}} = 1$ and $q_{\mathrm{h2}} = \varepsilon_{\mathrm{eq}}/\varepsilon_0$. The equivalent

strain $\varepsilon_{\mathrm{eq}}$ is then determined as the solution of the quadratic equation as

$$\varepsilon_{\mathrm{eq}} = \frac{\varepsilon_0 m_0}{2}\left(\frac{\bar{\rho}}{\sqrt{6}f_{\mathrm{c}}}r\left(\cos\theta\right)+\frac{\bar{\sigma}_{\mathrm{V}}}{f_c}\right)+\sqrt{\frac{\varepsilon_0^2 m_0^2}{4}\left(\frac{\bar{\rho}}{\sqrt{6}f_{\mathrm{c}}}r\left(\cos\theta\right)+\frac{\bar{\sigma}_{\mathrm{V}}}{f_{\mathrm{c}}}\right)^2+\frac{3\varepsilon_0^2\bar{\rho}^2}{2f_{\mathrm{c}}^2}} \tag{6.23}$$

For uniaxial tension, the effective stress state is defined as $\bar{\sigma}_1 = \bar{\sigma}_{\mathrm{t}}$, $\bar{\sigma}_2 = \bar{\sigma}_3 = 0$, $\bar{\sigma}_{\mathrm{V}} = \bar{\sigma}_{\mathrm{t}}/3$, $\bar{s}_1 = 2\bar{\sigma}_{\mathrm{t}}/3$, $\bar{s}_2 = \bar{s}_3 = -\bar{\sigma}_{\mathrm{t}}/3$, $\bar{\rho} = \sqrt{2/3}\bar{\sigma}_{\mathrm{t}}$ and $r(\cos\theta) = 1/e$. Setting this into (6.23) and using the definition of m_0 in (6.6) gives

$$\varepsilon_{\mathrm{eq}} = \varepsilon_0\frac{\bar{\sigma}_{\mathrm{t}}}{f_{\mathrm{t}}} = \bar{\sigma}_{\mathrm{t}}/E \tag{6.24}$$

which is the axial tensile strain. For uniaxial compression, the effective stress state is defined as $\bar{\sigma}_1 = -\bar{\sigma}_{\mathrm{c}}$, $\bar{\sigma}_2 = \bar{\sigma}_3 = 0$, $\bar{\sigma}_{\mathrm{V}} = -\bar{\sigma}_{\mathrm{c}}/3$, $\bar{s}_1 = -2/3\bar{\sigma}_{\mathrm{c}}$, $\bar{s}_2 = \bar{s}_3 = 1/3\bar{\sigma}_{\mathrm{c}}$, $\bar{\rho} = \sqrt{2/3}\bar{\sigma}_{\mathrm{c}}$, and $r(\cos\theta) = 1$. Here, $\bar{\sigma}_{\mathrm{c}}$ is the magnitude of the effective compressive stress. Setting this into (6.23), the equivalent strain is

$$\varepsilon_{\mathrm{eq}} = \frac{\bar{\sigma}_{\mathrm{c}}\varepsilon_0}{f_{\mathrm{c}}} = \frac{\bar{\sigma}_{\mathrm{c}}f_{\mathrm{t}}}{Ef_{\mathrm{c}}} \tag{6.25}$$

If $\bar{\sigma}_{\mathrm{c}} = (f_{\mathrm{c}}/f_{\mathrm{t}})\bar{\sigma}_{\mathrm{t}}$, the equivalent strain is again equal to the axial elastic strain component σ_{t}/E in uniaxial tension. Consequently, the equivalent strain definition in (6.23) is suitable for both tension and compression, which is very convenient for relating the damage variables in tension and compression to stress-inelastic strain curves.

Furthermore, variables $\varepsilon^{\mathrm{t}}_{\mathrm{eq}}$ and $\varepsilon^{\mathrm{c}}_{\mathrm{eq}}$ are defined in rate form as $\dot{\varepsilon}^{\mathrm{t}}_{\mathrm{eq}} = \dot{\varepsilon}_{\mathrm{eq}}$ and $\dot{\varepsilon}^{\mathrm{c}}_{\mathrm{eq}} = \alpha_{\mathrm{c}}\dot{\varepsilon}_{\mathrm{eq}}$. Variable α_{c} is introduced to quantify the contribution of compression in the effective stress state and is calculated as

$$\alpha_{\mathrm{c}} = \sum_{i=1}^{3}\frac{\bar{\sigma}_{\mathrm{Pci}}\left(\bar{\sigma}_{\mathrm{Pti}}+\bar{\sigma}_{\mathrm{Pci}}\right)}{\|\bar{\boldsymbol{\sigma}}_{\mathrm{P}}\|^2} \tag{6.26}$$

where $\bar{\sigma}_{\mathrm{Pti}}$ and $\bar{\sigma}_{\mathrm{Pci}}$ are the components of the compressive and tensile part of the principal effective stresses, respectively, which were previously used for the general stress strain law in (6.2). The variable α_{c} varies from 0 for pure tension to 1 for pure compression.

The history variables form two groups of three variables, which are related to the tensile and the compressive part, respectively. They are formulated as

$$\begin{aligned}
\kappa_{\mathrm{dt}} &= \max_{\tau\le t}\varepsilon^{\mathrm{t}}_{\mathrm{eq}} \qquad \dot{\kappa}_{\mathrm{dt1}} = \frac{\|\dot{\varepsilon}_{\mathrm{p}}\|}{x_{\mathrm{s}}(\bar{\sigma}_{\mathrm{v}},\bar{\rho})} \qquad \dot{\kappa}_{\mathrm{dt2}} = \frac{\dot{\kappa}_{\mathrm{dt}}}{x_{\mathrm{s}}(\bar{\sigma}_{\mathrm{v}},\bar{\rho})} \\
\kappa_{\mathrm{dc}} &= \max_{\tau\le t}\varepsilon^{\mathrm{c}}_{\mathrm{eq}} \qquad \dot{\kappa}_{\mathrm{dc1}} = \frac{\alpha_{\mathrm{c}}\,\beta_{\mathrm{c}}\,\|\dot{\varepsilon}_{\mathrm{p}}\|}{x_{\mathrm{s}}(\bar{\sigma}_{\mathrm{v}},\bar{\rho})} \qquad \dot{\kappa}_{\mathrm{dc2}} = \frac{\dot{\kappa}_{\mathrm{dc}}}{x_{\mathrm{s}}(\bar{\sigma}_{\mathrm{v}},\bar{\rho})}
\end{aligned} \tag{6.27}$$

Here, the softening ductility measure $x_{\mathrm{s}}(\bar{\sigma}_{\mathrm{v}},\bar{\rho})$ is a function of $\bar{\sigma}_{\mathrm{v}}$ and $\bar{\rho}$, which takes into

account the influence of multi-axial stress states on damage evolution. It is formulated as

$$x_{\mathrm{s}} = 1 + (A_{\mathrm{s}} - 1)\, R_{\mathrm{s}} \tag{6.28}$$

where R_{s} is

$$R_{\mathrm{s}} = \begin{cases} -\dfrac{\sqrt{6}\bar{\sigma}_{\mathrm{V}}}{\bar{\rho}} & \text{if } \bar{\sigma}_{\mathrm{V}} \leq 0 \\ 0 & \text{if } \bar{\sigma}_{\mathrm{V}} > 0 \end{cases} \tag{6.29}$$

In this function, A_{s} is a model parameter. For uniaxial tension $\bar{\sigma}_{\mathrm{v}}/\bar{\rho} = -1/\sqrt{6}$, $R_{\mathrm{s}} = 1$ and $x_{\mathrm{s}} = A_{\mathrm{s}}$. In (6.27) factor β_{c} provides a smooth transition from pure damage to damage-plasticity softening processes during cyclic loading. It is given by

$$\beta_{\mathrm{c}} = \frac{f_{\mathrm{t}} q_{\mathrm{h2}} \sqrt{2/3}}{\bar{\rho}\sqrt{1 + 2D_{\mathrm{f}}^2}} \tag{6.30}$$

An exponential stress-strain damage law was selected for both the tensile and the compressive part. Damage is initiated when either the tensile or the compressive equivalent strain reaches $\varepsilon_0 = f_{\mathrm{t}}/E$. The dissipated energy is controlled by softening parameters $\varepsilon_{\mathrm{ft}}$ and $\varepsilon_{\mathrm{fc}}$ for tension and compression, which determine the initial slope of the softening curve (Figure 6.3). The history variables are used in the damage law to provide the value of the damage variable by calculating the inelastic strains in the equivalent 1D problem. The inelastic strain is defined for tensile damage as

$$\varepsilon_{\mathrm{in}}^{\mathrm{t}} = \kappa_{\mathrm{dt1}} + \omega_{\mathrm{t}} \kappa_{\mathrm{dt2}} \tag{6.31}$$

Furthermore, in this problem the stress-strain relationship is replaced by

$$\sigma = (1 - \omega_{\mathrm{t}}) E \kappa_{\mathrm{dt}} \tag{6.32}$$

An exponential stress-strain law is assumed

$$\sigma = f_{\mathrm{t}} \exp\left(-\frac{\varepsilon_{\mathrm{in}}^{\mathrm{t}}}{\varepsilon_{\mathrm{ft}}}\right) \quad \text{if} \quad \varepsilon_{\mathrm{in}}^{\mathrm{t}} > 0 \tag{6.33}$$

The damage parameter ω_{t} is calculated by iteratively solving for ω_{t} the equation constructed by substituting (6.31) into (6.33) and setting it equal to (6.32). The compressive damage parameter is evaluated by replacing in (6.31) - (6.33) the tensile history variables and equivalent strain with their compressive counterparts.

To sum up, the 13 parameter damage-plasticity model was described. The plasticity part is defined by nine parameters, from which the main ones are the compressive strength f_{c}, tensile strength f_{t} and parameter H_{p} of the hardening functions. The latter controls the amount of the plastic strains. The smaller the value of H_{p} is the closer is the response of the model to a pure plasticity constitutive law. The roundness

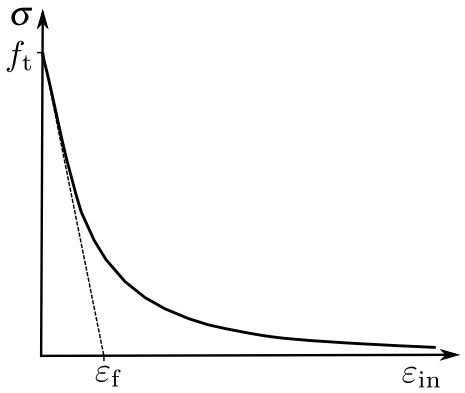

Figure 6.3: Exponential softening damage law

of the deviatoric sections is determined from parameter e which is calculated according to (6.5). Parameter D_f controls the ratio between lateral and axial plastic strains as described in (6.15). Initial hardening depends on the value of q_{h0}, used in (6.16), and the hardening ductility measure $x_h(\bar{\sigma}_v)$ consists of four parameters A_h, B_h, C_h, D_h, as shown in (6.19). Furthermore, the damage part is defined by four parameters, namely the strain ε_0 at which damage initiates, the strains ε_{ft} and ε_{fc} used in the damage laws for tension and compression and A_s of the ductility measure x_s in (6.28).

6.1.1 Implementation of CDPM2

The damage-plasticity model CDPM2 was implemented in the framework of nonlinear finite element method. The material response is evaluated at each Gauss point. For a new strain increment a trial elastic loading step is initially assumed. The trial stress state is initially corrected by the plasticity and then by the damage algorithm, as it was described in Grassl and Jirásek (2006b).

In the plasticity algorithm, stress states are treated differently depending on their position in the principal effective stress space with respect to the vertices of the yield surface, which lie at the intersections of the meridians with the hydrostatic axis (Figure 6.1). At these points, g_p is not differentiable and the direction of plastic flow $\boldsymbol{m}$ is not uniquely defined. Initially, it is checked whether the stress state lies within a region, that might require a vertex return, i.e. the stress state should be returned to the closest vertex on the hydrostatic axis. On the vertex, the yield condition is written as a function of the only unknown $\bar{\sigma}_v$ because on the hydrostatic axis $\bar{\rho} = 0$, $\bar{\theta}$ is set by default to $\pi/3$ and κ_p becomes a function of the trial stress state and σ_v. The bisection method is applied to find the vertex volumetric stress within the interval $[0, \bar{\sigma}_v^{trial}]$ or $[\bar{\sigma}_v^{trial}, 0]$ for tensile or compressive trial stress states, respectively. The solution is accepted if the vector connecting the trial and the vertex stress states is within the region

bounded by a cone including all vectors perpendicular to g_p on the vertex mapped in the effective stress space. Mapping from the strain to effective stress space is performed by multiplying their deviatoric and volumetric components with the shear modulus G and the bulk modulus K (Simo and Hughes, 2000). If a vertex return is unsuccessful, the regular return algorithm is applied to calculate the closest stress state on the yield surface from the trial stress state by applying a Closest Point Projection algorithm (Simo and Hughes, 2000). The problem can be reduced to the calculation of four unknowns including $\bar{\sigma}_v$, $\bar{\rho}$, $\dot{\lambda}$ and κ_p because the derivative of g_p with respect to $\bar{\theta}$ is zero so that $\bar{\theta}$ remains constant during regular return (Etse and Willam, 1996). For very large strain increments the plasticity algorithm cannot converge within a reasonable number of iterations or for very low tolerances. The robustness of the model is enhanced by applying a subincrementation scheme that relies in splitting large strain increments in subincrements, sequentially added to the strain vector. The intermediate effective stress states are then calculated after each addition by the plasticity algorithm.

The effective stress state evaluated from the plasticity part is corrected by the damage algorithm to provide the final stress. During the transition from tensile to compressive stress states in cyclic loading, ε_{eq}^{c}, κ_{dc} and κ_{dc2} depend on the value of α_c at the current load step. In a correct evaluation of ε_{eq}^{c} only the part of $\dot{\varepsilon}_{eq}$ corresponding to material reloading should be multiplied with the current α_c. This is not the case when unloading from tension and reloading in compression occur within a single load step. The miscalculation of ε_c and κ_{dc2} for $H_p = 0$, where elastic strains have low values and stay constant in the post-peak, results in an underprediction of the ε_{in}^{c} so that ω_c is not initiated properly and "lags behind" the effective stress. This problem is treated in the damage algorithm by initially detecting if unloading and reloading occurs in a single step. The value of ε_{eq} is calculated at two intermediate stress states that correspond to 1% and 99% of the total strain increment. Unloading and reloading within a single load step are assumed to occur, if the value of ε_{eq} decreases from the initial stress state to the first intermediate stress state and increases from the second intermediate stress state to the current stress state. In this case, the total strain increment is split in 100 subincrements which are sequentially added to the strain vector and the ε_{eq} is evaluated until its minimum value is reached. Then, the total increment of $\dot{\varepsilon}_{eq}^{c}$ is formulated as the sum of two increments between the three points, which correspond to the initial stress state, the point of minimum ε_{eq} and the final stress state. The values of α_c at the initial and the current stress state are used for the calculation of the first and the second increment, respectively.

6.2 Nonlocal approach

In the nonlocal approach, the equivalent strains and the rates of the history variables at a point $\boldsymbol{x}$ are calculated as weighted averages of the local ones, at each point $\boldsymbol{\xi}$ in the vicinity of $\boldsymbol{x}$. In the general case, the nonlocal average $\bar{f}(\boldsymbol{x})$ of a local function $f(\boldsymbol{x})$ is calculated as

$$\bar{f}(\boldsymbol{x}) = \int_V \alpha(\boldsymbol{x}, \boldsymbol{\xi}) f(\boldsymbol{\xi}) \mathrm{d}\boldsymbol{\xi} \tag{6.34}$$

Here, $\alpha(\boldsymbol{x}, \boldsymbol{\xi})$ is the weight function that describes the interactions between points $\boldsymbol{x}$ and $\boldsymbol{\xi}$ in the actual Euclidean space V, described in (3.10) and (3.11). The only parameter of this function is the interaction radius R, which is linked to the width of the final failure zones in tensile failure.

The main objective of the structural analyses is to investigate the mesh-dependence of the material models and not to accurately describe material failure close to boundaries. Moreover, the modified averaging schemes, presented in Section 4.1, aim at describing tensile failure but their performance in describing compressive failure, which is exhibited by the analysed specimens, has not been evaluated yet. The modified approaches would also increase the computational load and the number of the model parameters without influencing the mesh-dependence of the final solution compared to standard nonlocal averaging. Hence, the standard averaging approach, introduced in (3.10), is applied.

Nonlocal averaging was applied in both the tensile and the compressive damage part. The damage laws are based on stress-inelastic strain laws and the local history variables and equivalent strains used in (6.31) - (6.33) are replaced by their nonlocal counterparts, $\bar{\varepsilon}_{\mathrm{eq}}$, $\bar{\kappa}_{\mathrm{dt1}}$, $\bar{\kappa}_{\mathrm{dt2}}$, $\bar{\varepsilon}^{\mathrm{c}}_{\mathrm{eq}}$, $\bar{\kappa}_{\mathrm{dc1}}$, $\bar{\kappa}_{\mathrm{dc2}}$, which are calculated according to (6.34).

6.3 Crack-band approach

The tensile part of the damage algorithm is formulated according to the crack-band approach and fracture is modelled as a nonlinear band, that deforms inelastically. The inelastic behaviour is described by a stress-crack opening law and the exponential stress-inelastic strain law is replaced by a stress-inelastic displacement relationship calculated by multiplying inelastic strain in (6.31) with the width h of the crack-band.

The stress-inelastic displacement law for tension is then formulated as

$$\sigma_{\mathrm{t}} = f_{\mathrm{t}} \exp\left(-\frac{\varepsilon_{\mathrm{in}}^{\mathrm{t}} h}{w_{\mathrm{ft}}}\right) \quad \text{if} \quad \varepsilon_{\mathrm{in}}^{\mathrm{t}} > 0 \tag{6.35}$$

In the present study, the width of the crack-band is set equal to the maximum dimension of the element along the direction of the first principal strain at the onset of damage (Jirásek and Bauer, 2012).

6.4 Analyses

6.4.1 Calibration based on 1D direct tension test

The material models were calibrated based on the recommendations of FIB Model Code 2010 (FIB, 2012). The compressive strength f_{cm} was set equal to the value of the cylinder compressive strength, reported in the experiments (Leonhardt and Walther, 1962; Němeček et al., 2005). The Young's modulus E, the Poisson's ratio ν, the mean tensile strength f_{ctm} and the fracture energy G_{F} were determined based on the equations provided by CEB-FIB Model Code 2010 (FIB, 2012). The parameters of the material were calibrated by fitting the calculated material properties by analysing a 1D bar with length 0.25 m subjected to tension, which has been presented in Section 5.3. During the calibration procedure, the optimal values, proposed in Grassl et al. (2013), were used for the material parameter $q_{\mathrm{h0}} = 0.3$, $A_{\mathrm{h}} = 0.08, B_{\mathrm{h}} = 0.0033, C_{\mathrm{h}} = 2.0$, $D_{\mathrm{h}} = 10^{-6}$, $H_{\mathrm{p}} = 0.01$, $\varepsilon_{\mathrm{fc}} = 3\ 10^{-5}$ and $D_{\mathrm{f}} = 0.85$. In the analyses with the crack-band approach, failure localises in a single element and the model's tensile softening parameter w_{ft} is directly related to the fracture energy as $G_{\mathrm{f}} = f_{\mathrm{t}} w_{\mathrm{ft}}$. However, the nonlocal model is leading to a multi-element dissipation zone, whose width depends on the value of the interaction radius R.

In the present study, R was set equal to 0.01 m, which is much larger than the value provided for the interaction radius by the proposed calibration strategy in Section 5.3. Smaller values of R would require smaller mesh sizes to ensure that there are enough material points within the interaction domain for the calculation of the nonlocal averages, which would increase computational load. In addition, a value of R comparable to the one provided in Section 5.3 would lead to failure zones that are smaller than the experimental ones because no fractured aggregates were reported in these experiments (Leonhardt and Walther, 1962; Němeček et al., 2005). In the three-point bending test used for the calibration, the aggregates were characterised by low tensile strength

leading to smoother final fracture surfaces and lower standard deviation of the experimental roughness distribution. Therefore, the selected value of the interaction radius was considered to provide reasonably sized failure zones without the need of extremely fine meshes.

The calibrated models were applied to the nonlinear analysis of a reinforced concrete beam and a column in the two- and three-dimensional domain, respectively. Nonlocal interactions in 2D and 3D were taken into account in the calibration by applying the modified nonlocal weight functions, introduced in (3.36) and (3.37).

The parameter set, that will be used for the analysis of the reinforced concrete beam in Section 6.4.2, was applied to a mesh study to investigate the dependence of the two material models on the selected element size. A coarse, a medium and a fine mesh with 25, 51 and 101 elements of the 1D specimen with length 0.25 m were analysed with the calibrated crack-band and the nonlocal models. In the nonlocal models the modified weight function, introduced in (3.36), was used. Both approaches provide a mesh-independent description of the average stress-strain curves (Figures 6.4 and 6.5). The average stress is defined as the applied force divided by the cross-sectional area and the average strain is calculated as the applied displacement divided by the specimen length. The dissipated energy density profiles at the final loading step are illustrated in Figures 6.6 and 6.7. In the analyses with the crack-band approach, it is observed that for smaller mesh sizes the width of the localisation zone decreases and the value of the local dissipated energy density increases. On the contrary, the nonlocal approach results in mesh-insensitive representations of the dissipated energy density profile. In Figure 6.8, it is shown, that the plastic strain profiles are mesh-independent for $H_{\mathrm{p}} > 0$ in the nonlocal approach, which was illustrated previously for a simple damage-plasticity model in Grassl and Jirásek (2004).

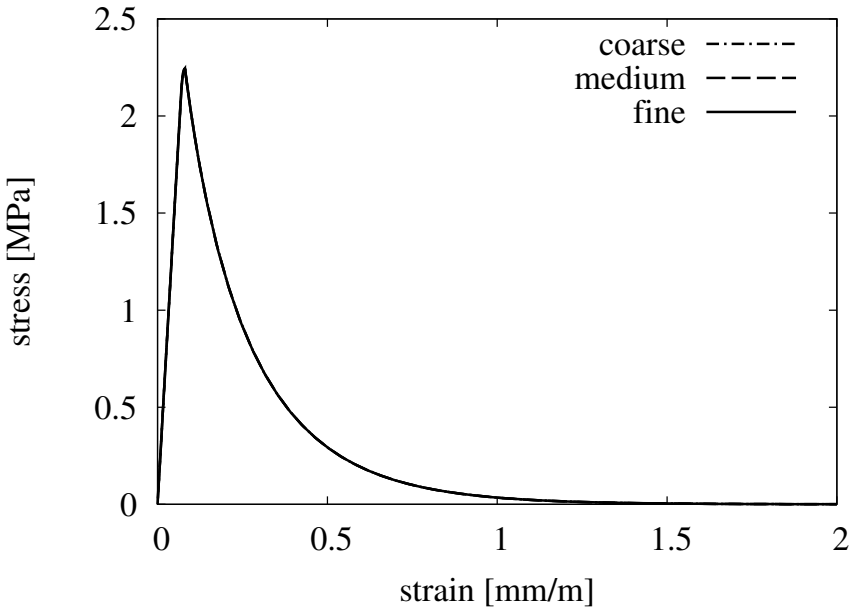

Figure 6.4: Comparison of the average stress-strain curves for the analysis with the crack-band model of the 1D direct tension test for three different meshes.

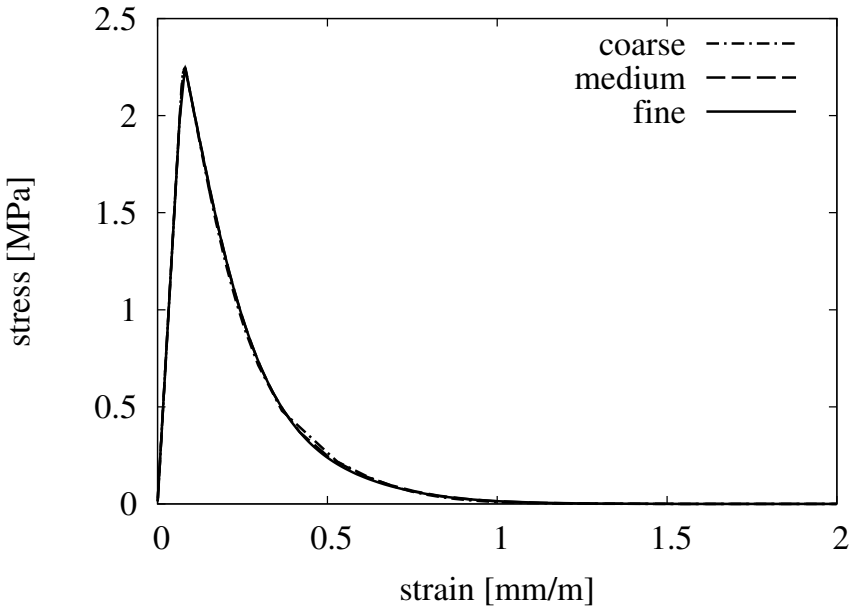

Figure 6.5: Comparison of the average stress-strain curves for the analysis with the nonlocal model of the 1D direct tension test for three different meshes.

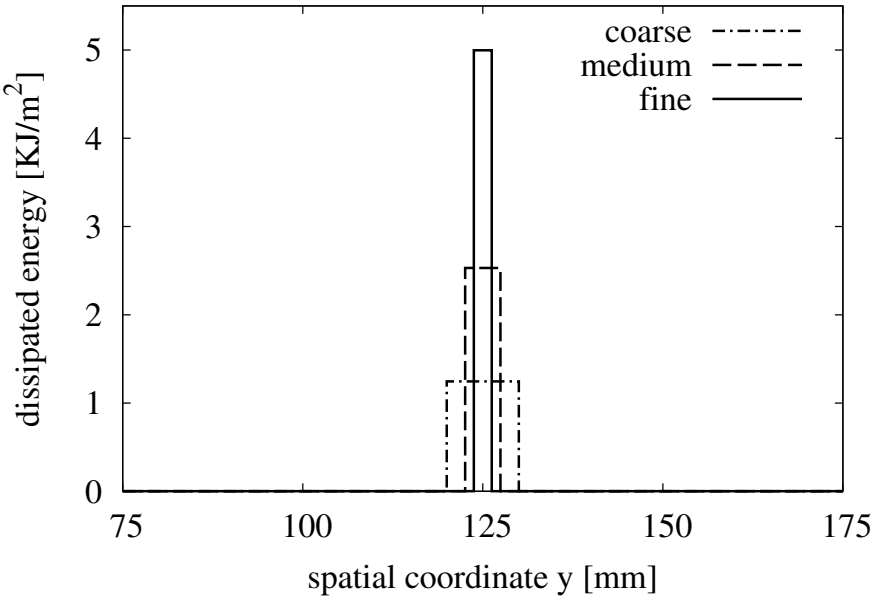

Figure 6.6: Comparison of the dissipated energy density profiles for the analysis with the crack-band model of the 1D direct tension test for three different meshes.

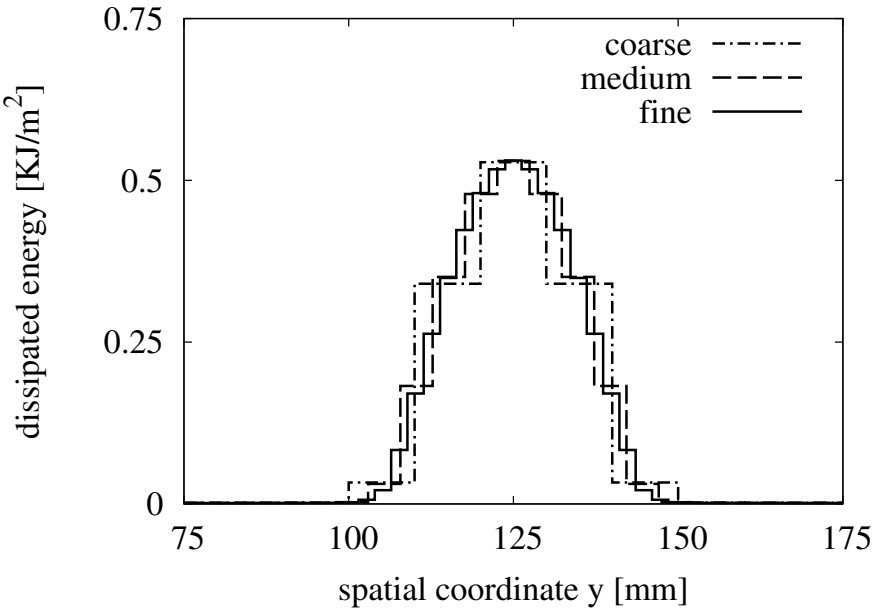

Figure 6.7: Comparison of the dissipated energy density profiles for the analysis with the nonlocal model of the 1D direct tension test for three different meshes.

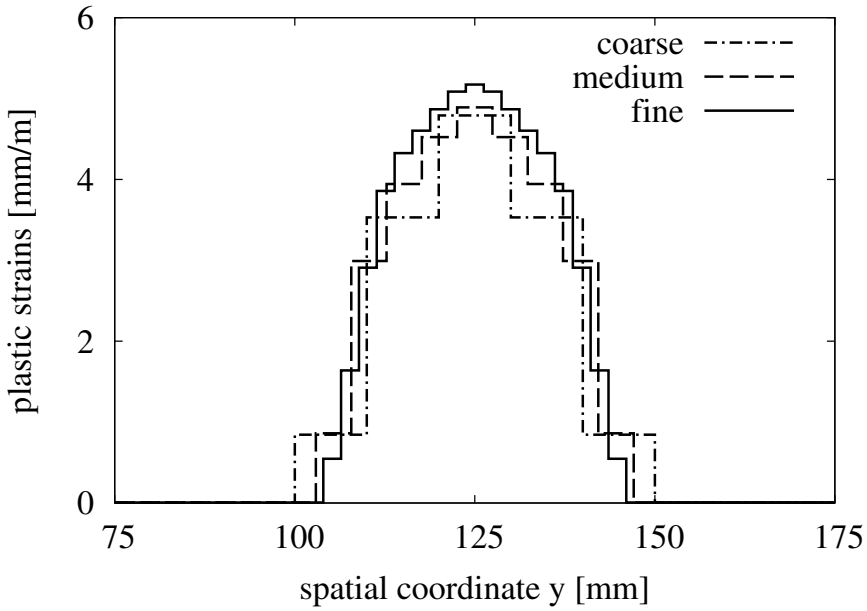

Figure 6.8: Comparison of the plastic strain profiles for the analysis with the nonlocal model of the 1D direct tension test for three different meshes.

6.4.2 Reinforced concrete beam

The first analysed structural member was the reinforced concrete beam no. 5 from the series of experiments, reported in Leonhardt and Walther (1962). The beam was subjected to four-point loading and exhibited shear failure in absence of shear reinforcement (Figure 6.9). Due to symmetry, only half of the specimen was analysed by constraining the horizontal displacements of all nodes lying on the symmetry plane. Direct displacement control was applied for the vertical displacement of the lowest point of the midspan of the beam. Concrete was modelled by 2D plane strain triangular elements because they result in a decreased computational load compared to a 3D analysis and because CDPM2 was formulated in 2D only for plane strain conditions.

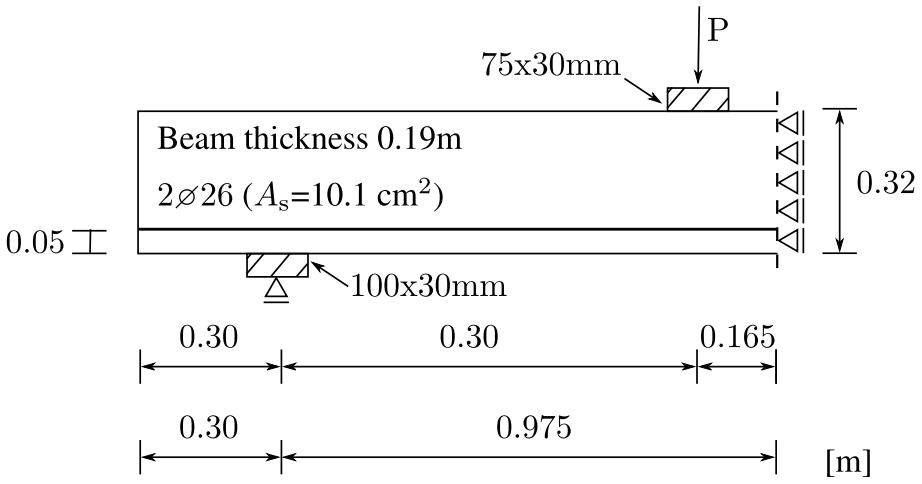

Figure 6.9: Geometry and setup of the reinforced concrete beam (Leonhardt and Walther, 1962).

The elastic solution in the 3D domain is closer to the plane stress solution but during fracture the response of the beam is a combination of the plane stress and the plane strain solutions (Bažant and Kazemi, 1991). Furthermore, the plasticity algorithm was formulated in 2D for plane strain. A coarse, a medium and a fine mesh were analysed with element sizes $h = 0.02$, 0.01 and 0.005 m.

The procedure, described in Section 6.4.1, was applied to calibrate the two material models. The calibrated material parameters are: $E = 30.5$ GPa, $\nu = 0.2$, $f_c = 28.5$ MPa, $f_t = 2.247$ MPa. The tensile softening parameters are $w_{ft} = 0.0594$ mm and $\varepsilon_{ft} = 0.00099$ for the crack-band and the nonlocal approach, which fit the fracture energy $G_f = 133$ N/m for the experimental compressive strength f_c. The remaining model parameters are set to their default values specified in Section 6.4.1. Symmetry was taken into account in the material models by modifying the material properties of the points lying close to the symmetry line. In the crack-band approach the fracture energy was assumed to be half of the calibrated value, as proposed by Jirásek and Bauer (2012), whereas in the nonlocal approach symmetric local state variable fields were assumed on the other side of the symmetry line. Steel plates were modelled to be linear elastic with Young's modulus $E = 200$ GPa and Poisson's ratio $\nu = 0.3$. The same constitutive law was applied to describe the response of the longitudinal reinforcement, which was modelled explicitly by truss elements. Perfect bond was assumed between steel and concrete.

The load-displacement curves for the nonlocal and the crack-band approach are presented in Figures 6.10 and 6.11. The initial stiffness is overestimated by both approaches, which may be attributed to the assumed plain strain conditions. Another reason could be the difference between the actual value of the Young's modulus and the one calculated based on the experimental compressive strength according to the equations provided in CEB-FIB Model Code 2010 (FIB, 2012). The experimental results cannot be compared with the analytical ones in the post-peak regime because load-control was applied in these experiments. The contour plots of the maximum tensile principal strain ε_1 for the medium mesh shown in Figure 6.12 correspond to the marked loading steps in Figures 6.10 and 6.11. Vertical failure zones appear in the region of high moment during early loading stages that correspond to the experimentally observed bending cracks. At about 75% of the peak load, diagonal failure zones develop close to the reinforcement and propagate towards the support and the load application point. For large midspan displacements, a diagonal failure zone is visible which is in accordance with the shear band observed in the original experiments. Hence, the analytical model is capable of capturing the shear failure analysed in the present mesh study.

Both approaches are not influenced by the mesh-size for low load levels (Figures 6.10 and 6.11). However, the use of the crack-band approach results in mesh-dependent peak loads and post-peak responses. This effect is also illustrated in Figures 6.13, where the contours of ε_1 at the loading stage 3, marked in Figure 6.11, are shown. The smaller the mesh-size is, the larger is the number of the final failure zones and the smaller is their width. An almost mesh-independent response is shown in the analyses of the medium and fine meshes with the nonlocal approach (Figure 6.10). In the contour plots of ε_1, failure zones from the analyses with the nonlocal model for the fine and the medium mesh include multiple finite elements over their width (Figure 6.13). In the analysis of the coarse mesh with the nonlocal model, the selected mesh-size in the coarse mesh is very large and there are not enough material points within the nonlocal interaction zone to calculate the nonlocal averages accurately. Therefore, failure localises in a single element and the load-displacement curve differs from the ones for the fine and the medium mesh.

All nonlocal analyses underestimate the peak load, which may be attributed to the selected interaction radius R. The influence of R was evaluated by calibrating the nonlocal model for a smaller $R = 0.005$ m and applying it to analyse the fine mesh. The material properties were the same as for the set of parameters used for $R = 0.01$ m except for $\varepsilon_{\mathrm{ft}} = 0.00179$, which results in fracture energy equal to $G_{\mathrm{F}} = 133$ N/m. The predicted peak load for this parameter set is in better agreement with the experimental one (Figure 6.14). The contour plot of ε_1 is illustrated in Figure 6.15 for loading stage 3 marked in Figure 6.14. More and narrower failure zones are observed in the analyses with $R = 0.005$ compared to the ones with $R = 0.01$ m. The interaction radius R in the nonlocal approach has a similar influence to the value of the mesh size in the crack-band approach. The main difference between the two approaches is that R is independent of the mesh size.

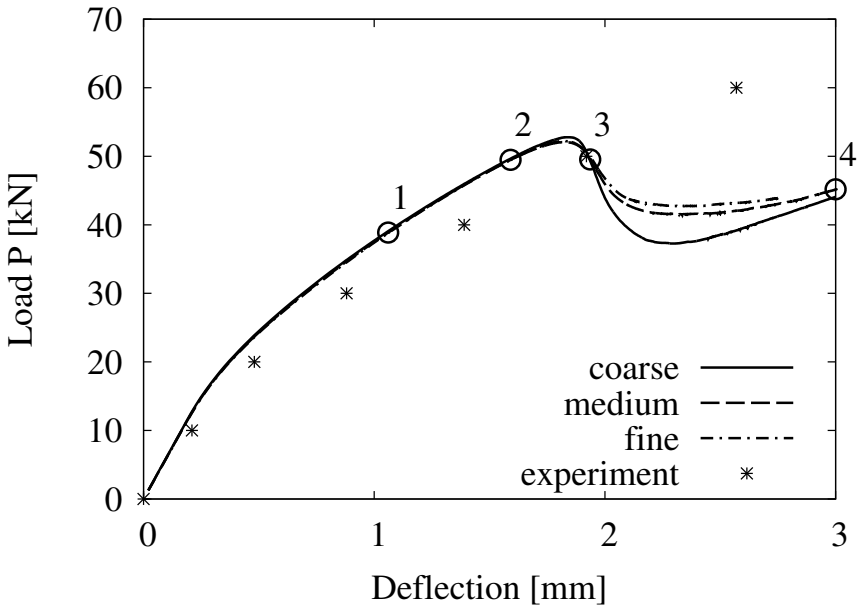

Figure 6.10: Load P-deflection curve for the reinforced concrete beam (Leonhardt and Walther, 1962) analysed for three different meshes with the nonlocal approach. Deflection is measured at the lowest point at the midspan of the beam.

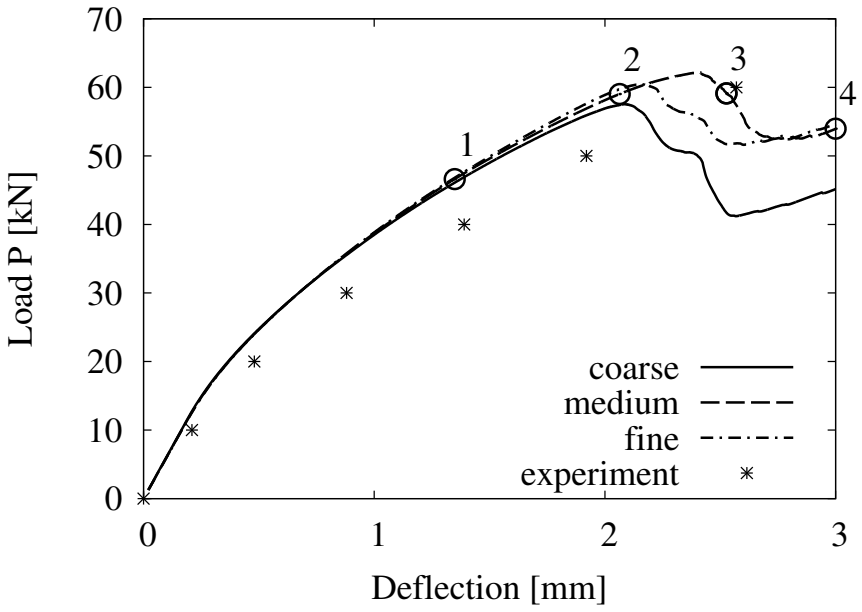

Figure 6.11: Load P-deflection curve for the reinforced concrete beam (Leonhardt and Walther, 1962) analysed for three different meshes with the crack-band approach. Deflection is measured at the lowest point at the midspan of the beam.

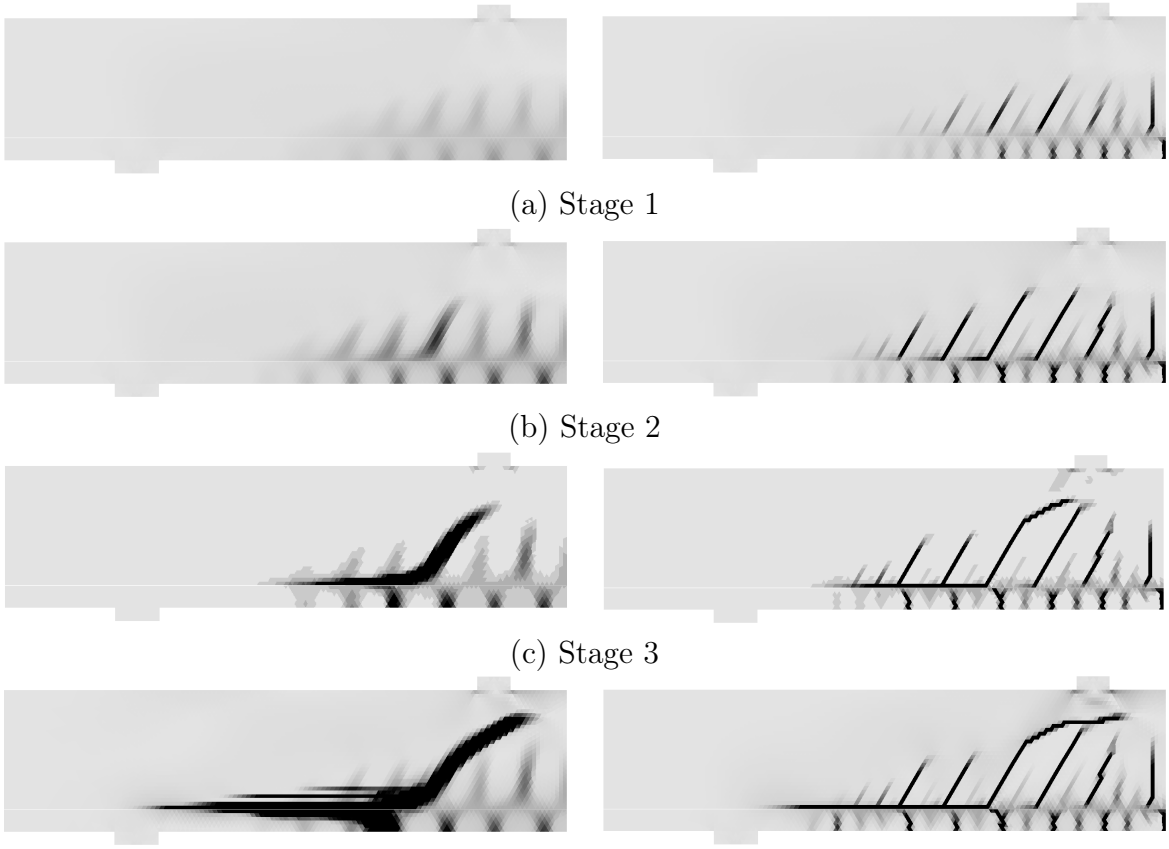

(a) Stage 1

(b) Stage 2

(c) Stage 3

(d)Stage 4

nonlocal approach crack-band approach

Figure 6.12: Evolution of the contour plot of the maximum tensile principal strain ε_1 of the shear beam (Leonhardt and Walther, 1962) for the medium mesh at the three loading stages marked in Figure 6.14 and 6.11. Light gray colour corresponds to values of $\varepsilon_1 < 0$ whereas black colour corresponds to values of $\varepsilon_1 > 10^{-3}$.

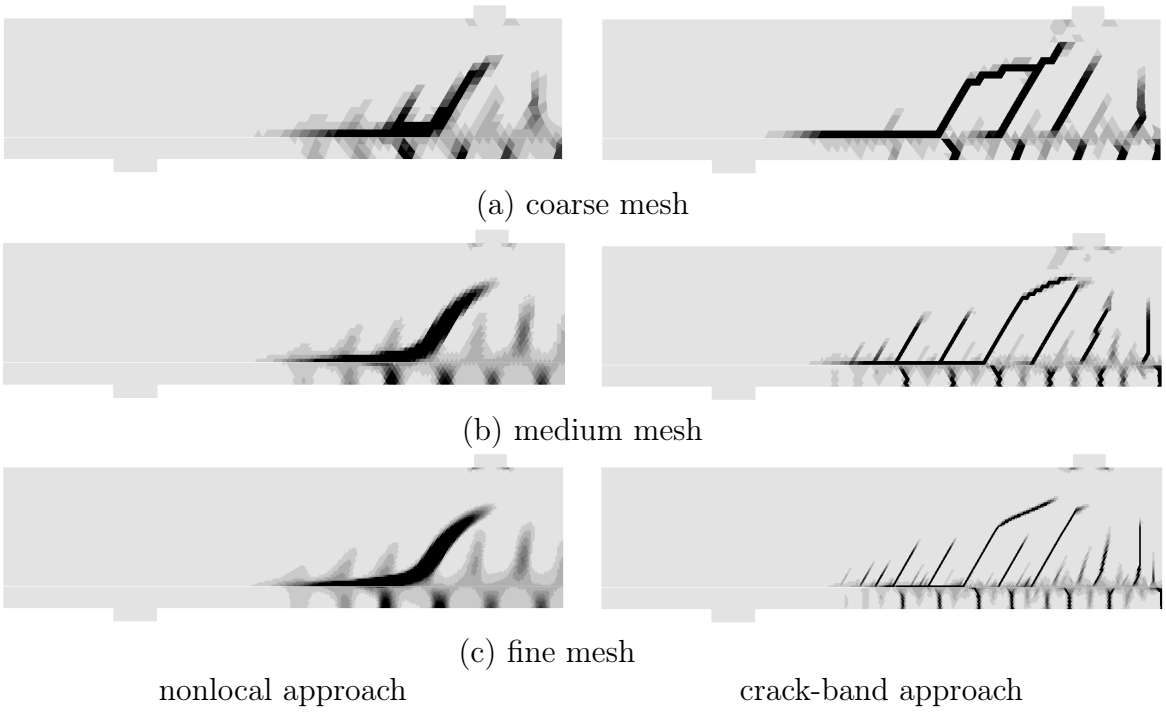

Figure 6.13: Contour plots of the maximum tensile principal strain ε_1 of the shear beam (Leonhardt and Walther, 1962) for all mesh sizes at loading stage 3, marked in Figure 6.14 and 6.11. Light gray colour corresponds to values of $\varepsilon_1 < 0$ whereas black colour corresponds to values of $\varepsilon_1 > 10^{-3}$.

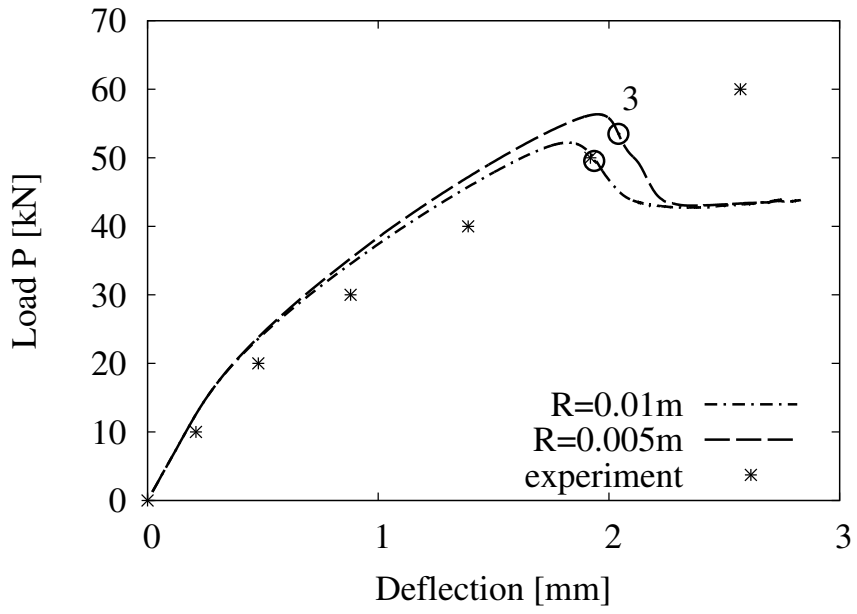

Figure 6.14: Load P-deflection curve of the reinforced concrete beam (Leonhardt and Walther, 1962), analysed for the fine mesh with the two nonlocal models. Deflection is measured at the lowest point of the midspan of the beam.

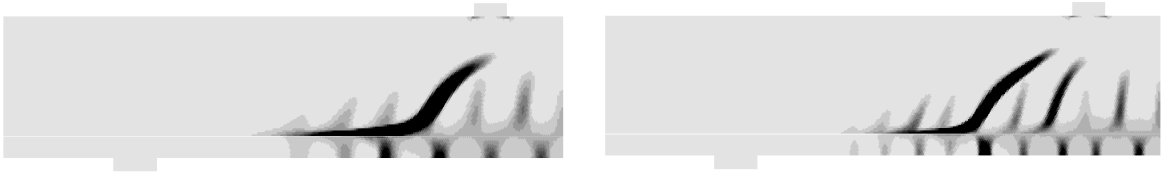

$R = 0.005$ m $R = 0.01$ m

Figure 6.15: Contour plots of the maximum tensile principal strain ε_1 of the shear beam (Leonhardt and Walther, 1962) at loading stage 3, marked in Figure 6.14, for the fine mesh analysed with the nonlocal approach for $R = 0.005$ m and $R = 0.01$ m. Light gray colour corresponds to values of $\varepsilon_1 < 0$ whereas black colour corresponds to values of $\varepsilon_1 > 10^{-3}$.

6.4.3 Reinforced concrete column

A reinforced concrete column subjected to eccentric loading was analysed in the 3D domain. This specimen was selected because it exhibits distributed failure in the form of diffuse cracking and crushing in its tensile and compressive side, respectively (Němeček et al., 2005). Direct displacement control of the midheight lateral deflection was applied. The column is modelled by tetrahedral constant strain elements. A finer mesh with $h = 0.005$ m was not analysed for this model since it resulted in increased computational time. This was because more source points need to be taken into account during nonlocal averaging for the calculation of the nonlocal equivalent strain at the same receiver point. Hence, only a coarse and a medium mesh with $h = 0.02$ m and 0.01 m were analysed.

The column is divided in three zones with different material properties (Figure 6.16). The steel blocks at the top and the bottom zones, were modelled as linear elastic with Young's modulus $E = 210$ GPa and Poisson's ratio $\nu = 0.2$. Concrete zones A, reported to remain undamaged during the experiments, were modelled as linear elastic with $E = 31$ GPa and $\nu = 0.2$. The nonlocal and the crack-band models were applied to analyse the constitutive response concrete zone B and were calibrated following the procedure described in Section 6.4.1 for the material properties calculated based on the compressive strength according to the equations provided in CEB-FIB Model Code 2010 (FIB, 2012). The calibrated material parameters were $E = 31$ GPa, $\nu = 0.2$, $f_c = 30$ MPa, $f_t = 2.355$ MPa. The tensile softening parameters are set to $w_{ft} = 0.0572$ mm and $\varepsilon_{ft} = 0.00099$ for the crack-band and the nonlocal approach to fit the calculated fracture energy $G_F = 163$ N/m. The stirrups were analysed by truss elements as elastic-perfectly plastic with $E = 210$ GPa, $\nu = 0.3$ and yield strength $f_y = 314$ MPa. Co-rotational beam elements were used for the longitudinal reinforcement that was subjected to the large displacements and buckled during the experiment. The constitutive response was modelled as elastic-perfectly plastic with $E = 210$ GPa, $\nu = 0.3$ and $f_y = 561$ MPa. A perfect bond was assumed between the steel reinforcement and concrete.

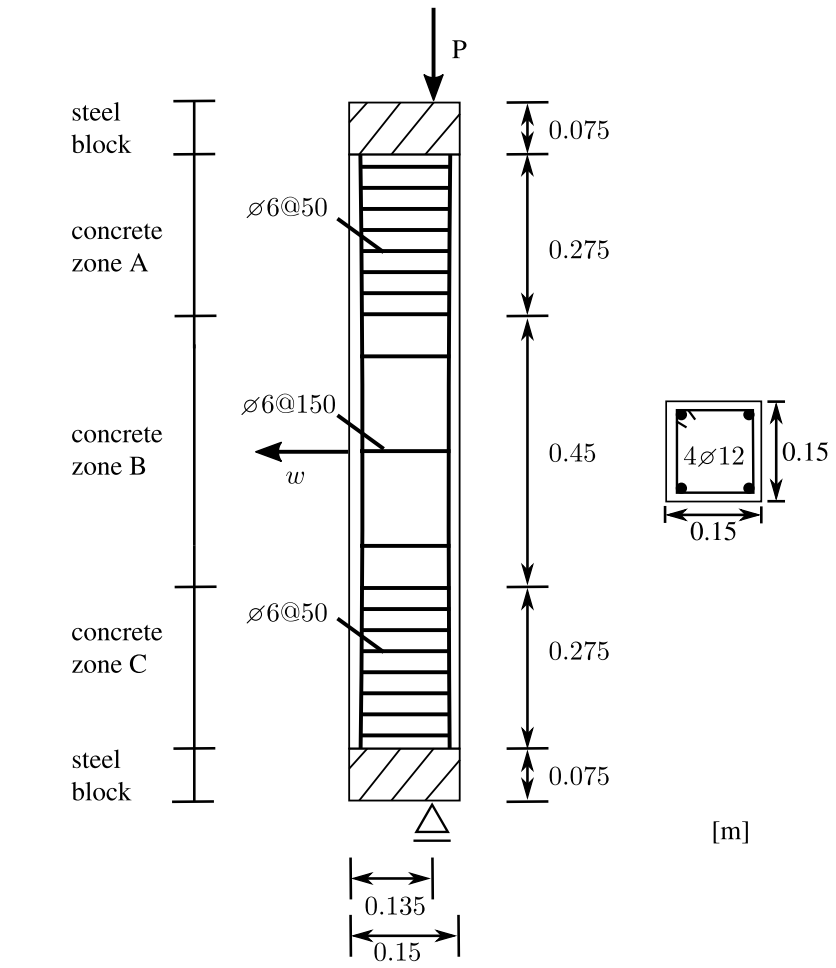

Figure 6.16: Geometry and setup of the reinforced concrete column (Němeček et al., 2005).

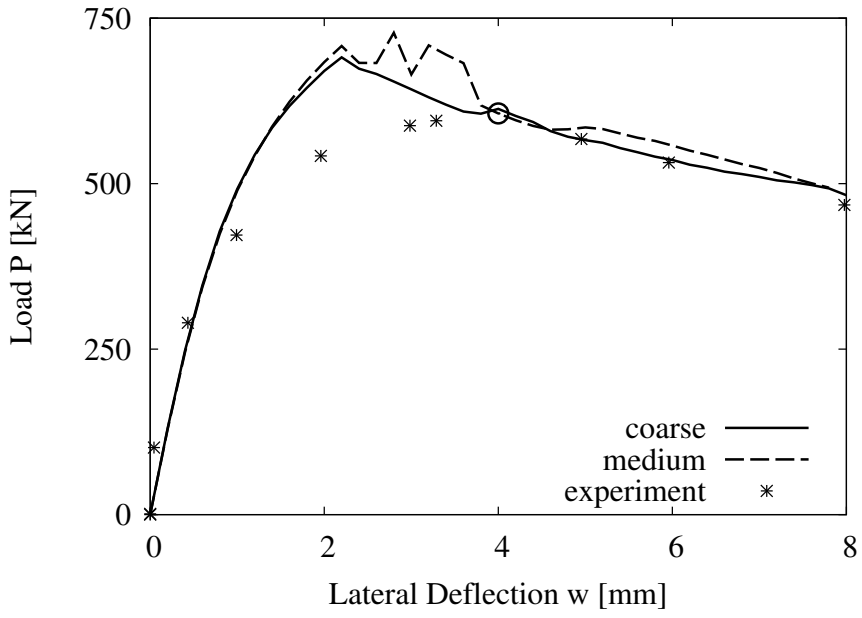

Figure 6.17: Load P-lateral deflection for the eccentric column (Němeček et al., 2005) analysed for two different meshes with the crack-band approach. Lateral deflection w is measured at the midpoint of the tensile side.

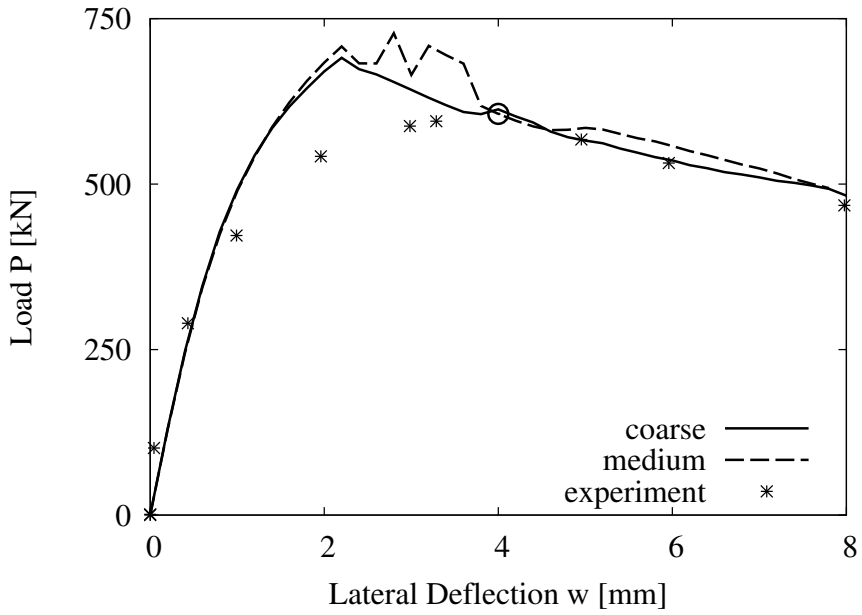

Figure 6.18: Load P-lateral deflection for the eccentric column (Němeček et al., 2005) analysed for two different meshes with the nonlocal approach. Lateral deflection w is measured at the midpoint of the tensile side.

In Figures 6.17 and 6.18, the load-lateral deflection curves are shown for the crack-band and the nonlocal approach. The initial stiffness for all analyses is close to the experimental one but the peak load is overpredicted, which may be attributed to the difference between the actual and the calculated material properties based on the recommendations of CEB-FIB Model Code 2010 (FIB, 2012). Another reason could be the simple calibration procedure that was followed instead of other more advanced techniques proposed, for example in Iacono et al. (2006). Both approaches lead to a mesh-independent description of the pre-peak and the late post-peak response. For the same mesh size, the load-lateral deflection curves for the nonlocal and the crack-band model are very similar to each other (Figures 6.17 and 6.18). The contour plots of ε_1 are shown for all analyses in Figure 6.19 for the marked loading step in Figures 6.17 and 6.18. Highly strained zones exist in both the tensile and the compressive side of the specimen, which is in agreement with the regions of cracking and crushing observed in the experiments. Both approaches resulted in similar ε_1 fields that were mesh-independent. However, in the contour plots of the damage variables a different failure mechanism is observed for each model (Figure 6.20). In the contour plots of ω_t for the crack-band approach, high values are limited on the tensile side of the specimen and around the longitudinal reinforcement. In the nonlocal approach the fields of ω_t are distributed over a larger area including both the compressive and the tensile sides of the specimen. On the contrary, in the contour plot for ω_c for the nonlocal approach large values of damage appear only at the compressive side of the specimen whereas in crack-band approach large values of ω_c are found on both sides of the specimen.

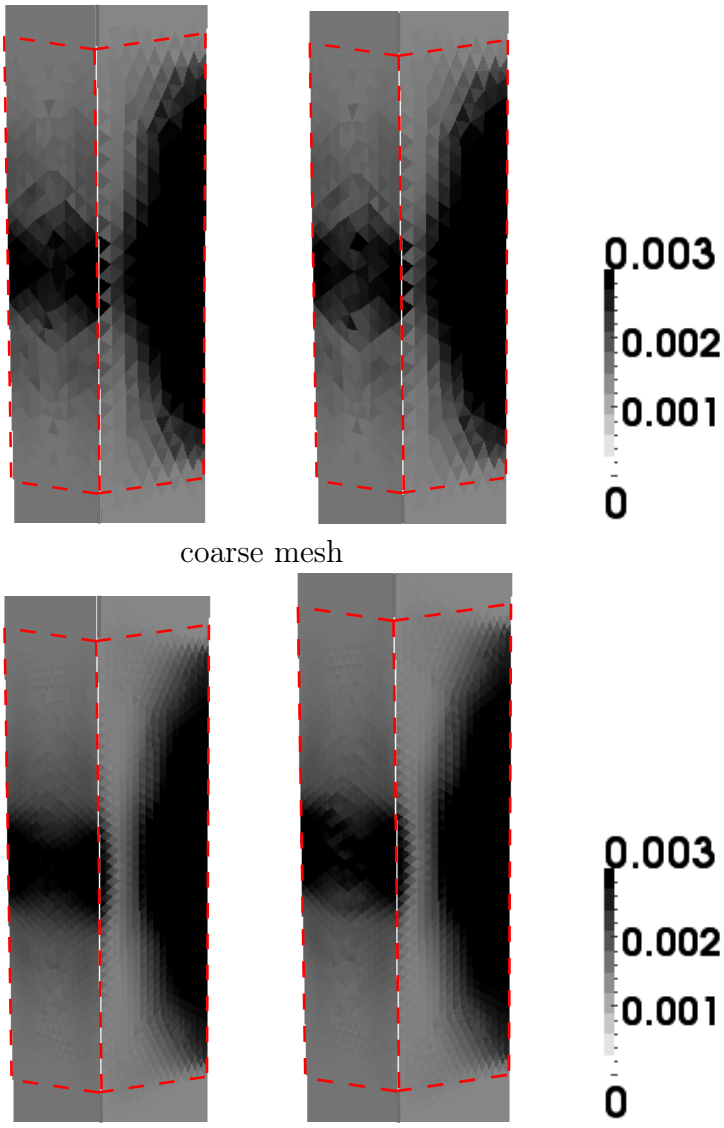

Figure 6.19: Contour plot of the maximum tensile strain ε_1 of the eccentrically loaded column (Němeček et al., 2005) at the loading stage, marked in Figures 6.17 and 6.18, for the two different mesh sizes analysed with the crack-band and the nonlocal model. Light gray colour corresponds to $\varepsilon_1 < 0$ whereas black colour corresponds to $\varepsilon_1 > 3 \cdot 10^{-3}$. The boundaries of concrete zone B are marked by the dashed red lines.

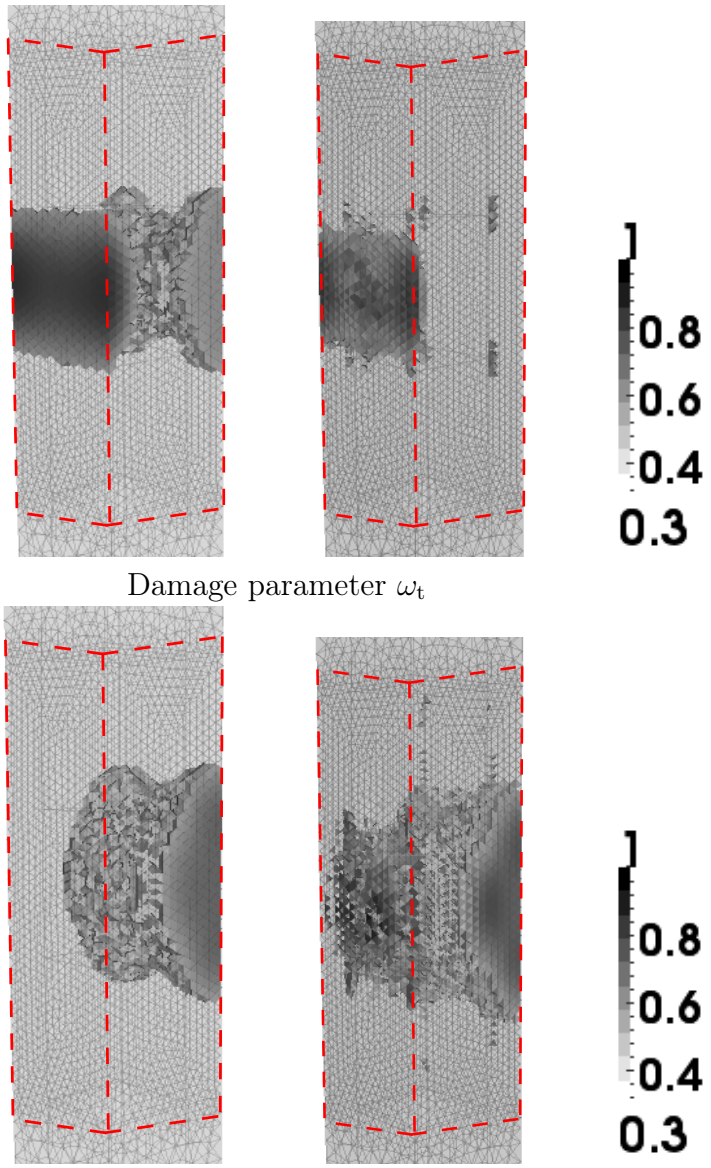

Figure 6.20: Contour plots of the damage variables ω_t and ω_c of the eccentrically loaded column (Němeček et al., 2005) at the loading stage, marked in Figures 6.17 and 6.18, for the two different mesh sizes analysed with the crack-band and the nonlocal approach. Light gray colour corresponds to values of the damage variable smaller than 0.3, whereas black colour corresponds to values equal to 1. The boundaries of concrete zone B are marked by the dashed red lines.

6.5 Discussion

The present study focuses on the mesh-dependence of damage-plasticity material models formulated according to the crack-band and the nonlocal approach. The advanced damage-plasticity constitutive law CDPM2, originally formulated based on the crack-band approach in Grassl et al. (2013), was extended according to the nonlocal approach.

The nonlocal and the crack-band model were applied to model a one-dimensional bar subjected to direct tension, which is similar to the one presented in Section 3.3. Both material models resulted in mesh-independent average stress-strain curves. For $H_{\mathrm{p}} > 0$ the nonlocal models provided mesh-independent plastic strain profiles, which is in agreement with the results reported in Grassl and Jirásek (2004). The width of the zone in which energy is dissipated decreases in the analyses with the crack-band approach for decreasing mesh size and the local dissipated energy density increases.

Furthermore, the two approaches were applied to model a reinforced concrete beam in 2D that was experimentally investigated in Leonhardt and Walther (1962). The analysed model is considered capable of describing shear failure, because the evolution of the failure patterns was in accordance with the observations reported for this failure mode in similar experimental campaigns (Bažant and Kazemi, 1991; Vecchio and Shim, 2004). In the crack band approach, both the crack patterns and the load-displacement curves depended on the selected element size. Nonlocal models lead to mesh-independent results as long as the mesh size was small enough to ensure that there were enough material points contributing to the calculated nonlocal equivalent strain. The main advantage of nonlocal models is that the selection of the value of R has a similar influence on the final failure patterns with the mesh size but its value is not related to the analysed mesh.

The two material models were also used in the analysis of a reinforced concrete column subjected to eccentric compression (Němeček et al., 2005). Both approaches resulted in mesh-independent descriptions of failure and provided similar load-lateral deflection curves. However, different failure mechanisms are observed in the form of contour plots of the damage variables fields.

Chapter 7

Conclusions and future work

7.1 Conclusions

The main subject of the present thesis was the development and application of integral-type nonlocal models. The author evaluated different methodologies to take into account the influence of boundaries in nonlocal averaging procedures. A calibration methodology for the interaction radius of nonlocal models based on the final fracture surface was proposed. Furthermore, a damage-plasticity constitutive law was formulated according to the nonlocal theory and was applied to analyse reinforced concrete members. The main conclusions of the research reported in this thesis are summarised in what follows.

The application of the standard scaling approach leads to spurious energy dissipation close to boundaries and to an overestimation of the peak load in notched specimens subjected to three-point bending, which is not in agreement with meso-scale analyses results. The main reason for this overestimation are the nonlocal contributions from undamaged source points that are away from the notch and are characterised by lower equivalent strains. The local complement, the stress-based and the distance-based approaches lead to a reduction of the local dissipation near the boundaries. For the unnotched specimens, the dissipated energy is reasonably distributed for all approaches, but is underpredicted in the analyses with the local complement method. Two additional input parameters are introduced in the distance-based approach, compared to standard scaling, whereas the stress-based approach requires only one additional parameter. The local complement formulation does not include any additional parameters. The nonlocal damage-plasticity approach also does not require any additional parameters, but leads to an overestimation of the dissipated energy close to the notch,

in the over-nonlocal formulation. In the case of standard averaging with $m = 1$, the damage-plasticity model provides results, that are in better agreement with the meso-scale analyses. However, the width of the fracture process zone depends on the selected finite element size.

A methodology to calibrate the interaction radius in nonlocal models based on experimental crack patterns was proposed. Meso-scale investigations were performed to validate the assumptions of this calibration procedure. According to the results of the meso-scale analyses, the majority of the fracture energy is dissipated in a rough crack. The width of the fracture process zone, determined from the energy dissipated in the localised crack, increases for increasing size of the heterogeneities modelled, which is controlled by the autocorrelation length of the random field.

A mesh study was conducted by analysing two reinforced concrete members with the nonlocal and the crack-band formulation of the damage-plasticity constitutive law CDPM2. The analyses with the nonlocal model are insensitive to the element size as long as the it is small enough to ensure that there are always enough material points contributing to the calculated nonlocal equivalent strain. The crack-band models lead to mesh dependent crack patterns and load-displacement curves in the first specimen, which was a beam failing in shear. Furthermore, the distributed compressive failure observed in the concrete column is analysed mesh-independently for both constitutive laws. However, the compressive and tensile damage fields are different in the two approaches.

7.2 Future work

Further research is required in order to extend the findings of the present thesis to different applications. Proposals for the investigation of different aspects of the topics addressed in the present thesis are discussed as follows.

Quasi-static loading conditions have been assumed throughout this thesis and dynamic phenomena were not included. Experimental investigations and meso-scale studies on the size of the FPZ for different strain rates is a potential direction of future research. The results could be applied to extend the described boundary approaches and calibration strategies to dynamic fracture.

There is no consensus on how to define the nonlocal domain during compressive failure. In the present thesis, the author investigated the modelling of boundaries and the calibration procedure of nonlocal models by analysing specimens where tensile failure dominates. The proposed techniques need to be extended to compressive failure. Moreover, nonlocal averaging close to the interface of two materials such as steel and concrete should be further investigated.

Size-effect is another important aspect. The performance of the boundary approaches was evaluated based on the analyses results of beams with the same ligament length subjected to three point bending. These methodologies should be applied in analysing geometrically similar specimens for the same set of parameters in order to evaluate their ability to describe the observed size effect in both material strength and fracture energy.

Finally, decreasing the computational cost needed for the solution of problems with many degrees of freedom would be another direction for further research. A more efficient and optimised data structure to store the weights used in nonlocal averaging is important to reduce the memory requirements of these problems. The calculation of the nonlocal averages can also be accelerated by parallel processing techniques that would dramatically reduce the computation time of those analyses.

Bibliography

Aifantis, E.C., 1984. On the microstructural origin of certain inelastic models. Journal of Engineering Materials and Technology 106, 326–330.

Bahn, B.Y., Hsu, C.T.T., 1988. Stress-strain behavior of concrete under cyclic loading. ACI-Materials Journal 95, 178–193.

Bažant, Z.P., 1994. Nonlocal damage theory based on micromechanics of crack interactions. Journal of Engineering Mechanics 120, 593–617.

Bažant, Z.P., Jirásek, M., 2002. Nonlocal integral formulations of plasticity and damage: survey of progress. Journal of Engineering Mechanics 128, 1119–1149.

Bažant, Z.P., Kazemi, M.T., 1991. Size effect on diagonal shear failure of beams without stirrups. ACI-Structural Journal 88, 268–276.

Bažant, Z.P., Le, J.L., Hoover, C., 2010. Nonlocal Boundary Layer (NBL) model: overcoming boundary condition problems in strength statistics and fracture analysis of quasibrittle materials, in: Oh, B.H. (Ed.), Fracture Mechanics of Concrete and Concrete Structures, Jeju, Korea, pp. 135–143.

Bažant, Z.P., Oh, B.H., 1983. Crack band theory for fracture of concrete. Matériaux et Construction 16, 155–177.

Bažant, Z.P., Pijaudier-Cabot, G., 1989. Measurement of characteristic length of nonlocal continuum. Journal of Engineering Mechanics 115, 755–767.

Bažant, Z.P., Xiang, Y., 1997. Size effect in compression fracture: splitting crack band propagation. Journal of Engineering Mechanics 123, 162–172.

Bažant, Z.P., 1999. Size effect on structural strength: a review. Archive of Applied Mechanics 69, 703–725.

Bazant, Z.P., Pijaudier-Cabot, G., 1988. Nonlocal continuum damage, localization instability and convergence. Journal of Applied Mechanics 55, 287–293.

Bellégo, C.L., Dubé, J.F., Pijaudier-Cabot, G., Gérard, B., 2003. Calibration of nonlocal damage model from size effect tests. European Journal of Mechanics - A/Solids 22, 33–46.

Bićanić, N., Pearce, C.J., 1996. Computational aspects of a softening plasticity model for plain concrete. Mechanics of Cohesive-frictional Materials 1, 75–94.

Bolander, J.E., Hikosaka, H., 1995. Simulation of fracture in cement-based composites. Cement and Concrete Composites 17, 135–145.

Bolander, J.E., Saito, S., 1998. Fracture analyses using spring networks with random geometry. Engineering Fracture Mechanics 61, 569–591.

Bolander, J.E., Sukumar, N., 2005. Irregular lattice model for quasistatic crack propagation. Physical Review B 71, 094106.

Borino, G., Failla, B., Parrinello, F., 2002. A symmetric formulation for nonlocal damage models, in: Mang, H.A. and Rammerstoffer, F.G and Eberhardsteiner, J. (Ed.), Proceedings of the 5th World Congress on Computational Mechanics (WCCM V), Vienna, Austria, 2002.

Borino, G., Failla, B., Parrinello, F., 2003. A symmetric nonlocal damage theory. International Journal of Solids and Structures 40, 3621–3645.

de Borst, R., 1987. Smeared cracking, plasticity, creep, and thermal loading–a unified approach. Computer Methods in Applied Mechanics and Engineering 62, 89–110.

Bouchaud, E., Lapasset, G., Planés, J., 1990. Fractal Dimension of Fractured Surfaces: A Universal Value? Europhysics Letters 13, 73–79.

Carmeliet, J., 1999. Optimal estimation of gradient damage parameters from localization phenomena in quasi-brittle materials. Mechanics of Cohesive-frictional Materials 4, 1–16.

Carol, I., Rizzi, E., Willam, K., 1994. A unified theory of elastic degradation and damage based on a loading surface. International Journal of Solids and Structures 31, 2835–2865.

Carpinteri, A., Cornetti, P., Puzzi, S., 2004. A stereological analysis of aggregate grading and size effect on concrete tensile strength. International Journal of Fracture 128, 233–242.

Cedolin, L., Poli, S.D., Iori, I., 1983. Experimental determination of the fracture process zone in concrete. Cement and Concrete Research 13, 557–567.

Cedolin, L., Poli, S.D., Iori, I., 1987. Tensile behavior of concrete. Journal of Engineering Mechanics - ASCE 113, 431–449.

Chaboche, J.L., 1993. Development of continuum damage mechanics for elastic solids sustaining anisotropic and unilateral damage. International Journal of Damage Mechanics 2, 311–329.

Chen, B., Liu, J., 2004. Experimental study on AE characteristics of three-point-bending concrete beams. Cement and Concrete Research 34, 391–397.

Cundall, P.A., Strack, O.D.L., 1979. A discrete numerical model for granular assemblies. Géotechnique 29, 47–65.

Di Luzio, G., Bažant, Z.P., 2005. Spectral analysis of localization in nonlocal and over-nonlocal materials with softening plasticity or damage. International Journal of Solids and Structures 42, 6071–6100.

Eringen, A.C., Edelen, D.G.B., 1972. On nonlocal elasticity. International Journal of Engineering Science 10, 233–248.

Etse, G., Willam, K., 1994. Fracture energy formulation for inelastic behavior of plain concrete. Journal of Engineering Mechanics 120, 1983–2011.

Etse, G., Willam, K., 1996. Integration algorithms for concrete plasticity. Engineering Computations 13, 38–65.

FIB, 2012. FIB-Model Code for Concrete Structures 2010. International Federation for Structural Concrete (FIB).

Fichant, S., La Borderie, C., Pijaudier-Cabot, G., 1999. Isotropic and anisotropic descriptions of damage in concrete structures. Mechanics of Cohesive-Frictional Materials 4, 339–359.

Fleck, N.A., Muller, G.M., Ashby, M.F., Hutchinson, J.W., 1994. Strain gradient plasticity: theory and experiment. Acta Metallurgica et Materialia 42, 475–487.

Folino, P., Etse, G., 2012. Performance Dependent Model for normal and high strength concretes. International Journal of Solids and Structures 49, 701–719.

Frantziskonis, G., 1995. Heterogeneity and implicated surface effects: statistical, fractal formulation and relevant analytical solution. Acta Mechanica 108, 157–178.

Ganghoffer, J.F., de Borst, R., 2000. A new framework in nonlocal mechanics. International Journal of Engineering Science 38, 453–486.

Giry, C., Dufour, F., Mazars, J., 2011. Stress-based nonlocal damage model. International Journal of Solids and Structures 48, 3431–3443.

Gitman, I.M., Askes, H., Aifantis, E.C., 2005. The representative volume size in static and dynamic micro-macro transitions. International Journal of Fracture 135, L3–L9.

Gitman, I.M., Askes, H., Sluys, L.J., 2008. Coupled-volume multi-scale modelling of quasi-brittle material. European Journal of Mechanics - A/Solids 27, 302–327.

Gitman, I.M., Gitman, M.B., Askes, H., 2006. Quantification of stochastically stable representative volumes for random heterogeneous materials. Archive of Applied Mechanics 75, 79–92.

Granger, S., Loukili, A., Pijaudier-Cabot, G., Chanvillard, G., 2007. Experimental characterization of the self-healing of cracks in an ultra high performance cementitious material: mechanical tests and acoustic emission analysis. Cement and Concrete Research 37, 519–527.

Grassl, P., 2004. Modelling of dilation of concrete and its effect in triaxial compression. Finite Elements in Analysis and Design 40, 1021–1033.

Grassl, P., Bažant, Z.P., 2009. Random lattice-particle simulation of statistical size effect in quasi-brittle structures failing at crack initiation. Journal of Engineering Mechanics - ASCE 135, 85–92.

Grassl, P., Grégoire, D., Rojas-Solano, L.B., Pijaudier-Cabot, G., 2012. Meso-scale modelling of the size effect on the fracture process zone of concrete. International Journal of Solids and Structures 49, 1818–1827.

Grassl, P., Jirásek, M., 2004. Nonlocal plastic models for cohesive-frictional materials. CRC Press. pp. 323–337.

Grassl, P., Jirásek, M., 2006a. Plastic model with non-local damage applied to concrete. International Journal for Numerical and Analytical Methods in Geomechanics 30, 71–90.

Grassl, P., Jirásek, M., 2006b. Damage-plastic model for concrete failure. International Journal of Solids and Structures 43, 7166–7196.

Grassl, P., Jirásek, M., 2008. Meso-mechanically motivated nonlocal models for the modelling of the fracture process zone in quasi-brittle materials, in: Schreffler, B.A., Perego, U. (Eds.), WCCM8, 8th World Congress on Computational Mechanics, Venice, Italy.

Grassl, P., Jirásek, M., 2010. Meso-scale approach to modelling the fracture process zone of concrete subjected to uniaxial tension. International Journal of Solids and Structures 47, 957–968.

Grassl, P., Lundgren, K., Gylltoft, K., 2002. Concrete in compression: a plasticity theory with a novel hardening law. International Journal of Solids and Structures 39, 5205–5223.

Grassl, P., Xenos, D., Jirásek, M., Horák, M., 2014. Evaluation of nonlocal approaches for modelling fracture near nonconvex boundaries. International Journal of Solids and Structures 51, 3239–3251.

Grassl, P., Xenos, D., Nyström, U., Rempling, R., Gylltoft, K., 2013. CDPM2: a damage-plasticity approach to modelling the failure of concrete. International Journal of Solids and Structures 50, 3805–3816.

Grégoire, D., Verdon, L., Lefort, V., Grassl, P., Saliba, J., Regoin, J.P., Loukili, A., Pijaudier-Cabot, G., 2015. Mesoscale analysis of failure in quasi-brittle materials:

comparison between lattice model and acoustic emission data. International Journal for Numerical and Analytical Methods in Geomechanics .

Griffiths, D.V., Mustoe, G.G.W., 2001. Modelling of elastic continua using a grillage of structural elements based on discrete element concepts. International Journal for Numerical Methods in Engineering 50, 1759–1775.

Guinea, G.V., Planas, J., Elices, M., 1992. Measurement of the fracture energy using three-point bend tests: part 1 - influence of experimental procedures. Materials and Structures 25, 212–218.

Haidar, K., Pijaudier-Cabot, G., Dubé, J.F., Loukili, A., 2005. Correlation between the internal length, the fracture process zone and size effect in model materials. Materials and Structures 38, 201–210.

Herrmann, H.J., Hansen, A., Roux, S., 1989. Fracture of disordered, elastic lattices in 2 dimensions. Physical Review B 39, 637–648.

Hillerborg, A., Modéer, M., Petersson, P.E., 1976. Analysis of crack formation and crack growth in concrete by means of fracture mechanics and finite elements. Cement and Concrete Research 6, 773–781.

Hofstetter, B., Valentini, G., 2013. Review and enhancement of 3D concrete models for large-scale numerical simulations of concrete structures. International Journal for Numerical and Analytical Methods in Geomechanics 37, 221–246.

Hu, X., Wittmann, F.H., 1990. Experimental method to determine extension of fracture-process zone. Journal of Materials in Civil Engineering 2, 15–23.

Hu, X., Wittmann, F.H., 1992. Fracture energy and fracture process zone. Materials and Structures 25, 319–326.

Huerta, A., Rodríguez Ferran, A., Díez, P., et al., 2002. Error estimation and adaptivity for nonlinear FE analysis. International Journal of Applied Mathematics and Computer Sciences 12, 59–70.

Iacono, C., Sluys, L.J., van Mier, J.G.M., 2006. Estimation of model parameters in nonlocal damage theories by inverse analysis techniques. Computer Methods in Applied Mechanics and Engineering 195, 7211–7222.

Iacono, C., Sluys, L.J., van Mier, J.G.M., 2008. Calibration of a higher-order continuum model using global and local data. Engineering Fracture Mechanics 75, 4642–4665.

Imran, I., Pantazopoulou, S.J., 1996. Experimental study of plain concrete under triaxial stress. ACI-Materials Journal 93.

Jankowski, L.J., Styś, D.J., 1990. Formation of the fracture process zone in concrete. Engineering Fracture Mechanics 36, 245–253.

Jason, L., Huerta, A., Pijaudier-Cabot, G., Ghavamian, S., 2006. An elastic plastic damage formulation for concrete: application to elementary tests and comparison with an isotropic damage model. Computer Methods in Applied Mechanics and Engineering 195, 7077–7092.

Jirásek, M., Bauer, M., 2012. Numerical aspects of the crack band approach. Computers & Structures 110–111, 60–78.

Jirásek, M., Bažant, Z.P., 1994. Localization analysis of nonlocal model based on crack interactions. Journal of Engineering Mechanics 120, 1521–1542.

Jirásek, M., Bažant, Z.P., 1995. Particle model for quasibrittle fracture and application to sea-ice. Journal of Engineering Mechanics - ASCE 121, 1016–1025.

Jirásek, M., Bažant, Z.P., 2002. Inelastic analysis of structures. John Wiley & Sons.

Jirásek, M., Grassl, P., 2008. Evaluation of directional mesh bias in concrete fracture simulations using continuum damage models. Engineering Fracture Mechanics 75, 1921–1943.

Jirásek, M., Rolshoven, S., 2003. Comparison of integral-type nonlocal plasticity models for strain-softening materials. International Journal of Engineering Science 41, 1553–1602.

Jirásek, M., Rolshoven, S., Grassl, P., 2004. Size effect on fracture energy induced by non-locality. International Journal for Numerical and Analytical Methods in Geomechanics 28, 653–670.

Kawai, T., 1978. New discrete models and their application to seismic response analysis of structures. Nuclear Engineering and Design 48, 207–229.

Kawai, T., 1980. Some consideration on the finite element method. International Journal for Numerical Methods in Engineering 16, 81–120.

Krayani, A., Pijaudier-Cabot, G., Dufour, F., 2009. Boundary effect on weight function in nonlocal damage model. Engineering Fracture Mechanics 76, 2217–2231.

Kreijger, P.C., 1984. The skin of concrete composition and properties. Matériaux et Construction 17, 275–283.

Kröner, E., 1967. Elasticity theory of materials with long range cohesive forces. International Journal of Solids and Structures 3, 731–742.

Labuz, J.F., Biolzi, L., 1998. Characteristic strength of quasi-brittle materials. International Journal of Solids and Structures 35, 4191–4203.

Landis, E.N., 1999. Micro–macro fracture relationships and acoustic emissions in concrete. Construction and Building Materials 13, 65–72.

Lange, D.A., Jennings, H.M., Shah, S.P., 1993. Relationship between fracture surface roughness and fracture behavior of cement paste and mortar. Journal of the American Ceramic Society 76, 589–597.

Leonhardt, F., Walther, R., 1962. Schubversuche an einfeldrigen Stahlbetonbalken mit und ohne Schubbewehrung zur Ermittlung der Schubtragfähigkeit und der oberen Schubspannungsgrenze. DAfStb-Deutscher Ausschuss für Stahlbeton .

Li, V.C., Maalej, M., 1996. Toughening in cement based composites. Part I: cement, mortar, and concrete. Cement and Concrete Composites 18, 223–237.

Liebe, T., Willam, K., 2001. Localization properties of generalized Drucker-Prager elastoplasticity. Journal of Engineering Mechanics 127, 616–619.

Lilliu, G., van Mier, J.G.M., 2003. 3D lattice type fracture model for concrete. Engineering Fracture Mechanics 70, 927–941.

Luccioni, B., Oller, S., 2003. A directional damage model. Computer Methods in Applied Mechanics and Engineering 192, 1119–1145.

Mahnken, R., Kuhl, E., 1999. Parameter identification of gradient enhanced damage models with the finite element method. European Journal of Mechanics - A/Solids 18, 819–835.

Mazars, J., Pijaudier-Cabot, G., 1989. Continuum damage theory - application to concrete. Journal of Engineering Mechanics 115, 345–365.

Meschke, G., Lackner, R., Mang, H.A., 1998. An anisotropic elastoplastic-damage model for plain concrete. International Journal for Numerical Methods in Engineering 42, 703–727.

van Mier, J.G.M., 1986. Multiaxial strain-softening of concrete. Materials and Structures 19, 179–200.

van Mier, J.G.M., 1991. Mode I fracture of concrete: discontinuous crack growth and crack interface grain bridging. Cement and Concrete Research 21, 1–15.

Mihashi, H., Nomura, N., Niiseki, S., 1991. Influence of aggregate size on fracture process zone of concrete detected with three dimensional acoustic emission technique. Cement and Concrete Research 21, 737–744.

Morel, S., Bonamy, D., Ponson, L., Bouchaud, E., 2008. Transient damage spreading and anomalous scaling in mortar crack surfaces. Physical Review E 78, 016112.

Murakami, S., Ohno, N., 1981. A continuum theory of creep and creep damage, in: Ponter, A.R.S., Hayhurst, D.R. (Eds.), Creep in Structures. Springer Berlin Heidelberg. International Union of Theoretical and Applied Mechanics, pp. 422–444.

Muralidhara, S., Prasad, B.K.R., Eskandari, H., Karihaloo, B.L., 2010. Fracture process zone size and true fracture energy of concrete using acoustic emission. Construction and Building Materials 24, 479–486.

Mühlhaus, H.B., Alfantis, E.C., 1991. A variational principle for gradient plasticity. International Journal of Solids and Structures 28, 845–857.

Nakamura, H., Higai, T., 2001. Compressive fracture energy and fracture zone length of concrete, in: Modeling of inelastic behavior of RC structures under seismic loads. American Society of Civil Engineers - ASCE, pp. 471–487.

Nirmalendran, S., Horii, H., 1992. Analytical modeling of microcracking and bridging in the fracture of quasi-brittle materials. Journal of the Mechanics and Physics of Solids 40, 863–886.

Němeček, J., Padevět, P., Patzák, B., Bittnar, Z., 2005. Effect of transversal reinforcement in normal and high strength concrete columns. Materials and Structures 38, 665–671.

Ortiz, M., 1985. A constitutive theory for the inelastic behavior of concrete. Mechanics of Materials 4, 67–93.

Otsuka, K., Date, H., 2000. Fracture process zone in concrete tension specimen. Engineering Fracture Mechanics 65, 111–131.

Pamin, J., de Borst, R., 1998. Simulation of crack spacing using a reinforced concrete model with an internal length parameter. Archive of Applied Mechanics 68, 613–625.

Papanikolaou, V.K., Kappos, A.J., 2007. Confinement-sensitive plasticity constitutive model for concrete in triaxial compression. International Journal of Solids and Structures 44, 7021–7048.

Peerlings, R.H.J., de Borst, R., Brekelmans, W.A.M., de Vree, J.H.P., Spee, I., 1996. Some observations on localisation in non-local and gradient damage models. European Journal of Mechanics - A/Solids 15, 937–953.

Pijaudier-Cabot, G., Bažant, Z.P., 1987. Nonlocal damage theory. Journal of Engineering Mechanics 113, 1512–1533.

Pijaudier-Cabot, G., Benallal, A., 1993. Strain localization and bifurcation in a nonlocal continuum. International Journal of Solids and Structures 30, 1761–1775.

Pijaudier-Cabot, G., Dufour, F., 2010. Nonlocal damage model: boundary and evolving boundary effects. European Journal of Environmental and Civil Engineering 14, 729–749.

Planas, J., Elices, M., Guinea, G.V., 1993. Cohesive cracks versus nonlocal models: closing the gap. International Journal of Fracture 63, 173–187.

Polizzotto, C., Fuschi, P., Pisano, A.A., 2006. A nonhomogeneous nonlocal elasticity model. European Journal of Mechanics - A/Solids 25, 308–333.

Prado, E.P., van Mier, J.G.M., 2003. Effect of particle structure on mode I fracture process in concrete. Engineering Fracture Mechanics 70, 1793–1807.

Přikryl, R., Lokajíček, T., Li, C., Rudajev, V., 2003. Acoustic emission characteristics and failure of uniaxially stressed granitic rocks: the effect of rock fabric. Rock Mechanics and Rock Engineering 36, 255–270.

Rizzi, E., Carol, I., Willam, K., 1995. Localization analysis of elastic degradation with application to scalar damage. Journal of Engineering Mechanics 121, 541–554.

Rojas-Solano, L.B., Grégoire, D., Pijaudier-Cabot, G., 2013. Interaction-based non-local damage model for failure in quasi-brittle materials. Mechanics Research Communications 54, 56–62.

Saouma, V.E., Barton, C.C., Gamaleldin, N.A., 1990. Fractal characterization of fracture surfaces in concrete. Engineering Fracture Mechanics 35, 47–53.

Schlangen, E., van Mier, J.G.M., 1992. Simple lattice model for numerical simulation of fracture of concrete materials and structures. Materials and Structures 25, 534–542.

Shinozuka, M., Deodatis, G., 1996. Simulation of multi-dimensional Gaussian stochastic fields by spectral representation. Applied Mechanics Reviews 49, 29–53.

Shinozuka, M., Jan, C.M., 1972. Digital simulation of random processes and its applications. Journal of Sound and Vibration 25, 111–128.

Simo, J.C., Hughes, T.J.R., 2000. Computational inelasticity. Interdisciplinary Applied Mathematics, Springer New York.

Simo, J.C., Ju, J.W., 1987. Strain- and stress-based continuum damage models - I. Formulation. International Journal of Solids and Structures 23, 821–840.

Tang, T., Bažant, Z.P., Yang, S., Zollinger, D., 1996. Variable-notch one-size test method for fracture energy and process zone length. Engineering Fracture Mechanics 55, 383–404.

Tao, X., Phillips, D.V., 2005. A simplified isotropic damage model for concrete under bi-axial stress states. Cement and Concrete Composites 27, 716–726.

Unger, J.F., Eckardt, S., 2011. Multiscale modeling of concrete. Archives of Computational Methods in Engineering 18, 341–393.

Červenka, J., Papanikolaou, V., 2008. Three dimensional combined fracture–plastic material model for concrete. International Journal of Plasticity 24, 2192–2220.

Červenka, J., Červenka, V., Laserna, S., 2014. On finite element modeling of compressive failure in brittle materials, in: Bicanic, N. and Mang, H. and Meschke, G. and de Borst, R. (Ed.), Computational Modelling of Concrete Structures, pp. 273–281. Euro-C Conference, St. Anton am Alberg, Austria, 2014.

Vecchio, F., Shim, W., 2004. Experimental and analytical reexamination of classic concrete beam tests. Journal of Structural Engineering 130, 460–469.

Vermeer, P.A., Brinkgreve, R.B.J., 1994. A new effective non-local strain-measure for softening plasticity, in: Chambon, R. and Desrues, J. and Vardoulakis, I. (Ed.), Localisation and bifurcation theory for soils and rocks, pp. 89–100. 3rd International Workshop on Localisation and Bifurcation Theory for Soils and Rocks, Grenoble, France, 1993.

Voyiadjis, G.Z., Kattan, P.I., 2009. A comparative study of damage variables in continuum damage mechanics. International Journal of Damage Mechanics 18, 315–340.

Willam, K., Warnke, E.P., 1974. Constitutive model for the triaxial behavior of concrete. IABSE Report, vol. 19. International Association of Bridge and Structural Engineers, Zurich, pp 1–30.

Wu, Z., Rong, H., Zheng, J., Xu, F., Dong, W., 2011. An experimental investigation on the FPZ properties in concrete using digital image correlation technique. Engineering Fracture Mechanics 78, 2978–2990.

Yazdani, S., Schreyer, H.L., 1988. An anisotropic damage model with dilatation for concrete. Mechanics of Materials 7, 231–244.

Zubelewicz, A., Bažant, Z.P., 1987. Interface element modeling of fracture in aggregate composites. Journal of Engineering Mechanics 113, 1619–1630.